EXPERIMENTAL INVESTIGATION OF COAL COMBUSTION IN COAL-LADEN METHANE JETS

BY

RAJAVASANTH RAJASEGAR

THESIS

Submitted in partial fulfillment of the requirements
for the degree of Master of Science in Mechanical Engineering
in the Graduate College of the
University of Illinois at Urbana-Champaign, 2013

Urbana, Illinois

Adviser:

Associate Professor Dimitrios C. Kyritsis

ABSTRACT

Combustion characteristics of methane jets laden with pulverized coal were studied by using a vertically oriented solid particle injector that entrained pulverized coal particles using the Venturi effect. The dependence of entrainment rate on the size of coal particles was studied as a function of the flow rate. Particle Streak Velocimetry performed on coal-laden jets provided valuable insight into the relative velocity of entrained coal particles with respect to the fluid velocity.

High-resolution still images and high-speed videos of laser-sheet light scattered by the coal particles helped determine the mode of interaction of entrained coal particles with the flame front. The effect of combustion on the entrained coal particles was analyzed both in terms of macrostructure and microstructure. Also, the effect of flame on coal-particle size was probed by analyzing the particle size distribution for premixed and non-premixed flames. Loose density measurements and Fraunhofer-diffraction-based particle size distribution measurements were carried out before and after combustion in order to characterize the effect of combustion on the macrostructure of coal particles. Based on the experimental results, it was established that the combustion process did not have any significant effect on the macrostructure of the coal particles. This was evidenced by the negligible changes observed in loose density and mean particle diameter after combustion.

Scanned Electron Microscopy imaging was carried out in order to study the change in microstructure of coal particles as a result of combustion. Remarkable changes were observed in microstructure while there was hardly any change in the macrostructure of coal particles due to combustion. Based on these findings, it was established that the coal particles underwent only partial devolatilization during their passage through the flame due to the small residence time. Hence it was concluded, that this mode of combustion was a surface phenomenon. The effect of oxidizer composition on the combustion of coal particles was studied by comparing the measured particle size distributions for CH_4/air, $CH_4/O_2/CO_2$ and CH_4/O_2 flames.

To my parents and my sister for their unconditional love, endless support and constant encouragement throughout my life.

ACKNOWLEDGEMENTS

It gives me immense pleasure in expressing my sincere gratitude to all those people who have supported me and had made invaluable contributions in making this thesis possible. First and foremost, I would like to express my profound sense of reverence and gratitude to my research adviser Dr. Dimitrios C. Kyritsis for his continuous guidance, support, motivation, patience and untiring help throughout my Masters. His in-depth technical knowledge and unparalleled enthusiasm have always been a source of constant inspiration. His mentorship was paramount in providing a well-rounded research experience. During demoralizing times, he was always there as more than just a mentor: a colleague, a friend and a source of moral support. One simply could not wish for a better or friendlier adviser. I can state with certainty if not for him, I would have never been able to prosper in this challenging environment. Thanks a lot Professor.

I would also like to thank the other members of the Combustion Physics Group: Farzan Kazemifar, Michael Pennisi, Constandinos Mitsingas, Tom Connelly, Nicholas Traina and Anna Oldani for their invaluable expertise and assistance in completing my thesis. I thank them for making this experience pleasant and enjoyable. It has been a pleasure working with you all.

I would like to express my gratitude to Keith Parrish for his technical support in building my experimental setup. Additionally I would like to thank the staff of Fredrick Seitz Materials Research Laboratory Central Facilities for helping me with SEM analysis.

Last, but not least, I would like to thank my parents Rajasegar & Saraswathi, my sister Raajashri and all my friends for their immense love and support throughout my life, making it possible for me to be here right now. A special thanks to Vidya Ravi, A.P. Prasanth and Pranava Swaroopan who have always been there for me in my most agonizing times, loved, supported, encouraged, entertained and helped me get back on my feet in the most positive way. Thank you all.

TABLE OF CONTENTS

LIST OF SYMBOLS vii

CHAPTER 1: INTRODUCTION 1

1.1 Motivation 1

1.2 Pulverized Coal Combustion and Coal-Dust Flames 1

1.3 Particle Laden Jet Flames 4

1.4 Oxy-Coal Technology 6

1.5 Research Objectives 8

CHAPTER 2: EXPERIMENTAL APPARATUS 10

2.1 Coal Sizing and Loose Density Measurement 10

2.2 Coal Particle Laden Jet 11

2.3 Diffusion and Premixed Flames 12

2.4 Particle Size Measurement (Pre and Post-Combustion) 14

2.5 High-Speed Visualization 18

2.6 Particle Streak Velocimetry 21

2.7 SEM Imaging 22

CHAPTER 3: RESULTS & DISCUSSION 26

3.1 Effect of Combustion on Loose Density 26

3.2 Effect of Particle Size on Entrainment Rate 28

3.3 Particle Streak Velocimetry 37

3.4 Combustion Phenomenology 43

3.5 Particle Size Analysis 55

3.5.1 Effect of Optical Properties of Coal on Particle Size Measurement 55

3.5.2 Diffusion Flame 58

3.5.3 Premixed Flame 72

3.6 SEM Analysis 75

CHAPTER 4: SUMMARY, CONCLUSIONS & RECOMMENDATIONS 88
4.1 Summary and Concluding Remarks 88
4.2 Recommendations for Future Study 90

LIST OF REFERENCES 92

APPENDIX A: ROTAMETER CALIBRATION 96

APPENDIX B: PERSPECTIVE VIEW AT 45° TO LASER SHEET 98

APPENDIX C: PARTICLE SIZE DATA 100
C.1 Malvern Bin Size 100
C.2 Particle Size Distribution before Combustion 101
C.3 Particle Size Distribution after Combustion (CH_4 Diffusion Flame) 112
C.4 Particle Size Distribution after Combustion (CH_4/air Premixed Flame) 123
C.5 Particle Size Distribution after Combustion ($CH_4/O_2/CO_2$ Premixed Flame) 125
C.6 Particle Size Distribution after Combustion (CH_4/O_2 Premixed Flame) 127

LIST OF SYMBOLS

m_p	Mass of particle phase
m_g	Mass of gas phase
ML	Mass loading or Particle loading
Stk	Stokes number
τ_p	Particle relaxation time or Particle stoppage time
τ_f	Flow time scale
ρ_p	Density of the particle
d_p	Diameter of the particle
U	Fluid velocity
μ	Dynamic viscosity of the fluid
L	Characteristic length
D_L	Lower particle diameter
D_U	Upper particle diameter
D_M	Mean particle diameter
φ	Porosity or Void fraction
V_V	Total volume of void spaces
V_T	Bulk volume
PCF	Pressure correction factor
TCF	Temperature correction factor
P	Operating pressure
P_o	Calibration pressure
P_g	Gauge pressure
T	Operating temperature
T_o	Calibration temperature
Q_o	Volumetric flow rate under standard conditions
Q'	Corrected volumetric flow rate
Φ	Equivalence ratio
n	Refractive index of the particle

CHAPTER 1

INTRODUCTION

1.1 Motivation

It is a well-established fact that energy generation from combustion of fossil fuels results in significant emission of greenhouse gases, the dominant contributor being CO_2. The awareness about the increase in greenhouse gas emissions have led to various international legislation policies like the Kyoto protocol and the Intergovernmental Panel on Climate Change regarding the reduction greenhouse gas emissions in most economically well developed countries [1]. It is well known that the use of alternative energy sources like nuclear power and renewable energy can significantly reduce the greenhouse gas emissions associated with energy production. Though the potential for renewable energy sources is expected to increase tremendously with our ever increasing future energy demand, the total contribution of these renewable energy sources in terms of total energy produced is significantly less when compared to conventional sources of energy like fossil fuels [2]. Since renewable energy sources hold hope for reducing greenhouse gas emissions only in an extremely long time frame, it is likely that coal will remain in an important position in the energy demand for the foreseeable future owing to its proven stability in terms of supply and cost [3]. This renewed interest has led to recent developments in coal combustion technologies over the past decade dealing with oxy-fuel combustion to obtain a steady stream of nitrogen free flue gas that is ready for carbon sequestration [4].

1.2 Pulverized Coal Combustion and Coal-Dust Flames:

Pulverized coal combustion came into existence on account of their relatively high combustion intensities (0.5-1.5 MW per m^2) and high heat transfer rates per unit surface area of the fuel (0.1-1.0 MW per m^2) which made them superior to fluidized bed combustors [5]. The underlying principle of pulverized coal combustion is fairly well understood and can be broadly divided into four major steps: heating up of pulverized coal particles, devolatilization, volatile combustion and the burning of char.

Though heating-up of coal particles is a fairly simple process, there are difficulties involved in defining the heat transfer quantitatively either by using convection or radiation phenomena and in determining the specific heat capacity of the coal particles [6]. As the process of devolatilization commences, mass transfer starts interfering with heat transfer rates i.e., due to the sudden efflux of volatiles, there is a drop in temperature in the immediate vicinity of the un-ignited particles and also an outward radial velocity against which the heat has to be conducted to the coal particles from the surrounding gas [5]. Devolatilization is not a completely homogenous process as the material is ejected by 'jetting' from pores or blow-holes with recorded velocities up to 1 m/s. It is commonly assumed that volatiles burn via the following steps:

$$\text{Volatiles} + O_2 \xrightarrow{\text{yields}} CO + H_2O \tag{1.1}$$

$$CO + 0.5\,O_2 \xrightarrow{\text{yields}} CO_2 \tag{1.2}$$

The rates of the reaction are determined by the rates of mixing and the thermo-chemistry i.e., the heat of combustion of the volatiles determines the flame temperature. The flame structure is determined by the air-flow patterns and the rate of chemical heat release. For coal flames, this is a function of the air velocity, the amount of excess air and the size of pulverized coal particles [7]. The process of char combustion is not completely understood and is further complicated by the influence of particle size, char mineral content and fragmentation of char particles during combustion. The rate limiting step in the combustion of char particles can be chemical reactions or gaseous diffusion to the particles or a combination of these two factors [8].

Combustion of pulverized mixtures poses a series of intriguing theoretical challenges. In particular, many materials that are non-flammable in their bulk form become highly reactive and even explosive if dispersed as a cloud of very fine particles in air, due to significant increase in surface area for enhancing mass and heat transfer processes. Hence from a combustion perspective, it becomes necessary to investigate such phenomena as they can be both a benefit and hazard. Kenneth [9] measured the minimum explosible concentration, maximum explosion pressure, maximum rate of pressure rise and minimum oxygen concentration for coal explosion in mines. The minimum explosible concentration refers to the minimum concentration of airborne dust particles in a gas mixture below which a deflagration cannot propagate after it has been initiated by a sufficiently strong ignition source. It was determined that the particle size and volatility were the most important parameters in determining the explosion hazard. Paul and co-workers [10] investigated the ignitability characteristics of coal-dust and coal-dust admixed with methane. It was observed that the lean flammability limit decreased with increasing ignition energy and methane concentration. Hertzberg et al. [11] observed that above certain characteristic diameter of the coal particle, the lean limit concentrations increased significantly with increasing particle size until a critical size was reached, above which the coal-dust was non-flammable for any concentration at ambient temperature and pressure. It was reported that both the characteristic diameter and the coarse size limit of flammability (critical diameter) increased monotonically with increasing coal-dust volatility and increasing oxygen content in the dispersing gas. Also Scanning Electron Microscopy (SEM) analysis performed on the coal particles before and after combustion revealed structural changes in coal particles as result of their participation in coal-dust explosions. It was observed that char residues that are pockmarked with blow-holes are typical of such coal-dust explosions. Also, the char residues fused into large agglomerated masses with increasing coal-dust concentration during the explosion.

One of the fundamental properties which control the intensity of a coal-dust explosion is the burning velocity, i.e., the velocity normal to the flame front at which the flame propagates relative to the burnt mixture. Over decades, various thermal theories have been put forth in order to evaluate the burning velocity of a planar laminar premixed coal-dust flame. Ogle et al. [12] compared the burning velocities obtained using the Radiation-Convection-Conduction model (RCC) and the Radiation-Convection model (RC) against the Mallard Le Chatelier model (ML) [13] and the Mallard Le Chatelier model with Radiation (MLR) [14]. It was concluded that the conductive heat flux was negligible when compared with the contributions due to convection and radiation, this was substantiated by that the difference between the predicted burning velocity for the RC and RCC models was on the order of 0.01 %. Also, the ML model was found to be entirely inadequate as radiative flux cannot be ignored while computing the burning velocity.

Hordon and co-workers [15] used a flat flame burner to study the atmospheric flame velocities in coal-dust and air-systems. The flame velocity was determined to be a function of particle size, coal concentration and volatility. Krier et al. [16] reported the fundamental lean limit coal-dust concentration and the burning velocity as a function of coal-dust concentration while observing coal-dust flames propagating in a horizontal flammability apparatus called the Gravity Tumbler Flammability tube (GTFT). Liu et al. [17] studied the flame propagation in a hybrid mixture of coal-dust and methane. It was observed that the presence of methane along with coal-dust improved the flame propagation speed and maximum flame temperature significantly when compared to single-coal dust flames. It was also reported that the flame front temperature varied with the coal-dust concentration.

There has been significant progress made in the study of fundamental aspects of coal-dust flames. The basic theory [5-8,12-14] underlying particle combustion has been well established and considerable amount of work carried out in the past has been focused on studying the effect of various parameters [9-11, 15-17] i.e., particle size, concentration and volatility on the burning velocity. But however, this field is still dominated by empiricism, due to the lack of supporting literature based on studies utilizing modern diagnostic tools, i.e., particle sizing, SEM etc., for studying pulverized coal combustion.

1.3 Particle Laden Jet Flames

Non-reactive jet flows that are laden with condensed-phase particles occur in a variety of natural and technological systems. These non-reactive jet flows can be subdivided as gas-solid and gas-droplet flows. The main difference between the two flows is that mass transfer does not occur in the former but occurs in the latter. The gas-particle flows are characterized by mass loading or particle loading which is defined as follows:

$$ML = \frac{Mass\ of\ paricle\ phase}{Mass\ of\ gas\ phase} = \frac{m_p}{m_g} \qquad (1.3)$$

The particles can be treated as passive contaminants when the mass loading ratio of the particles is small. In turbulent gas-particle flows, turbulence modification can be expected to be negligible if the particle diameter is much smaller than the Kolmogorov scale. However, when the particle mass loading ratio is increased, global turbulence modifications may be induced. If the particle diameter is larger than the Kolmogorov scale, the particle affects the energy distribution of the surrounding fluid [18]. An important dimensionless parameter which characterizes the gas-particle flows is the Stokes number [19] which is defined as follows:

$$Stk = \frac{Particle\ relxation\ time}{Flow\ time\ scale} = \frac{\tau_p}{\tau_f} \tag{1.4}$$

$$Stk = \frac{\rho_p d_p^2 U}{18\mu L} \tag{1.5}$$

This dimensionless number determines how well the particles follow the motion of the surrounding gas. For small Stokes number (Stk $\ll$ 1), the particles can be considered to move with the same velocity as the carrier fluid. For large Stokes number (Stk $\gg$ 1), the particles do not follow fluid velocity, and this leads to significant momentum transfer from the particle to the fluid or vice-versa.

Wagenknecht and Bohnet [20] were the first to study an injector type particle-feeder in order to create a gas-particle flow. They used a high velocity air stream issuing from a primary nozzle that entrains the particles into a secondary nozzle, where the necessary pressure is built up for conveying the particles. Most solid-particle injector designs relied on a nozzle that created a high velocity air flow which in turn carried the solid particles. Xie et al. [21] developed a vertical solid-particle injector that utilized the Venturi effect i.e., the pressure drop in the air flow across an orifice plate placed in a circular pipe was used to naturally entrain micron-sized solid particles such as coal-dust.

Xie et al. [22] also studied the interaction of entrained coal-dust particles in lean methane-air premixed flames. They analyzed the laminar burning velocity of the coal-dust methane-air mixture by capturing shadowgraph images of the flames and processing them using the cone-angle method. Two competing effects namely volatile release and heat sink effect of the coal particles affected the flame temperature and the burning velocity. The volatile release increases the overall equivalence ratio and thus the flame temperature and burning velocity while heat sink effect i.e., the heat taken up by the coal particles to release the volatiles reduces the flame temperature and thereby the burning velocity. Frachetti and co-workers [23] employed Large Eddy Simulation (LES) to pulverized coal jet flames that presented good agreement of the computational results with the experimental data for both reactive and non-reactive case. Scott et al. [24] analyzed the effect of coal-dust on premixed turbulent methane-air flames on a new experimental platform using the Hybrid Flame analyzer (HFA) to measure the burning velocity. It was reported that the coal particles usually increase the turbulent burning velocity. Smaller particle sizes and larger concentrations were found to increase the turbulent burning velocity significantly when compared to larger particle sizes and lower concentrations.

Preliminary studies on the combustion of coal particles entrained in premixed methane-air flames [22, 24] have been carried out. However studies regarding the combustion phenomenology i.e., the mechanism of interaction of solid particles with the flame front and the particle morphology pre and post-combustion are absent from the current literature for entrained coal particles in premixed methane-oxygen flames. Further no information is available on the interaction of coal particles entrained in pure methane diffusion flames. Also there is no background on the fluid mechanics happening during the interaction of coal particles with the flame in terms of particle and flow velocity as a function of Stokes number.

1.4 Oxy-Coal Technology

Conventional pulverized coal-fired boilers use atmospheric air for combustion in which the nitrogen from the air (approximate 79 % by volume) dilutes the CO_2 concentration in the flue gas. The cost involved in capturing CO_2 for carbon sequestration from such dilute mixtures using amine stripping or membrane-based separation technologies is substantial [25]. As the largest portion of the remaining flue gas consists of the atmospheric nitrogen introduced into the process with the combustion air, holding back this nitrogen before combustion ensures a significant increase in the CO_2 concentration. Thus the underlying principle of oxy-coal combustion is to extract the nitrogen from the combustion air prior to combustion thereby feeding virtually pure oxygen to the combustion process [26]. In oxy-coal combustion, the pulverized coal is burnt using an oxidizer which is a combination of 95 % pure oxygen by volume and recycled flue gas. Using this process, the flue gas generated which is a mixture consisting mainly of CO_2 and water vapor is ready for CO_2 sequestration after simple purification and compression without the use of expensive amine stripping technology used for separating CO_2 from the flue gas. The recycled flue gas mixed along with fresh oxygen is used to control flame temperature.

Due to the fundamental change in the oxidant used for combustion and the consequent change in the furnace gas environment, the oxy-coal technology affects the combustion process of pulverized coal and the associated processes like heat transfer and combustion chemistry. Numerous studies and research projects have been carried on focusing on many scientific and engineering fundamental issues of oxy-coal combustion including: recycled flue gas ratio, ignition, flame stability, heat transfer, combustion characteristics, and pollutant formation and reduction [27].

Oxy-coal combustion combined with CO_2 sequestration from flue gases is a near-zero emission technology that can be adapted to both new and existing pulverized coal-fired power plants. CO_2 sequestration is an area of ongoing active research, but for all CO_2 sequestration techniques, the energy requirement for CO_2 compression is reduced with increasing purity of CO_2. In oxy-coal combustion, the concentration of CO_2 in the flue gas is increased from approximately 17 % to 70 % by mass, thus making it a suitable candidate for carbon sequestration [4].

Though oxy-coal technology is undergoing rapid development towards commercialization, there are no full scale power plants using oxy-coal combustion in operation. However, theoretical studies combined with laboratory and pilot scale studies have provided an understanding of the relevant design parameters and operational issues. The Vantenfall project in Germany, the Callide project in Australia, the Clean Environment Development Facility (CEDF) Pilot in Ohio, USA are a few of the large scale (30 MW thermal) operational pilot plants employing oxy-coal technology which are used for validating the prospects of commercializing this technology [28].Wall et al. [29] provided a comprehensive overview on the most recent developments in pilot plants and demonstration projects worldwide for oxy-coal Carbon Capture and Storage (CCS) technology. The summary of the major semi-industrial scale and demonstration plant studies undertaken during the past decades is presented in Figure 1.1.

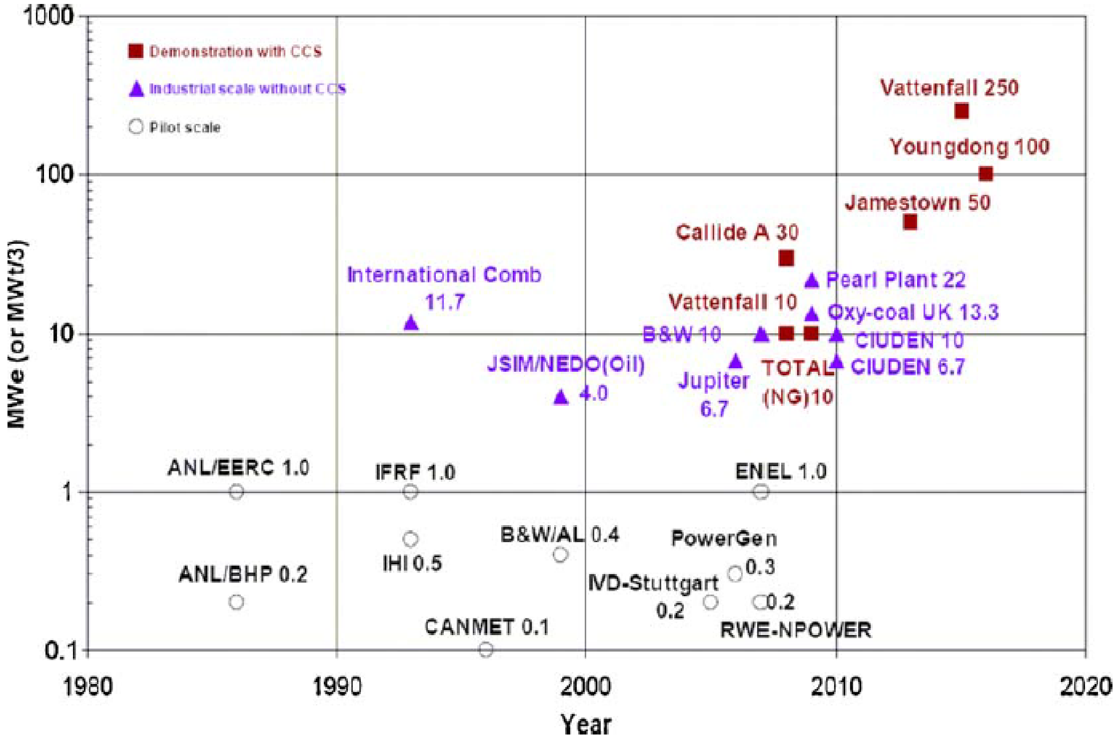

Figure 1.1: Historical progression of the scale of oxy-fuel pilot-plants and demonstrations [29].

1.5 Research Objectives

The present study focuses on the interaction of coal particles with diffusion and premixed flames. The overarching goal of this thesis is to establish the flame phenomenology and combustion morphology of the coal particles, before and after combustion as a function of particle size for diffusion and premixed flames. In order to achieve this goal, the following research objectives were pursued:

- Establish a particle seeding technique to entrain coal particles in a free jet stream.
- Use Particle Streak Velocimetry (PSV) to compare particle velocity to actual flow velocity.
- Characterize flame phenomenology using high-speed videos.

- Characterize the combustion morphology by studying the loose density and the particle size distribution of pulverized coal using Malvern diagnostic tool before and after combustion.
- Analyze particle morphology before and after combustion using Scanning Electron Microscopy (SEM).

Overall a seminal study was pursued that to my knowledge provided first-hand information about the interaction of coal particles entrained in diffusion and premixed flames on the basis of particle morphology and flame phenomenology for various particle sizes.

CHAPTER 2

EXPERIMENTAL APPARATUS

2.1 Coal Sizing and Loose Density Measurement

Coal samples were procured from Southern Illinois Power Cooperative. The samples consisted of milled coal meant for cyclone boilers. The coal samples had a varying size distribution ranging from huge lumps with a characteristic dimension of 1 cm to very fine coal dust, so they had to be graded according to particle size before being used in experiments. The coal particles were graded according the particle size by passing them sequentially through USA Standard 3’’ diameter sieves procured from Dual Manufacturing Co., Inc. 11 different samples with particle size ranging between 1000 μm to 178 μm were then used for further investigation. The details of the sieve analysis performed on the coal particles can be seen in Table 2.1 below. The loose density of the particles was then computed by accurately measuring the weight of a fixed volume of coal samples namely 100 cc using an Ohaus JR120 Precision Standard Electronic balance.

Sample No.	Sieve Number	Diameter Upper Limit D_U (μm)	Diameter Lower Limit D_L (μm)	Mean Diameter D_M (μm)
1	18 - 20	1000	853	927
2	20 - 25	853	710	782
3	25 - 30	710	600	655
4	30 - 35	600	500	550
5	35 - 40	500	422	461
6	40 - 45	422	354	388
7	45 - 50	354	297	326
8	50 - 60	297	251	274
9	60 - 70	251	211	231
10	70 - 80	211	178	195
11	< 80	178	178	178

Table 2.1: Sieve analysis of pulverized coal samples.

2.2 Coal Particle Laden Jet

Based on the work of Xie et al. [21], a vertically oriented solid particle injector was designed in order to create a coal particle laden jet. This particular injector utilized the Venturi effect in order to entrain particles inside the jet stream. The Venturi effect in this case was established by allowing the flow to pass through an orifice plate, resulting in an increase in the flow velocity and thereby causing a pressure drop which was utilized to seed coal particles onto the flow. The injection rate can simply be controlled by adjusting the flow rate and thereby modifying the pressure drop associated with the flow that drives the entrainment phenomenon.

The schematic layout of the solid particle injector designed for the experiment is show in Figure 2.1. A small orifice plate was machined out from an aluminum slab, which had a hole of 1 mm diameter placed centrally. This orifice plate was then mounted centrally with the help of compression springs onto a steel tube with an outer diameter of 12 mm, inner diameter of 11 mm and a length of 300 mm. Three circular holes 5 mm in diameter were drilled such that they were radially equi-spaced on the periphery of the steel tube just above the location of the orifice plate, so as to enable coal particles to be fed easily into the orifice plate for entrainment

A particle feeder arrangement namely a hopper device comprising of a hollow 60° inverted cone made of acrylic was attached to the steel tube with the help of socket screws. The socket screws helped to adjust the position the hopper arrangement on the steel tube relative to the position of the holes on the periphery of the steel tube. The feeder was made of acrylic so as to ensure a smooth sloping inner surface to minimize frictional losses in the assembly. The hopper arrangement was fitted with a Burgess Vibro-Graver Model 74 electric engraver to create vibrations and thereby start the entrainment process. This ensured that the particles did not agglomerate and thereby resulted in a smooth movement towards the holes on the periphery once entrainment was established. The hopper arrangement was also fitted with a lid made from acrylic that served as particle collection pan once the flow was laden with coal particles. This allowed collection of coal particles once they are entrained in the flow. The entire arrangement was secured an optical bench using suitable clamping and supports. For the purpose of entrainment studies, air supply fed into the steel tube was monitored using Omega FL-3840 G rotameters.

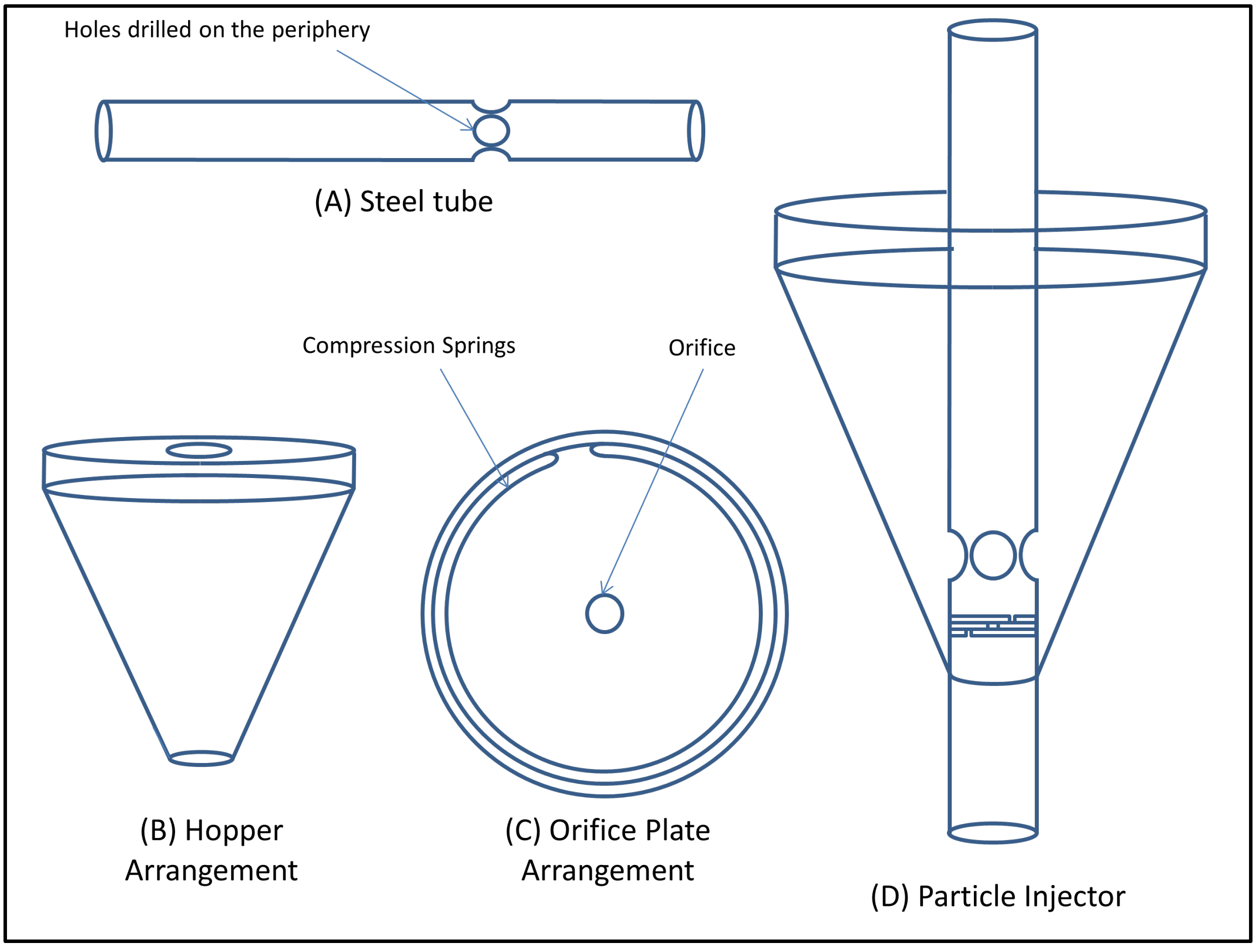

Figure 2.1: Schematic layout of the solid particle injector.

2.3 Diffusion and Premixed Flames

The steel tube of the solid particle injector assembly was then fitted with a suitable arrangement so as to ensure smooth supply of gaseous fuel (methane), oxidizer (air/oxygen) and diluent (nitrogen/carbon-di-oxide), the flow rates of each of these gases can be controlled individually using Omega rotameters. A very fine wire mesh was inserted into the steel tube below the orifice plate that served the purpose of a flame arrestor in case of a flashback happening inside the tube. In addition to this, the orifice plate itself offered some level of protection against flash back owing to the small size of the hole (1 mm in diameter).

Methane and nitrogen/carbon-di-oxide supply were controlled using Omega FL-3839 ST while air/oxygen flow rate was controlled using Omega FL-3840 G rotameters. This arrangement ensured that a diffusion flame or a premixed flame of desired strength can be set up at ease for the purpose of experimentation. Nitrogen was used as a diluent in the diffusion flame to prevent the luminescence caused by soot that interfered with flow visualization. Also it helped in stabilizing the flame at the top of the steel tube and in increasing the total flow rate so as to get sufficient particle entrainment without having to increase the supply of the fuel. The experimental setup for the study of coal-laden jets in diffusion and premixed flames is presented in Figure 2.2.

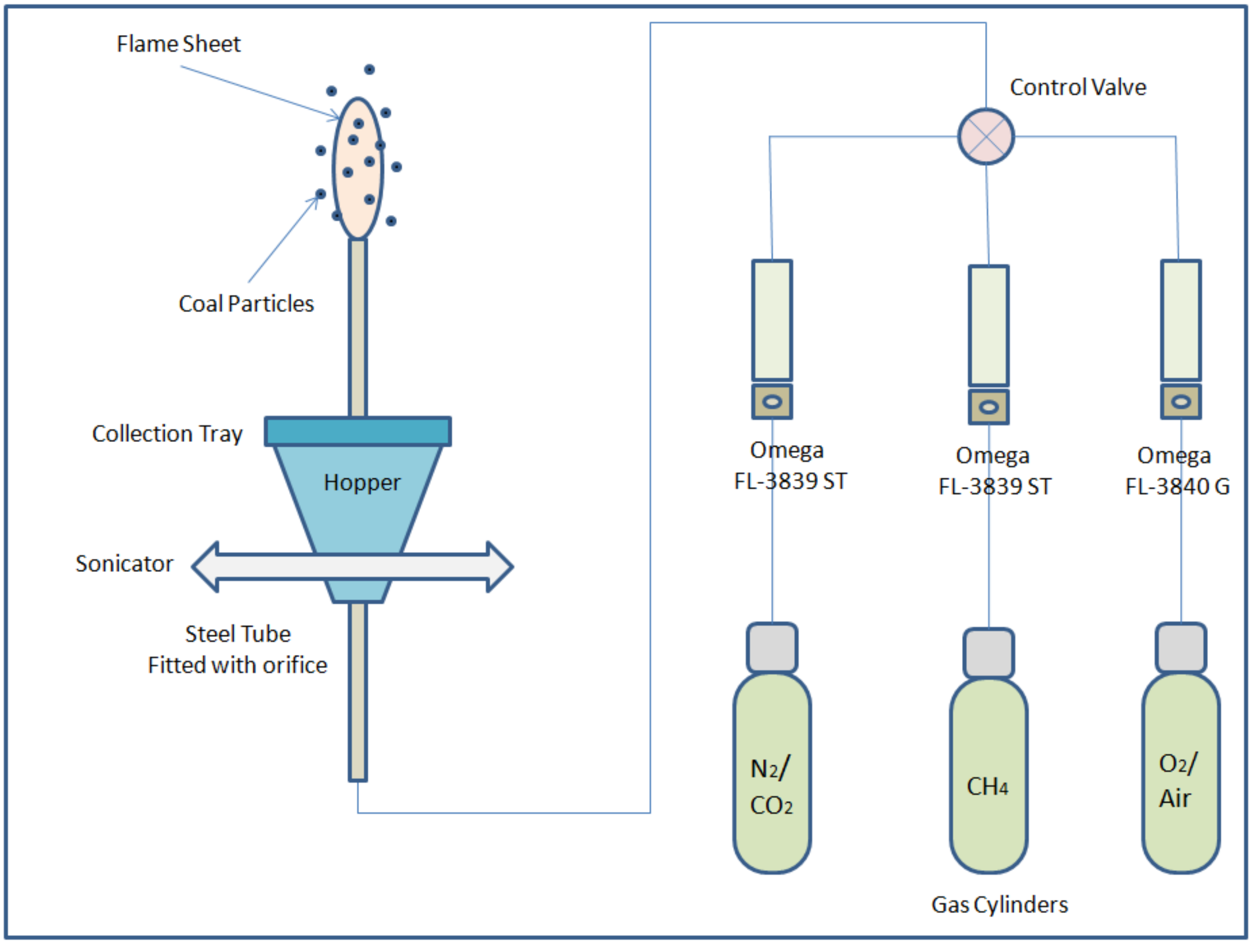

Figure 2.2: Schematic layout of the experimental setup used for coal-laden diffusion and premixed flames.

2.4 Particle Size Measurement (Pre and Post-Combustion)

The schematic layout of the experimental setup used for particle size measurement is shown in Figure 2.3. The particle size distribution of the different coal sample before and after combustion was obtained using a Malvern RT 97 Spraytec droplet-size measurement instrument. The Malvern system can compute particle size distribution based on the complete Mie theory or can use the Fraunhofer approximation technique, which is actually a simplified version of the Mie theory. The Fraunhofer approximation assumes the particles whose size is being measured are opaque and hence no input of the refractive index of the particles is required. This being a crude approximation has proved to be erroneous when used for droplet-size measurement involving transparent droplets i.e, sprays, and aerosols [30]. Hence, for such measurements, it is always preferable to base the particle size measurement on the full Mie theory which requires the refractive index of the particles as one of the inputs. Since the coal particles were opaque as such, the value of refractive index did not have any significant effect on the particle size distribution; so it was reasonable to use the Fraunhofer approximation. The refractive index of the coal particles was set to the system default opaque refractive index of 1.5+0.50i and 1+0.00i for the refractive index of the surrounding medium namely air [31, 32].

The Malvern system uses a 670 nm He-Ne laser beam and a set of 31 concentric circles as the detector system for particle size measurement. The amount of light scattered from a particle is inversely proportional to the characteristic length of the particle. As the laser beam is directed across the test section, the particles scatter light and this scattered light is focused onto the detector system through a 200 μm-diameter pin-hole for analysis. Relying on the principles of Mie scattering, the Spraytec feeds data into the v5.6 of the RT Sizer software package for analysis.

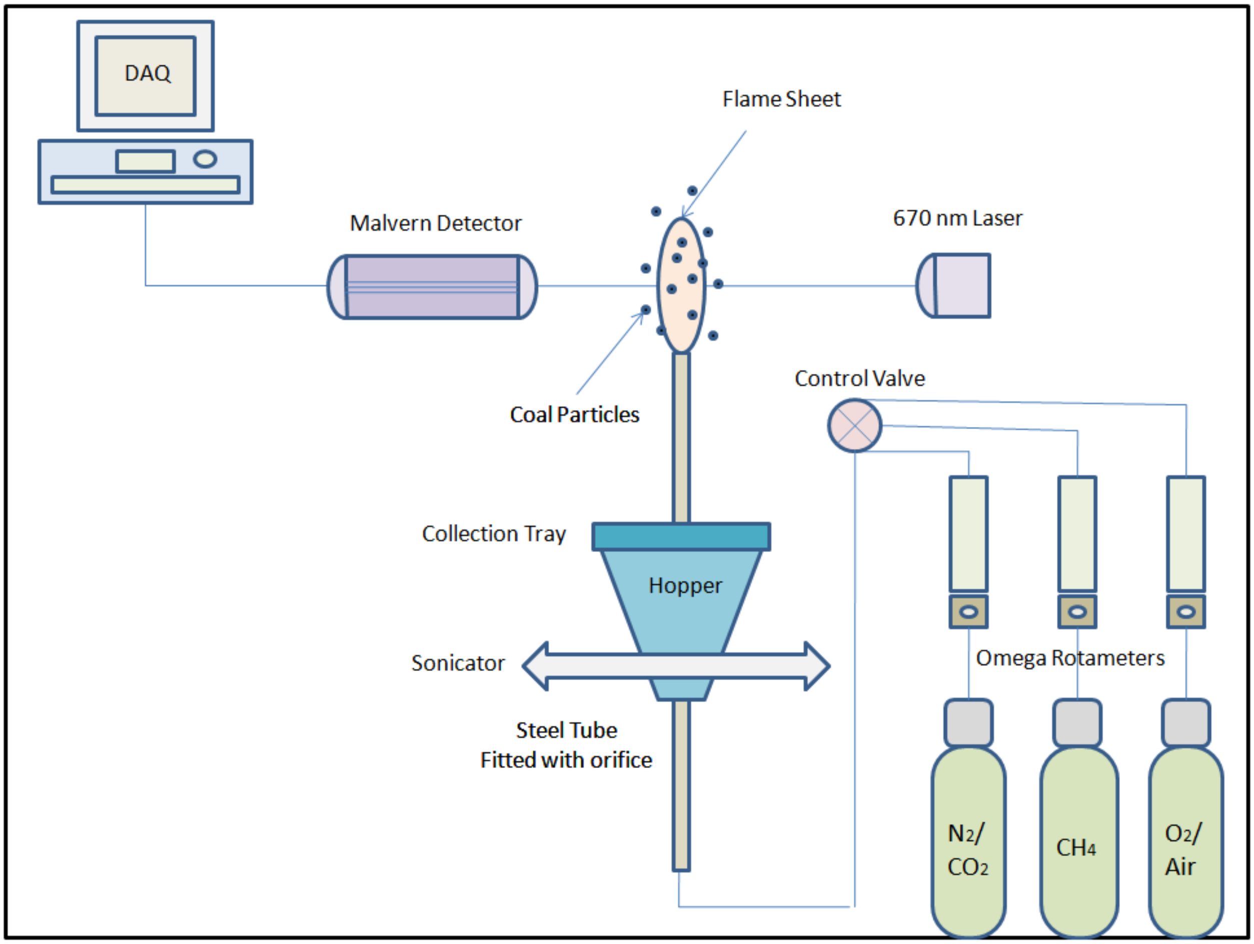

Figure 2.3: Schematic layout of the experimental set up used for particle size measurements.

Before every experiment was conducted, a background signal was collected using an empty test section without the coal-laden jet. The background signal served as a reference for the particle size distribution analysis and hence it was essential to record the background every time in close proximity to the actual test. When the test section was empty, the laser was transmitted without any scatter onto the detector system. Hence, the signal intensity on the central ring of the detector system, namely ring 1, was to be above 1500 a.u., while the signal levels on the other rings are to stay at a minimal value. The transmitted signal intensity was measured in terms of a number on an arbitrary scale unit (a.u.) that quantified the strength of the signal. A value of around 1500 a.u. corresponded to a very strong signal but a signal of 2000 a.u. or above, flooded the detector and hence resulted in a saturation warning. A typical background signal from the Malvern system is shown in Figure 2.4.

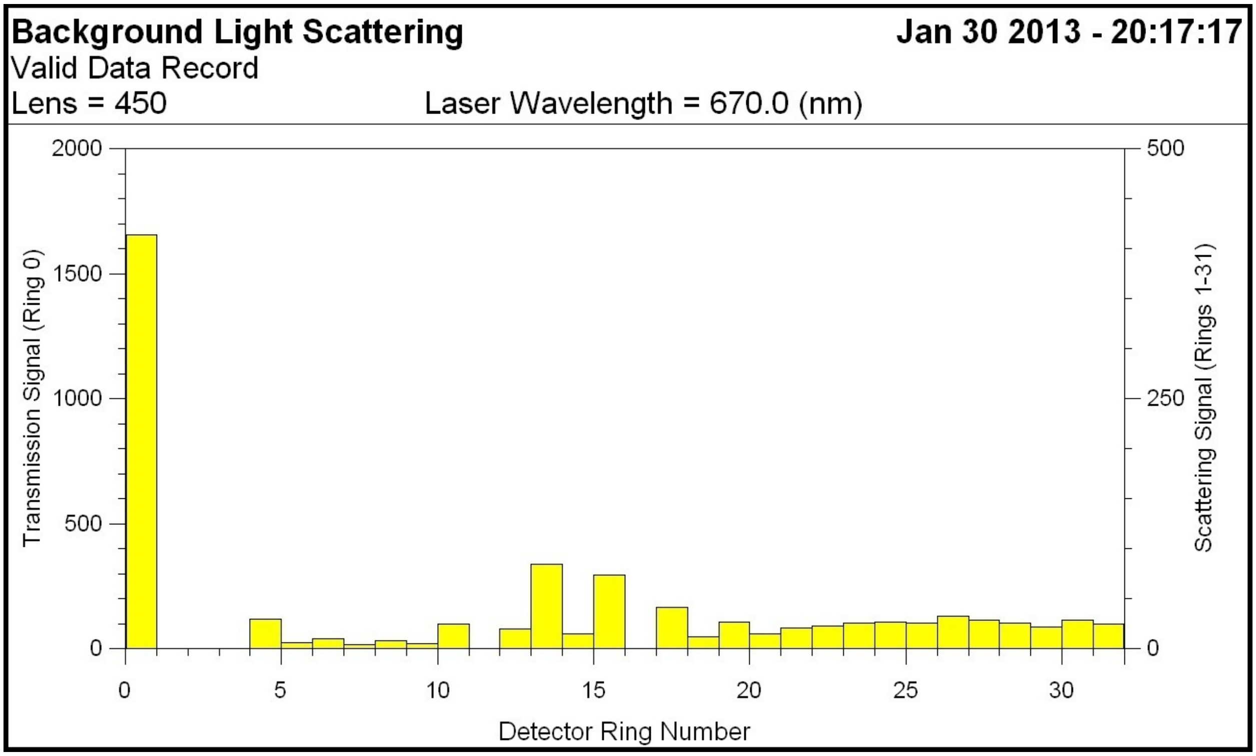

Figure 2.4: Typical background signal for the Malvern Spraytec system in the RT Sizer program.

In case of a drop in the signal level in the central ring below 1500 a.u., the system had to be aligned before further experiments can be conducted. The alignment was done by releasing the four lock nuts on the detector side and then sequentially moving the horizontal and vertical alignment screws so as to sweep across the entire detector systematically. The aim of this adjustment is to align the 200 μm-diameter pin-hole exactly with the center of the laser beam such that the signal intensity on the central ring is maximum (above 1500 a.u.) with the test section empty. In order to improve the quality of data, once in a while a background noise check was performed. This was similar to the background signal but was recorded with the laser off so that it took into account only the stray light entering into the detector system. A typical noise signal from the Malvern system is shown in Figure 2.5.

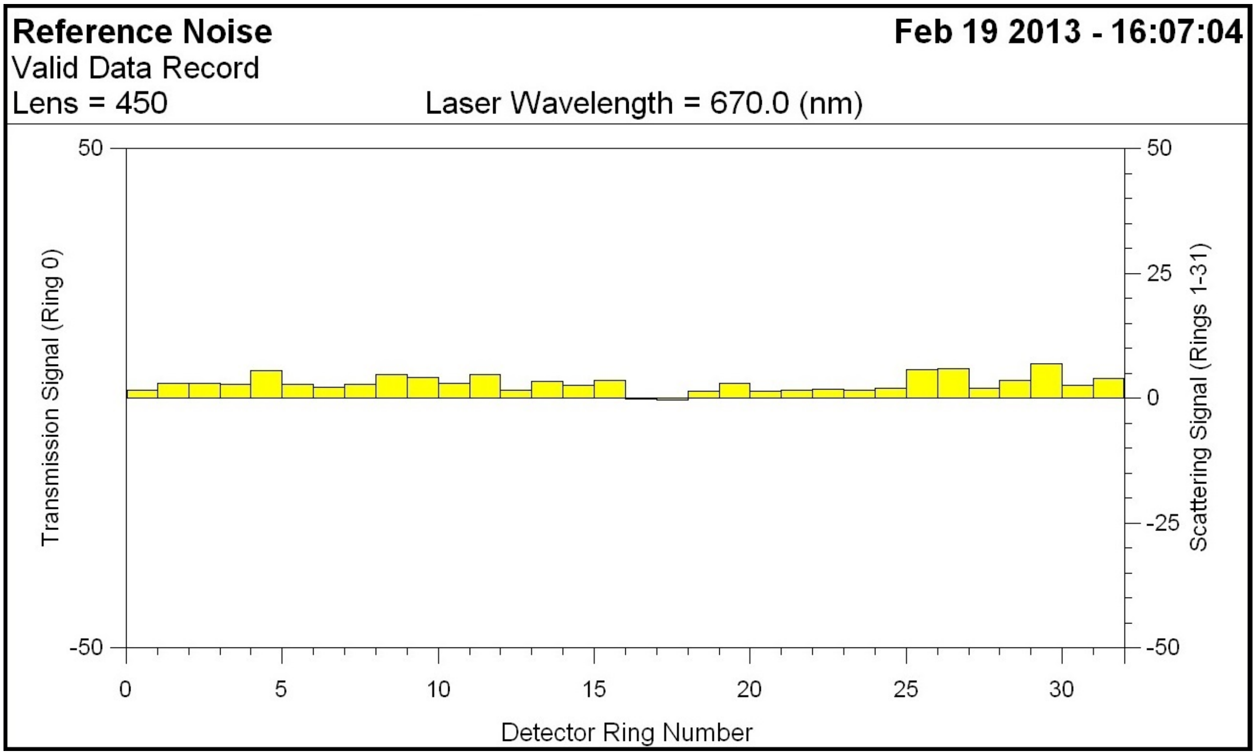

Figure 2.5: Typical noise signal for the Malvern Spraytec system in the RT Sizer program.

Malvern-based size measurements can be performed either in real-time or in a flash mode. The real-time mode provides instantaneous size measurements, while the flash mode that provides averaged data acquired at a user-defined acquisition rate (up to 1000 Hz) over a user-defined acquisition time period. In our case, flash mode measurements were used. Data were acquired at a rate of 500 Hz over a time period of 2000 ms and were used to get the average particle size distributions. In addition to these two parameters, the duty cycle defines the fraction of the total amount of time (acquisition time period) during which a signal is actually acquired. This parameter was set to 20 % by default, but in our case, setting it to 50 % provided better consistency in terms of particle size distribution. Also, to provide ease of data storage, the RT Sizer software can also tag data sets, which can be used to store information regarding the experimental conditions. This tag is written and saved onto the data file and hence can be used for future reference.

Once the data has been acquired, the averaged particle size distribution is stored along with the time history. The time history file is store .pcl format that can be read only by using the RT Sizer program, whereas the averaged particle size distribution (PSD file) can be saved as .csv file (Comma separated values) that can be imported onto Microsoft Excel for post processing. The Malvern presents size distribution in terms of % number and % volume as a function of specified range of particle diameters distributed over various bins of different sizes. For the analysis, instead of the continuous size distribution across the various bin sizes, the data is presented using an average particle diameter representing each bin by considering the average of the upper and the lower limits of each bin.

For the 11 different samples of coal particles, particle size distribution was studied before and after the combustion process by creating a coal-laden jet using the experimental setup described in section 2.2. In order to avoid the effects of beam steering due to presence of the flame, post combustion particle size measurements were not carried out above the flame as the particles cross the flame zone. Instead, the burnt coal particles were collected once they passed through the flame and they were again entrained to create a jet now laden with burnt coal particles, which was used to determine the particle size distribution after combustion.

2.5 High-Speed Visualization

In order to characterize the combustion phenomenology of coal-laden jet flames, high-speed visualization techniques were invoked. A high-speed camera (Phantom v.7.0) capable of 4800 frames per second (fps) at a resolution of 800 x 600 pixels was used to capture high-speed videos. For the purposes of our study, a frame rate around 800 fps was found to provide the best results in terms of optimum balance between exposure time (i.e., signal strength) and frame rate (i.e., temporal resolution).All the visualizations were grayscale i.e., a pixel value of 0 corresponded to a dark signal whereas a value of 255 corresponded to the maximum recorded luminosity. Using a 50 mm f/1.8D Nikkor lens gave sufficient depth of field of the image plane for high-speed videos and occasionally a 105mm f/2.8D Nikkor lens was also used.

Initially a continuous Nd-Yag Wickedlaser E2, 75 mW (Class IIIb), lasing at 532 nm mounted on a ring stand was used as the illumination source. A very fine laser sheet was created using a combination of optical lenses. The laser beam was first directed through a biconvex focusing lens with a focal length of 19 cm and then allowed to pass through a plano-convex cylindrical lens of focal length 119.4 mm. The biconvex lens focused the laser beam in both the X and Y directions into a fine point, while the cylindrical lens spread out the concentrated laser beam in the Y direction alone, thereby creating a laser sheet. By varying the distance between the two lenses, the position of the image plane with respect to the Y direction and the height of the laser sheet can be varied independently. High-speed movies were taken in a direction perpendicular to this laser sheet. The schematic layout illustrating the optical setup for creating a laser sheet is shown in Figure 2.6.

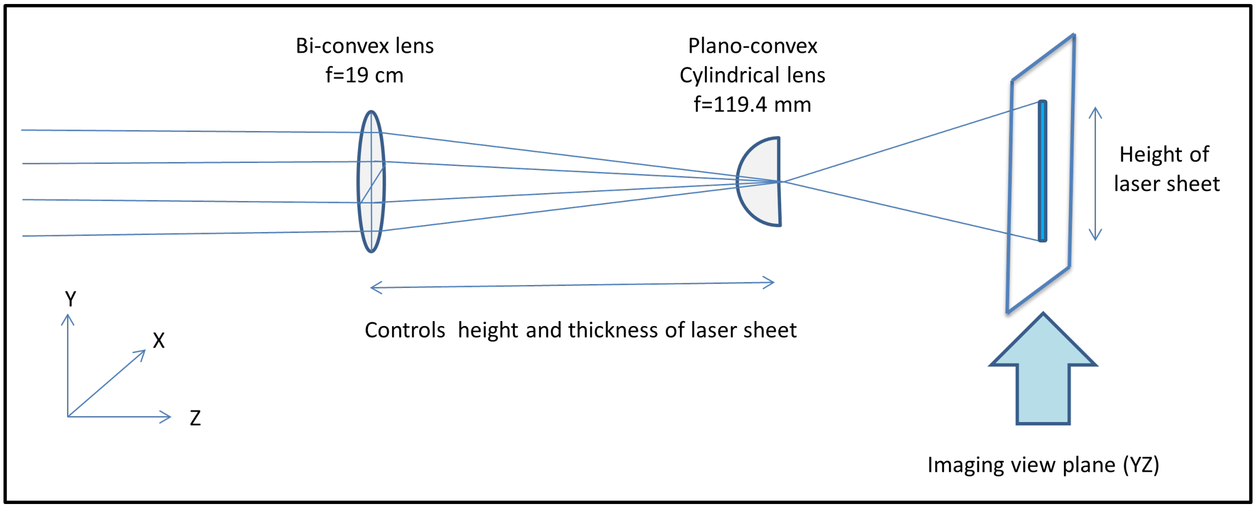

Figure 2.6: Schematic layout of the optical setup used for creating a laser sheet.

The flow was not seeded with any tracing particles (like TiO_2) as such, but it was stipulated that the incandescence caused by the burning of coal particles as they cross the flame front coupled with the light scattered by the particles should provide a signal strong enough to be picked up by the high-speed camera. However a variety of problems was encountered during this phase of flow visualization. Firstly, the diffusion flame proved to be strongly luminescent as such because of soot formation. This inherent flame luminosity obscured any incandescence or scatter from the coal particles. In order to overcome this, a narrow band pass filter was used.

Videos taken using an Andover Corporation 532 1.0±0.2 nm band pass filter attached to the Nikkor camera lenses reduced flame luminosity but the scattered signal from the particles could not be distinguished and hence the idea of using a narrow band pass filter was dropped.

As an alternative solution, the use of nitrogen gas as a diluent in the diffusion flame was considered in order to reduce soot formation and thereby eliminate flame luminosity. Also, using nitrogen could increase the overall flow rate without increasing the height of the flame, resulting in an increased pressure drop through the orifice and thereby entraining more coal particles onto the jet, as explained in section 2.3. By using controlled quantities of nitrogen, a non-luminous blue flame could be stabilized at the tip of the steel tube in diffusion mode. This improved the quality of signal in the high-speed videos but nevertheless the signal due to the scatter from the coal particles seemed to be too weak to provide any valuable insight about the interactions of the solid particles with the flame front.

Hence, it was decided to use an Argon Ion Laser as a stronger source of illumination instead of the Wickedlaser E2 so as to achieve a strong signal caused by the scatter of laser from coal particles that can be easily captured by the high-speed camera. A Spectra Physics Stabilite 2017 Argon Ion 6 W laser with a multi-line output mainly at 457nm, 488nm, and 514nm was used with the same optical setup as described in section 2.5, in order to create the laser sheet for high-speed imaging. The laser beam from the Argon Ion laser was controlled using an aperture and steered into the optical arrangement by a combination of two prisms mounted on translational stages. The prisms helped in steering the beam to the required height and also aligning the position laser sheet with respect to center of the burner at ease. Also, a Fotodiox Canon EOS Macro Extension Tube Set Kit for Extreme Close-up was used along with the high-speed camera to mount the camera lenses in order to zoom into an area of interest within the flame zone. This configuration resulted in a stronger signal of scattered light. Together with the chemi-luminescence from the flame, it proved to be optimal for our case in visualizing the flow field and thereby providing intricate details about the combustion morphology of coal-laden flames. The schematic layout of the experimental setup along with optical system used for high-speed visualization is depicted in Figure 2.7.

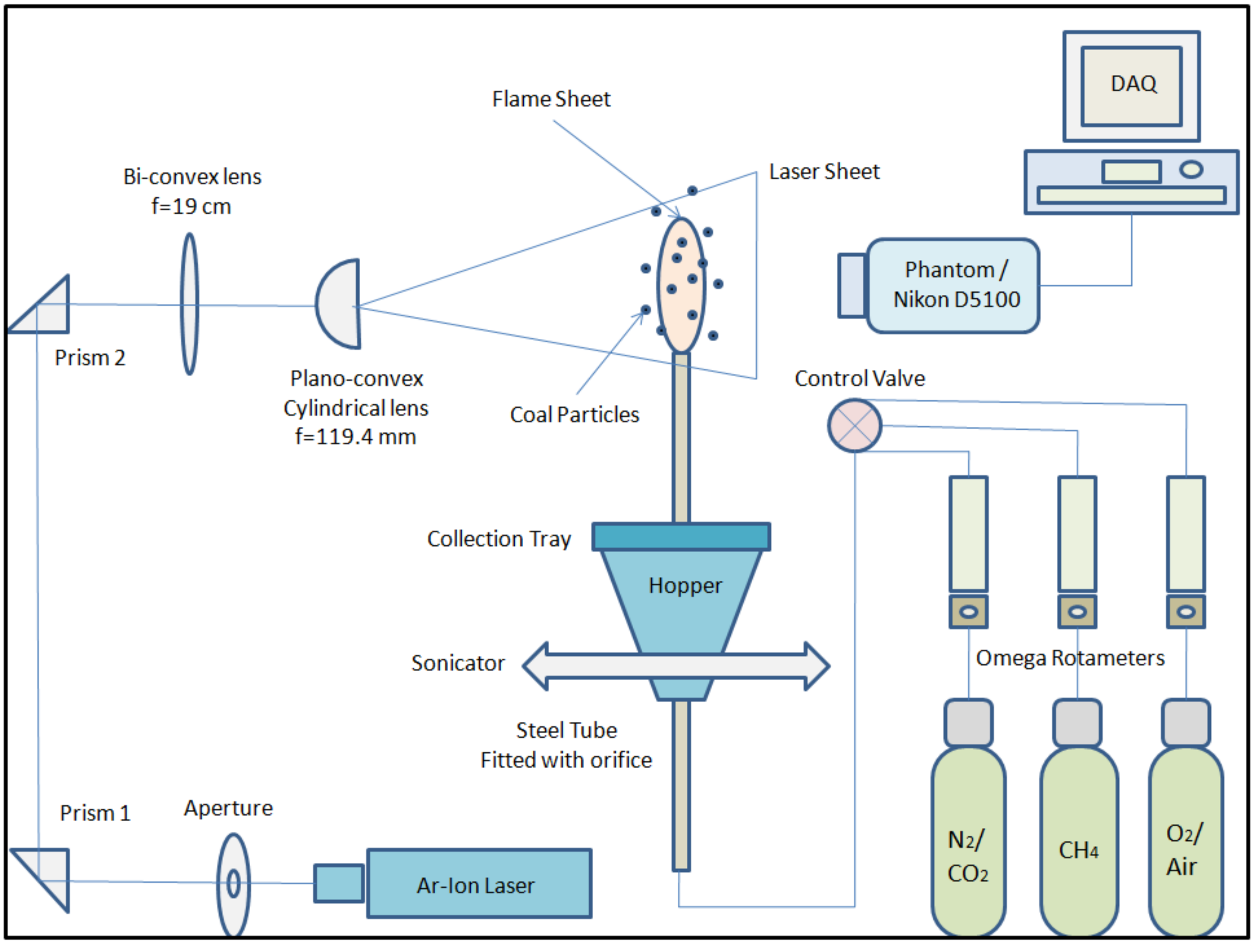

Figure 2.7: Schematic layout of the experimental setup used for high-speed flow visualization.

2.6 Particle Streak Velocimetry

To compute the velocity of the coal particles in the flow field, a technique called Particle Streak Velocimetry (PSV) was used [33]. For this, the same optical setup used for the high-speed flow visualization was employed but the Phantom high-speed camera was replaced by a Nikon D5100 to capture still images and high-definition movies. The camera had a maximum resolution of 4928 x 3264 pixels (16 MP) and shutter speed of up to 1/4000 s. The camera was connected to a workstation and was controlled remotely using the software Control-My-Nikon v4.0. This software seemed to be instrumental in adjusting the various parameters involved i.e., ISO, exposure, in order to obtain a good image suitable for PSV.

The aperture setting was usually set to wide open to capture most of the incandescence and scattered light from the coal particles.

By using suitable long exposure rates, the particles are allowed to travel spatially within a single frame. This results in a streakline which defines the path travelled by a single particle over a known time period equal to the exposure rate. By measuring the length of the streaks, velocity data can be extracted. In order to extract velocity data out of these still images, an open source Java-based software called ImageJ developed by the National Institutes of Health was used. First, a reference length like the known outer diameter of the steel tube was used to correlate the pixels to actual length scale and thereby formulate a reference grid for each image. The images were then inverted such that the grayscale intensity of a pixel corresponding to 0 was set to 255 and vice versa. The "Subtract background" tool was used in order to isolate and highlight the streaks effectively. The contrast and brightness of these processed images were then adjusted suitably in order to enhance the quality of the streaks. The length of each streak corresponded to the distance traveled by the particle during the camera's exposure time. This distance was measured using the "Measure" function as the length of the streakline. Using this information and the exposure time, the velocity of the particles can be calculated. The average flow velocity at the nozzle of the jet can be computed from the flow rate recorded by the rotameters, the cross sectional area of the tube, and the gas density.

2.7 SEM Imaging

In order to study the change in morphology of the coal particles as a result of combustion, Scanning Electron Microscopy (SEM) was used. The SEM images of the coal particles collected after combustion were compared to those obtained before combustion in order to reveal any structural changes in the coal particle as a result of combustion. SEM analysis was carried out on the Jeol 6060 LV SEM in the Frederick Seitz Materials Research Laboratory Central Facilities in the University of Illinois at Urbana-Champaign. The Jeol 6060 LV SEM was typically operated at high vacuum condition (10^{-5}Torr) with the electron beam voltages varying from a few hundred volts up to 30 kV. The Jeol 6060 LV SEM was also specially equipped with a differentially pumped variable pressure system for operations up to 20 Torr in the specimen chamber for imaging of uncoated non-conductive samples and samples not compatible with high vacuum. The Jeol 6060 LV SEM is capable of magnifications ranging from 5x to 200,000x. The cut-section view showing the various parts of the Jeol 6060 LV SEM is shown in Figure 2.8.

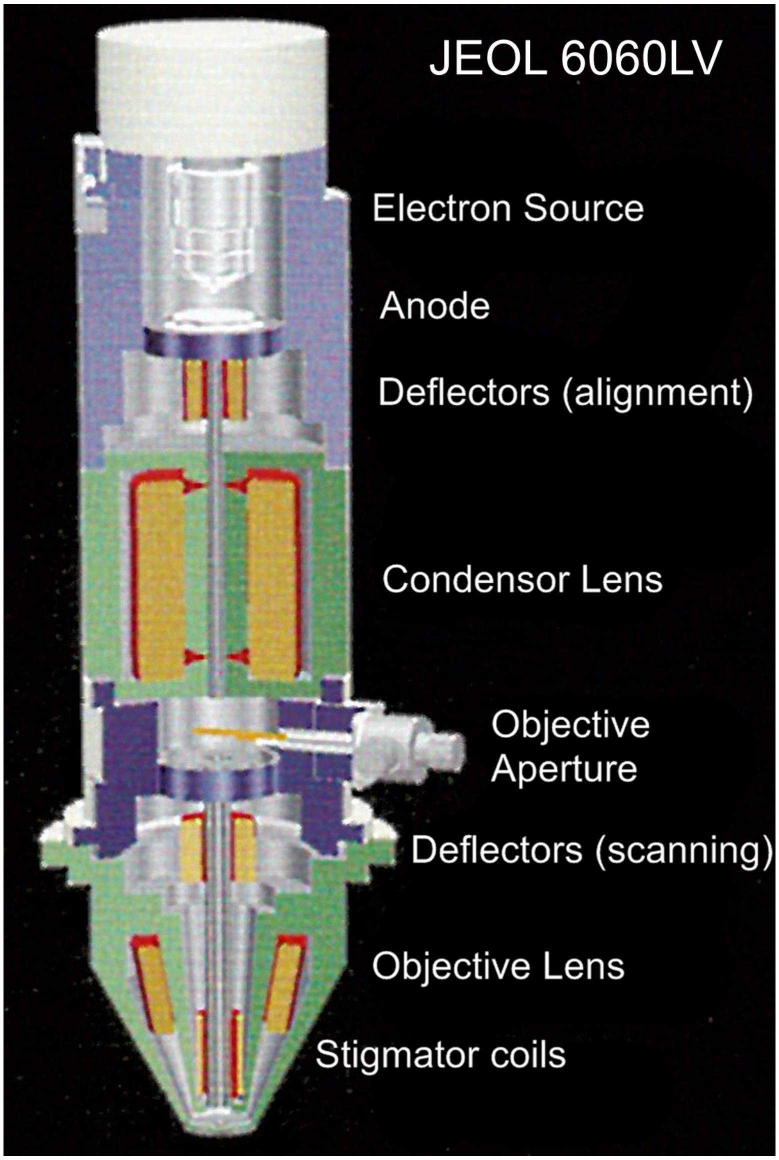

Figure 2.8: Cut-section view of the Jeol 6060 LV SEM

If the instrument was operated above an electron beam voltage of 10 kV, significant charging of the samples led to deteriorating image quality for higher magnifications. This happened because coal particles were electrically non-conductive. In order to prevent the samples from charging, the instrument had to be operated either in the Low Vacuum (LV) mode or the sample had to be prepared before observation. The sample was prepared by applying a thin coating of around 10 nm of Gold-Palladium alloy (Au-Pd) using a sputtering device. This Au-Pd coating makes the sample more conductive and thereby permits higher electron beam voltages for better resolution at high magnifications.

Once the sample was coated, it was mounted on the sample holder and placed onto the Jeol 6060 LV for analysis. A working distance of 10 mm was found to be suitable for the range of magnification used in our analysis. In order to take quality SEM images for analysis, the following steps were followed:

- **Working Distance:** The working distance was precisely adjusted to 10 mm by moving the stage holding the sample using the Z adjustment knob until a clear focused image was obtained on the screen.
- **Gun Alignment:** The filament heating current was set so as to operate very near to the saturation regime, i.e, region where increase in filament current will not increase the brightness of the image any further. In case, if the brightness of image was found to decrease with increasing filament current then a gun alignment procedure had to be performed. This was done by systematically adjusting the X, Y-Shift and the X, Y-Tilt parameters manually. These parameters controlled the position and the tilt angle of the electron beam respectively as it passed through the alignment coils. This adjustment was performed until the gun was made to operate back again in the saturation regime.
- **Objective aperture alignment:** If the image was found to move on the screen while manually focusing, the objective aperture needs to be aligned. The X and Y fine controls knobs on the SEM that control the objective aperture position were adjusted suitably until the motion of the image on the screen while focusing was reduced substantially.
- **Astigmatism Correction:** If the image was found to be focused asymmetrically or with stretching or streaks, then astigmatism correction had to be performed. The X and Y stigmator coils were adjusted manually until the distortion of the image on the screen was minimized.

After the preliminary adjustments were performed, the sample was then ready for observation. High quality SEM images were acquired using appropriate beam voltages and magnification as required for analysis. The images were tagged using the “Tag” function with the operating conditions i.e, beam voltage, magnification, working distance etc., for future reference. The brightness and contrast were appropriately adjusted in order to get an image with well-defined features in shades of grey avoiding regions of saturation. The salient dimensions could also be measured on the image using the “Measure” function. The “Scan 1” and “Scan 2” modes were suitable for quick imaging needs like alignment, locating the sample etc. The actually SEM images used for analysis were taken using either the “Scan 4” or “Photo mode” at the maximum possible of resolution of 1280 x 960 pixels. This mode provided the best possible image quality by decreasing the noise.

CHAPTER 3

RESULTS & DISCUSSION

3.1 Effect of Combustion on Loose Density

The effect of combustion on the morphology and macroscopic properties of coal particles was analyzed by comparing the loose density of the coal particles before and after combustion process as they pass through the flame sheet. The details of the loose density analysis performed on the coal particles are presented in Table 3.1.

Sample No.	Sieve Number	Mean Diameter D_M (μm)	Loose Density before combustion (g/cc)	Loose Density after combustion (g/cc)	% Change in Loose Density (%)
1	18 - 20	927	0.733	0.732	-0.096
2	20 - 25	782	0.735	0.733	-0.231
3	25 - 30	655	0.738	0.736	-0.277
4	30 - 35	550	0.743	0.741	-0.292
5	35 - 40	461	0.750	0.747	-0.408
6	40 - 45	388	0.755	0.751	-0.476
7	45 - 50	326	0.763	0.758	-0.590
8	50 - 60	274	0.772	0.767	-0.600
9	60 - 70	231	0.775	0.771	-0.531
10	70 - 80	195	0.781	0.776	-0.626
11	< 80	178	0.784	0.779	-0.750

Table 3.1: Loose density analysis of coal samples before and after combustion.

From this data, it is evident that the loose density of coal particles was dependent on the particle size to some extent. The loose density of the coal particles was found to increase progressively with decreasing particle size. The coal sample with a relatively larger mean diameter of 927 μm had the minimum loose density, 0.733 g/cm^3 whereas fine coal dust with mean diameter of less than 178 μm had the maximum loose density, 0.784 g/cm^3. This corresponded to an increase of 7.08 % in terms of loose density. This increase in loose density of coal particles with progressively decreasing particle size can be explained in terms of porosity or void fraction. Void fraction or Porosity is a measure of the void spaces in a sample and is defined as the ratio of the total volume of voids to the total volume occupied by the sample.

$$\varphi = \frac{Total\ volume\ of\ void\ spaces}{Bulk\ Volume} = \frac{V_v}{V_t} \tag{3.1}$$

$$\varphi = 1 - \frac{Loose\ density}{Particle\ density} \tag{3.2}$$

For coarser particles, in an un-compacted sample like the one used for loose density measurements, the particles tend to form bigger voids within the sample that led to increase in the void fraction. This increase in void fraction due to larger particle size reflects as a direct decrease in the loose density of coarser coal samples. On the other hand, finer particles tend to form numerous voids that are much smaller and thereby result in an overall decreased void fraction. Thus finer coal samples had a slightly higher loose density owing to the decreased void fraction when compared to coarser coal samples.

Similar loose density analysis was also performed on the ash particles that were collected after the coal samples were subjected to combustion by entraining them into a methane jet flame. From Table 3.1, it can be clearly seen that there was no significant change in the loose density of coal particles as a result of combustion. This is attributed to the small residence time on the order of 0.01 s for the coal particles inside the flame front in our experiments. This is about an order of magnitude less than the time required for complete devolatilization of pulverized coal as reported by I.W. Smith [34]. In essence, the combustion process hardly modified the macrostructure of these particles. Hence there was no considerable change in the loose density of the coal particles after combustion. But it is also evident that, the loose density of finer coal samples was affected to a relatively large extent due to the combustion process when compared to those of coarser coal samples. The loose density of the coal sample with a mean diameter of 927 μm changed by hardly 0.10 % to 0.732 g/cm^3 as a result of the combustion process. On the other hand the loose density of the fine coal dust with mean diameter of less than 178 μm changed by almost 0.75 % to 0.779 g/cm^3 after combustion. The variation of loose density of the coal particles before and after the combustion process for different samples based on mean diameter is presented in Figure 3.1. It is to be noted that the variation in the loose density of the coal particles as a function of the mean particle diameter before and after combustion can be closely approximated by a second order polynomial fit. The loose density of the coal particles after combustion was found to be hardly dependent on the nature of the flame i.e, diffusion flame, premixed flame etc. This is again due to the fact that the residence time in all these cases were so small (~ 0.01 s) that the type of combustion process hardly mattered in modifying the macrostructure of the coal samples.

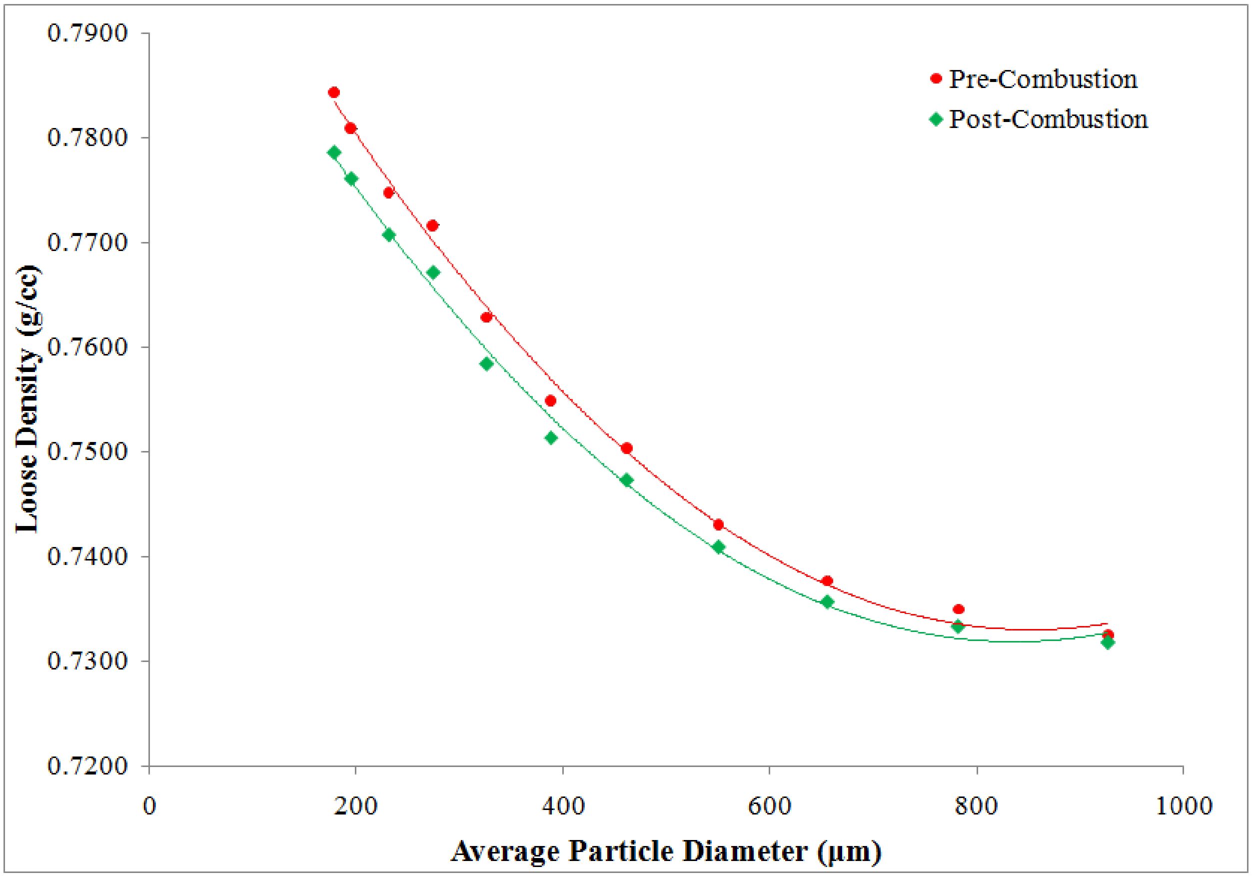

Figure 3.1: Comparison of loose density of coal particles before and after combustion as a function of particle diameter.

3.2 Effect of Particle Size on Entrainment Rate

To study the effect of particle size on entrainment rate, the hopper arrangement was filled with a coal sample of known mean diameter and the flow rate of air was increased in steps by using Omega FL-3840 G rotameter. The entrainment rate of the coal particles was calculated by collecting the entrained coal particles on a collection tray fitted on the hopper arrangement over a fixed period of time i.e., 20 s. This was then weighed on an Ohaus JR 120 Precision Standard

Electronic Balance to evaluate the entrainment rate. Each set of experiments was repeated five times to ensure consistency. The same procedure was repeated for all the 11 different samples that were earlier prepared based on particle size.

The upstream pressure regulator which was connected to the Omega FL-3840 G rotameter that supplied air for the entrainment process was maintained at a fixed gauge pressure of 50 psi. The entrainment experiments were then carried out at ambient temperature of 75° F. For each of the coal samples, the air flow rate was carefully adjusted until a significant amount of coal particles got entrained in the flow and were collected in the collection pan. From that point on, the flow rate of air was increased in steps to study the total entrainment rate of coal particles as a function of flow rate of air.

In order to calculate the actual volumetric flow rate of air under standard conditions of pressure and temperature using the rotameter, certain correction factors were to be evaluated. These correction factors accounted for the operating conditions of the rotameter (50 psig and 75°F) which were different from its original calibrated conditions (14.7 psia and 70°F). The pressure correction factor (PCF) and the temperature correction factor (TCF) were computed using the following equations [35]:

$$PCF = \sqrt{\frac{P\ (psia)}{P_0\ (psia)}} = \sqrt{\frac{P_g + 14.7}{14.7}} \tag{3.3}$$

$$TCF = \sqrt{\frac{T_0\ (°\mathrm{R})}{T\ (°\mathrm{R})}} = \sqrt{\frac{530}{T + 460}} \tag{3.4}$$

The corrected volumetric flow rate of air under standard conditions of pressure and temperature was then computed based on the correlation charts provided by the manufacturer and the evaluated correction factors as follows:

$$Q' = Q_0 * PCF * TCF \tag{3.5}$$

Further by evaluating the density of air at the standards conditions, the volumetric flow rate of air was converted into an equivalent mass flow rate of air.

The entrainment rate of coal particles (grams per minute) as function of the air mass flow rate (grams per minute) for various sizes of coal particles ranging from sieve size: 18-20 to sieve size: < 80 is presented in Figures 3.2 - 3.5. From the Figures, it is evident that the particle entrainment rate was mainly dependent on the flow rate and the size of coal particles.

In general, as the flow rate of air was increased, the particle entrainment rate also increased due to the increased Venturi effect. For all the cases considered in our analysis, the entrainment rate followed an almost linearly increasing trend. This is indicated in the graphs by the near perfect correlation with a linear fit. The error bars in the graphs correspond to one unit of standard deviation. The experimental results on particle entrainment rate were found to be fairly in good agreement with similar studies carried out by Xie et al. [21], in terms of the observed trend: linearly increasing entrainment rate with respect to air flow rate.

For the ease of comparison, the entrainment rate for coarse (Sieve size: 18-20), mid-size (Sieve size: 40-45) and fine coal particles (Sieve size: < 80) is presented in Figure 3.6. It can be seen that the minimum flow rate at which significant entrainment occurs decreased considerably with decreasing particle size. For coarser particles, minimal entrainment happened for flow rates less than 21 g/min, while for finer particles significant entrainment happened even at a very low flow rate of around 6 g/min. For mid-size coal particles, the minimum entrainment flow rate had a nominal value of around 10 g/min.

The pressure drop developed as result of the Venturi effect was used to overcome partly the frictional losses due to the interaction of the coal particles with holes on the circumference of the tube with and to carry the sheer inertia of the coal particles into the flow. It is evident that for particles with a larger mean diameter, due to the increased frictional and inertia effects, a larger pressure drop was required to cause significant entrainment of particles onto the flow. This large pressure drop requirement resulted in an increase in the minimum flow rate of air required for significant entrainment of coarser particles. However it is to be noted that beyond this point of minimum flow rate for significant entrainment, the entrainment rate for all the cases increased linearly. The slopes of these linear dependencies increased with decreasing particle size due to significant decrease in friction and inertia effects. As a result of this, smaller particles tend to get entrained in the flow much more easily when compared to larger particles for the same flow conditions.

The mass loading or the particle loading for these flows as function of the particle diameter is presented in Figure 3.7. The error bars on the graph represent one unit of standard deviation. Based on the actual entrainment data collected during the experiments, mass loading factor was computed as:

$$ML = \frac{Mass\ of\ paricle\ phase}{Mass\ of\ gas\ phase} = \frac{m_p}{m_g} \tag{3.6}$$

It can be seen that the mass loading as a function particle diameter can be fitted closely to a second order polynomial. Since the mass loading increased significantly with decreasing particle diameter, it is evident that global turbulent modifications can be easily induced for flows entraining finer coal particles than those entraining coarser coal particles.

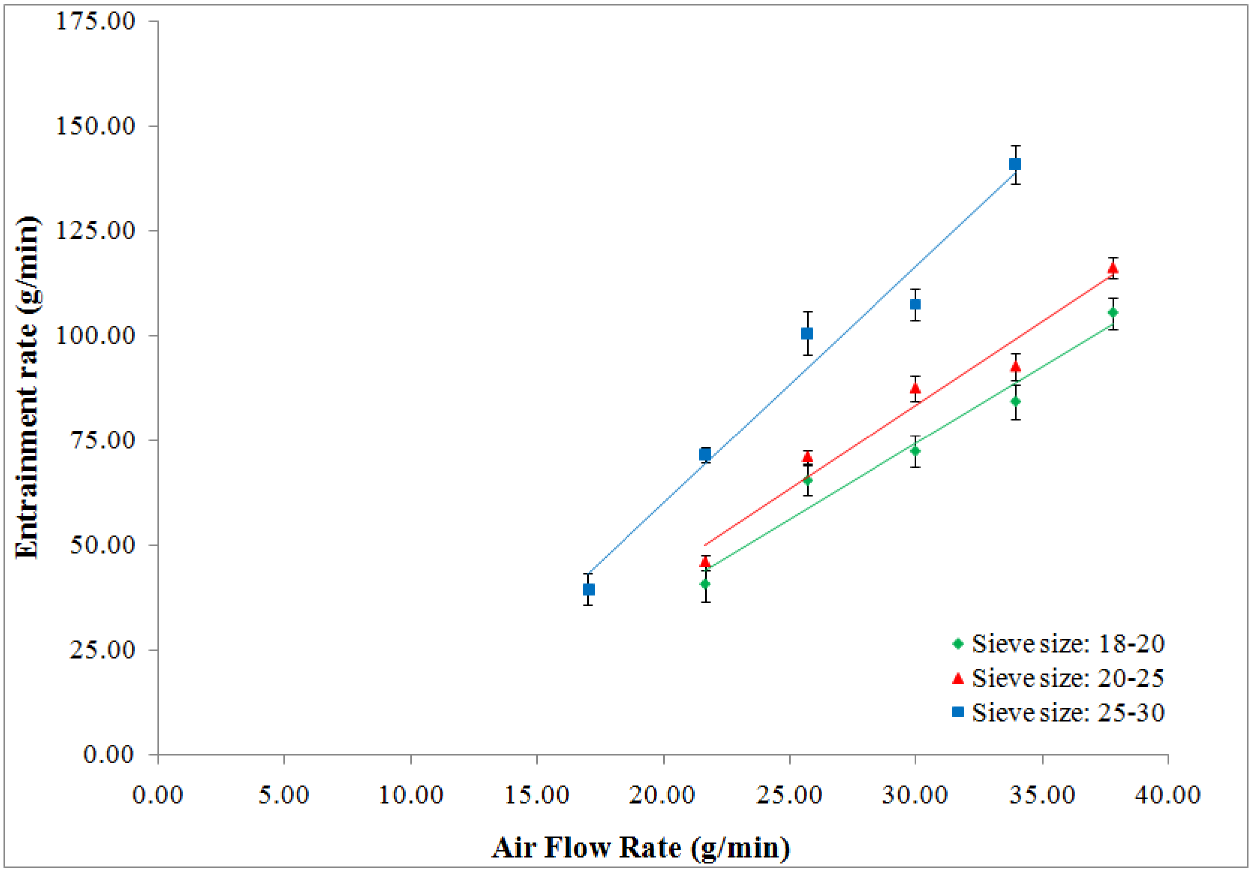

Figure 3.2: Coal particle entrainment rate as a function of air flow rate for different particle sizes (a) Sieve size: 18-20 (b) Sieve size: 20-25 (c) Sieve size: 25-30.

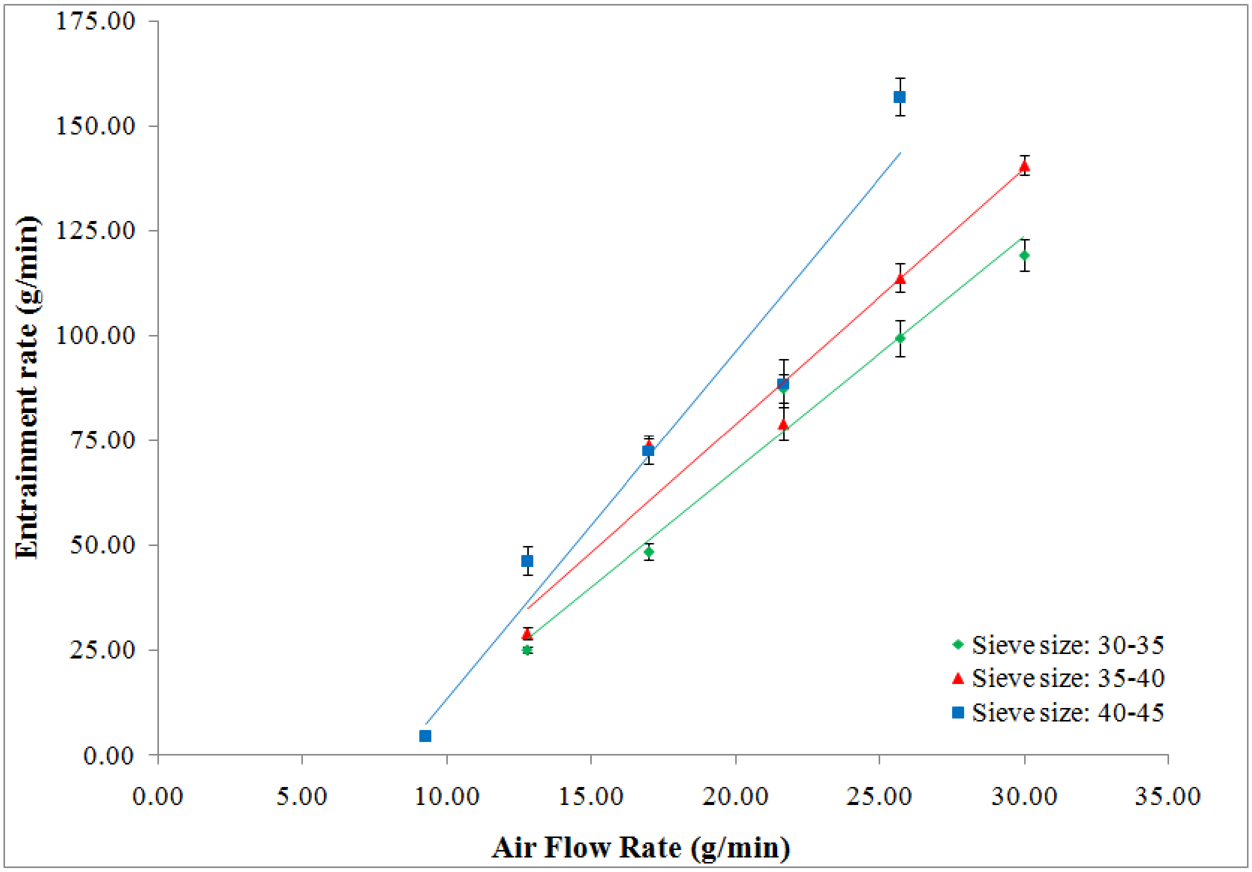

Figure 3.3: Coal particle entrainment rate as a function of air flow rate for different particle sizes (a) Sieve size: 30-35 (b) Sieve size: 35-40 (c) Sieve size: 40-45.

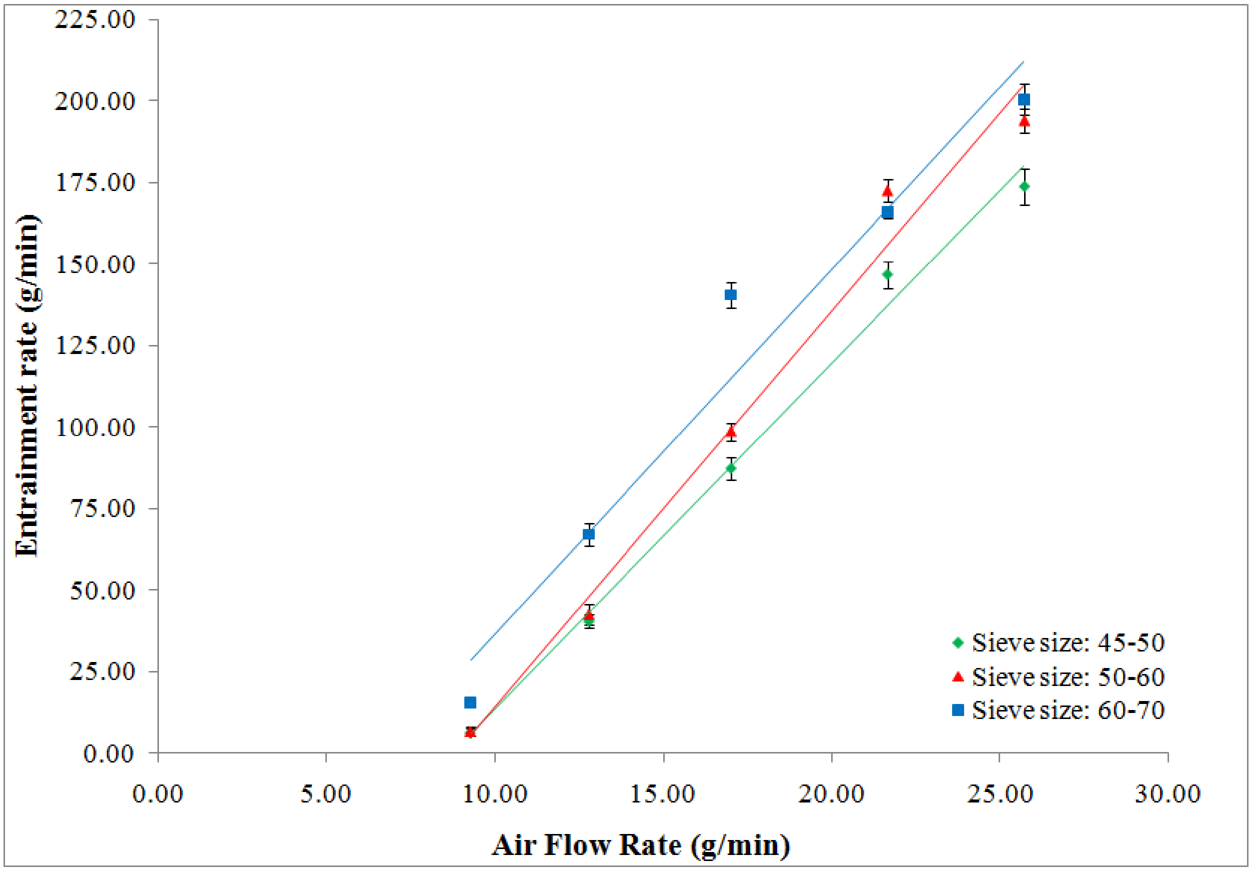

Figure 3.4: Coal particle entrainment rate as a function of air flow rate for different particle sizes (a) Sieve size: 45-50 (b) Sieve size: 50-60 (c) Sieve size: 60-70.

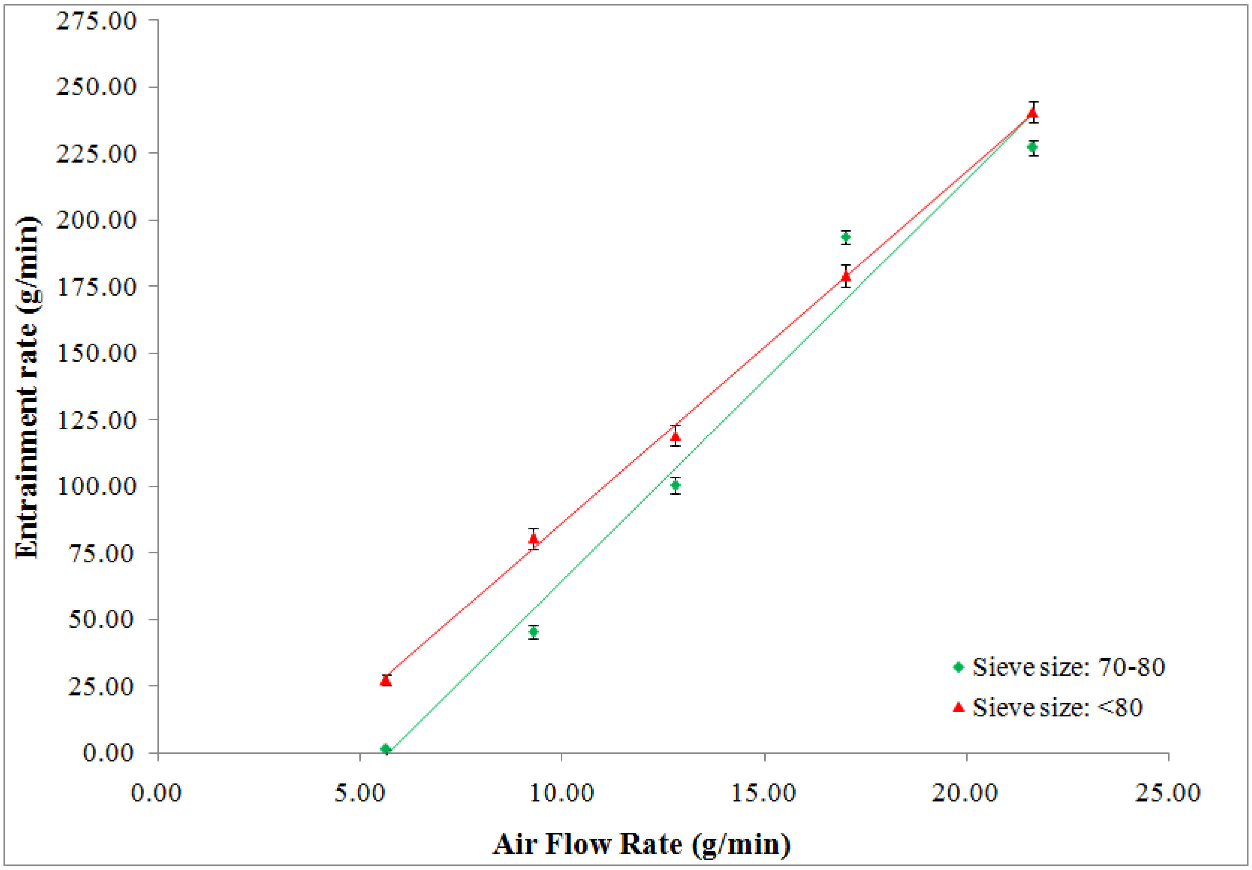

Figure 3.5: Coal particle entrainment rate as a function of air flow rate for different particle sizes (a) Sieve size: 70-80 (b) Sieve size: < 80.

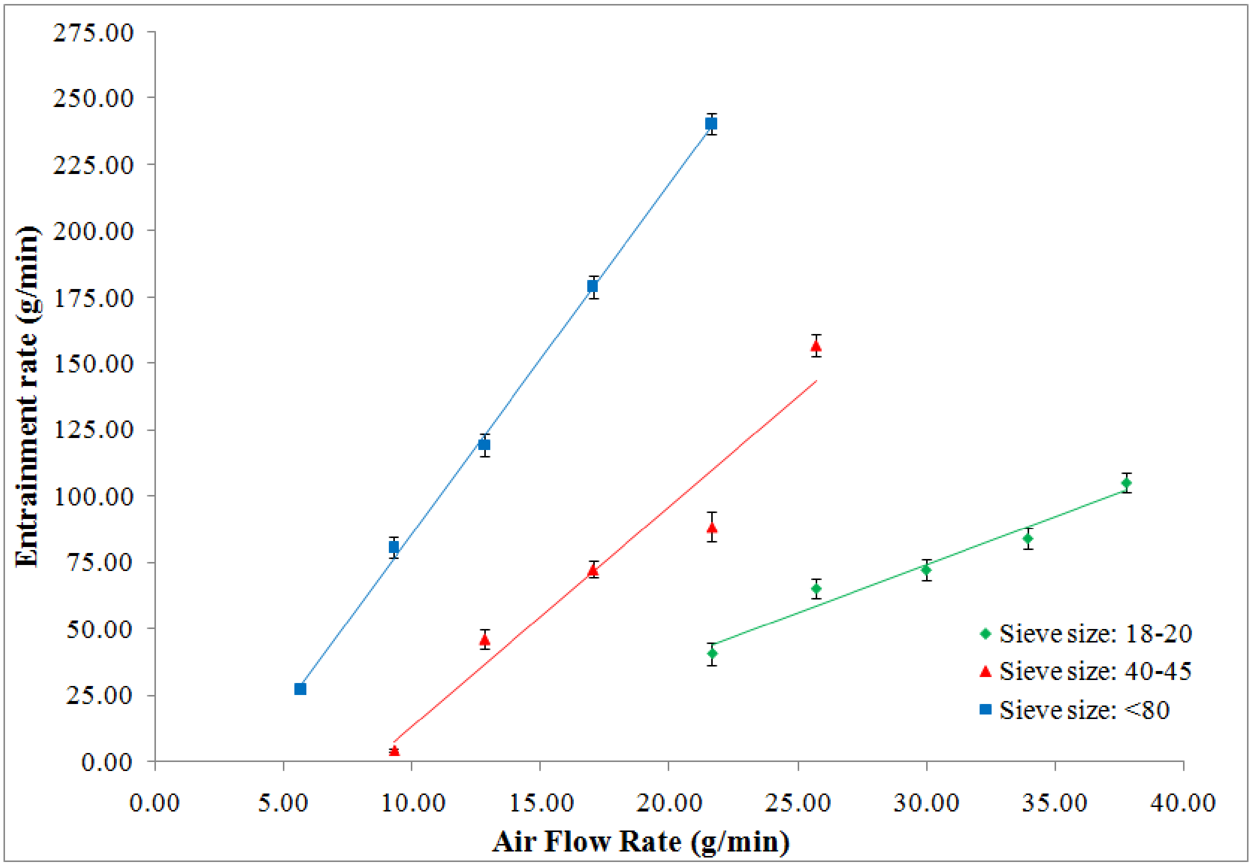

Figure 3.6: Comparison of coal particle entrainment rate as a function of air flow rate for particle sizes (a) Sieve size: 18-20 (b) Sieve size: 40-45 (c) Sieve size: < 80.

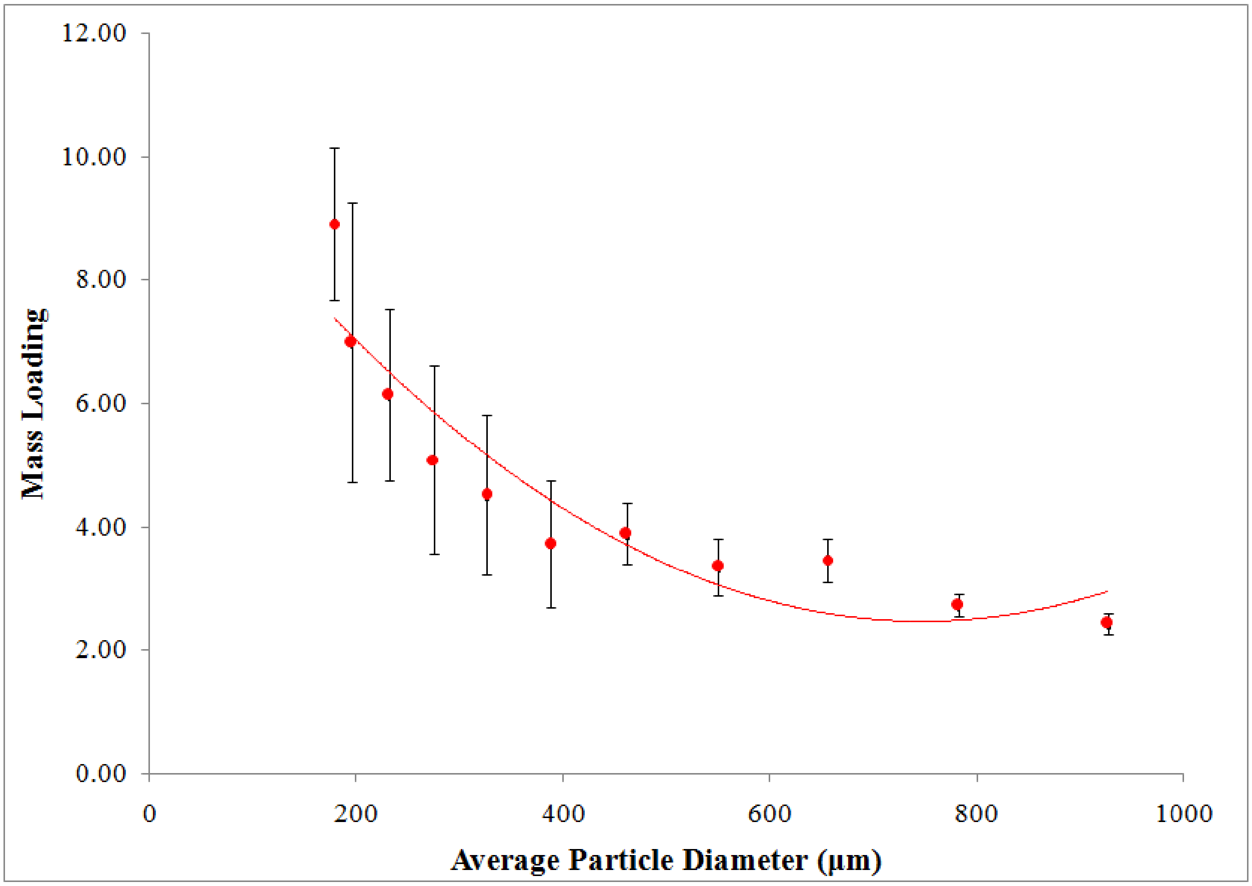

Figure 3.7: Mass loading as a function of particle diameter based on (a) actual entrainment data (b) slope of the linear fit.

3.3 Particle Streak Velocimetry

In order to compute the velocity of the coal particles in relation to the flow field, Particle Streak Velocimetry (PSV) analysis was carried out. To obtain velocity information, a series of high-resolution images captured using the Nikon D5100 camera with a relatively long exposure time was analyzed using ImageJ software. The exposure time of the camera was suitably adjusted so that the moving particles in each frame appeared as streaks rather than individual particles. Using these streaklines, Particle Streak Velocimetry analysis was carried out to evaluate the velocity of the particles in relation to the flow field. The velocity measurements were taken at a plane coincident with the center of the tube.

The typical steps involved in image processing using ImageJ software for a selected image to evaluate the velocity of the particles using the method of Particle Streak Velocimetry is shown in Figure 3.8. The raw image as taken by the Nikon D5100 before any processing, the converted grey scale image with pixel intensities ranging from 0 to 255, and the final processed image after inversion using binary transformation is presented in Figure 3.8 (a), (b) and (c) respectively.

By measuring the length of each streakline which now corresponded to the distance travelled by the particle in the selected exposure time, velocity information can easily be extracted from the images. For a typical exposure rate of 1/800 s, an uncertainty of 1 pixel in measuring the length of a streakline corresponded to an error of 0.01 m/s in terms of velocity. Zooming in on the streaklines closely for accurate length measurements coupled with ImageJ's exceptional processing abilities made this method, a fairly adequate and reliable velocity measurement technique.

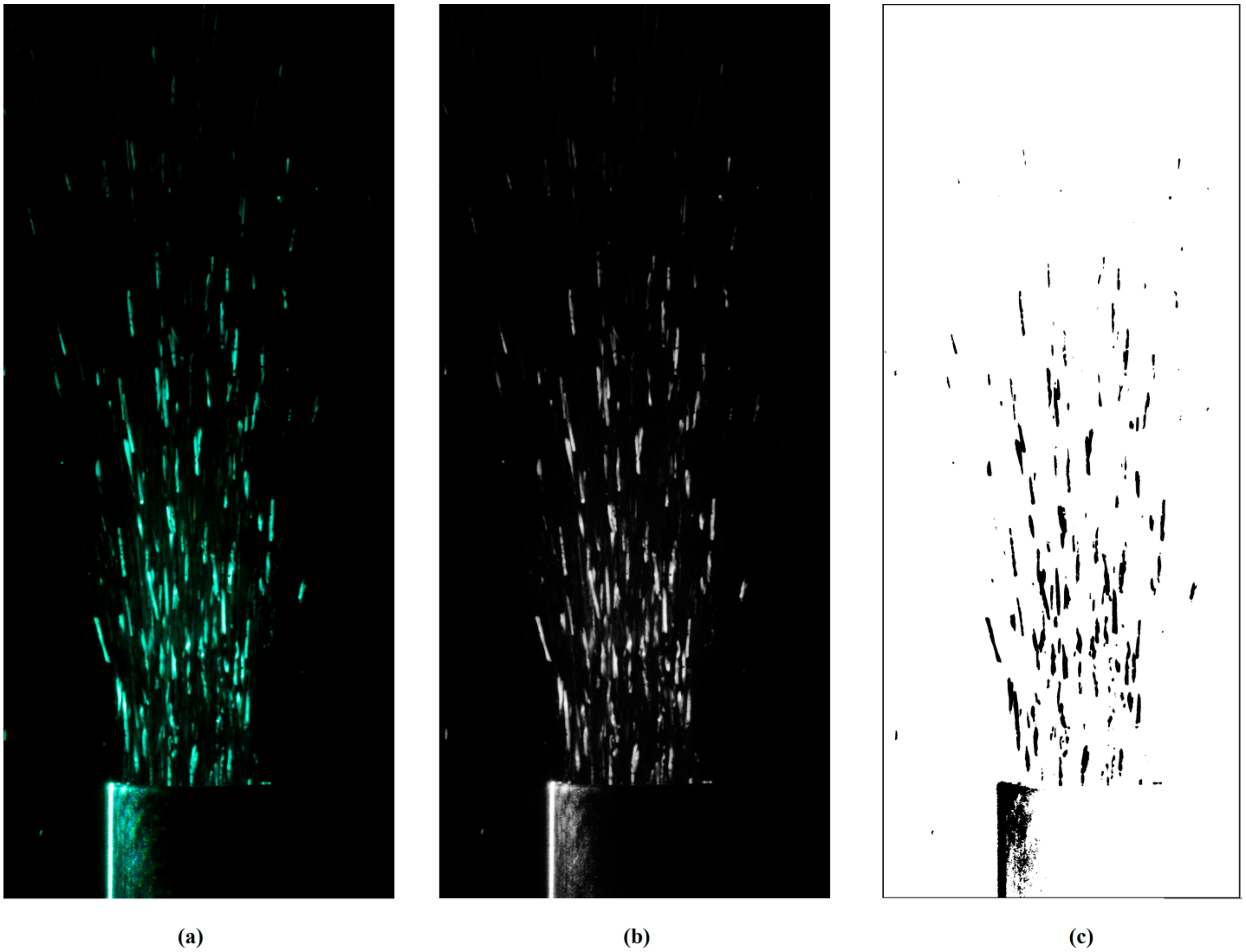

Figure 3.8: Typical steps involved in image processing using Image J for PSV. (a) Raw image captured by Nikon D5100 (b) Corresponding grey scale image (c) Inverted image after Binary transformation displaying streaks for PSV analysis.

In order to provide an overall picture of the PSV analysis performed, two important parameters namely the particle stoppage time τ_s and the Stokes number [19] associated with the flow were calculated based on Equations 3.7 and 3.8 respectively. The particle density ρ_p and the mean particle diameter d_p were taken based on the values tabulated earlier in Table 3.1. The inner diameter of the tube was considered to be the characteristic length scale L in order to evaluate the Stokes number.

$$\tau_p = \frac{\rho_p d_p^2}{18\mu} \tag{3.7}$$

$$Stk = \frac{\tau_p U}{L} \tag{3.8}$$

In our case, the mean flow velocity U was computed to be 2.5 m/s based on the flow rate recorded by the rotameter, the cross sectional area of the tube and the gas density. The stoppage time and the Stokes number for various coal samples are presented as function of the mean particle diameter in Figure 3.9 and 3.10 respectively.

From Figure 3.10, it is clear that for all coal samples, the Stokes number is sufficiently large (namely $Stk \gg 1$), hence the particle velocity differs significantly from the fluid velocity. This resulted in the particles diverting rather substantially from the fluid stream path and thereby leading to significant momentum transfer from the particles to the fluid. Thereby, the inertia effects of the particles become more prevalent and exert a significant influence on the background fluid. This finding was supported by the particle velocities measured using Particle Streak Velocimetry technique. Figure 3.11 shows the variation of particle velocity as function of Stokes number for a mean flow velocity of 2.5 m/s. The error bars shown on the graphs represent one unit of standard deviation. It can be seen that even the smallest of the coal particle travelled at a sufficiently low velocity when compared to the velocity of the surrounding gas that can lead to significant momentum transfer from the particles to the fluid.

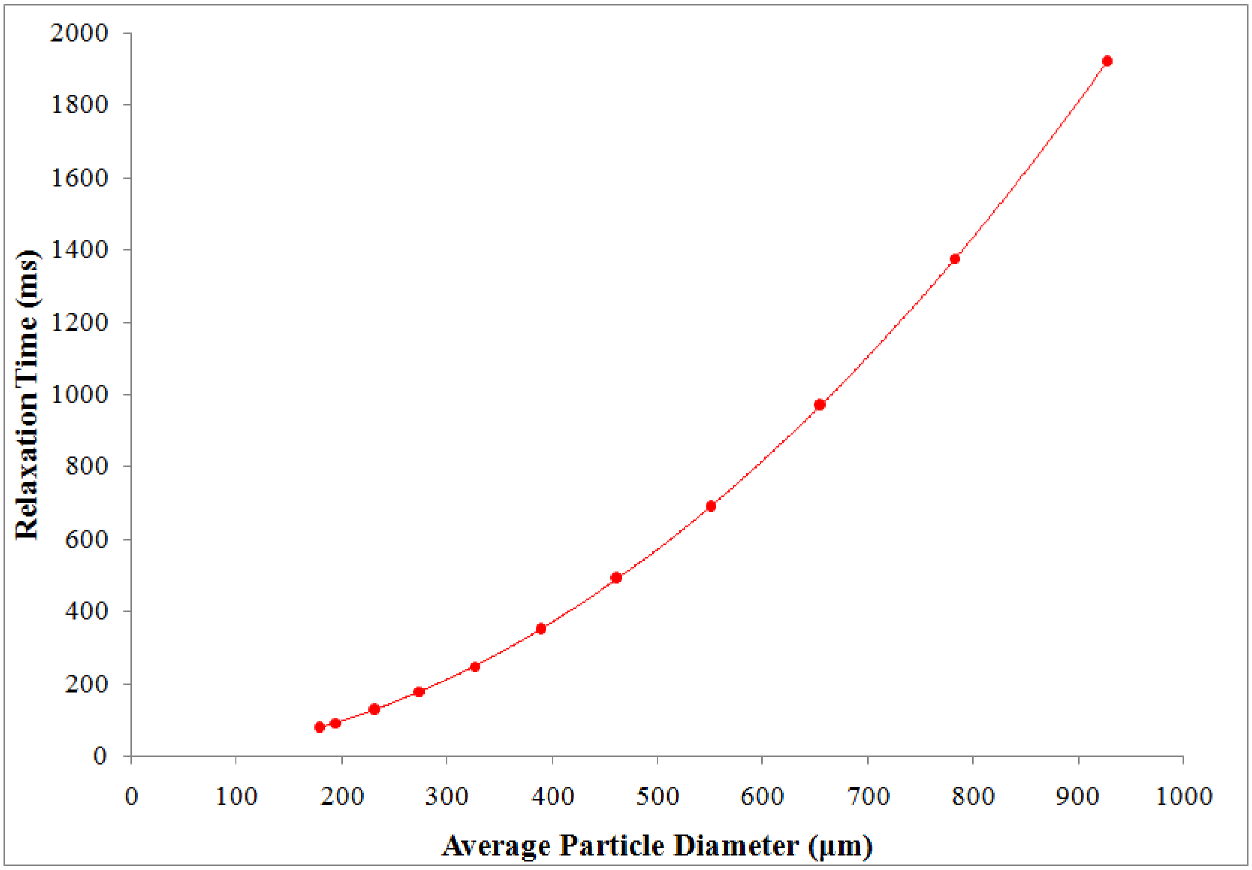

Figure 3.9: Relaxation time as a function of particle diameter.

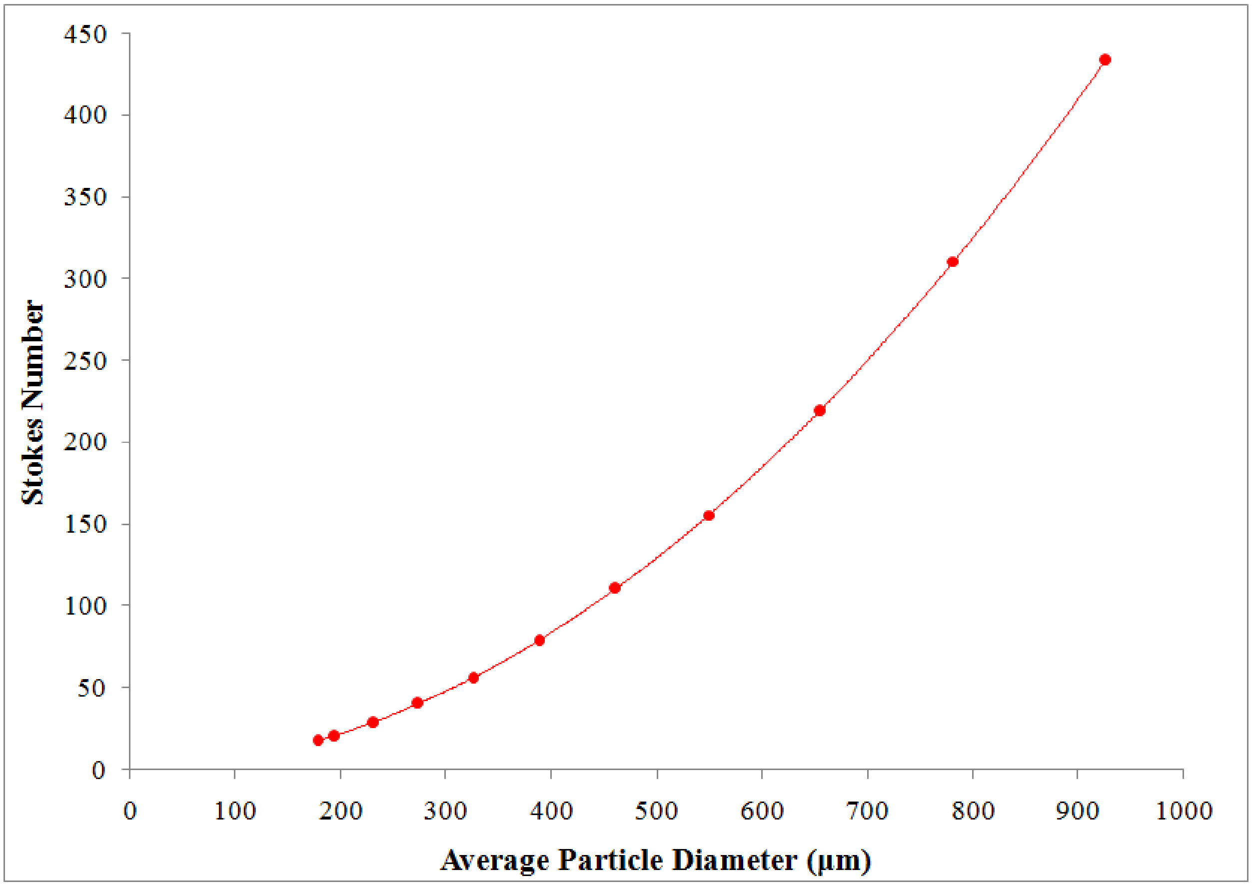

Figure 3.10: Stokes number as a function of particle diameter for a mean flow velocity of 2.5 m/s.

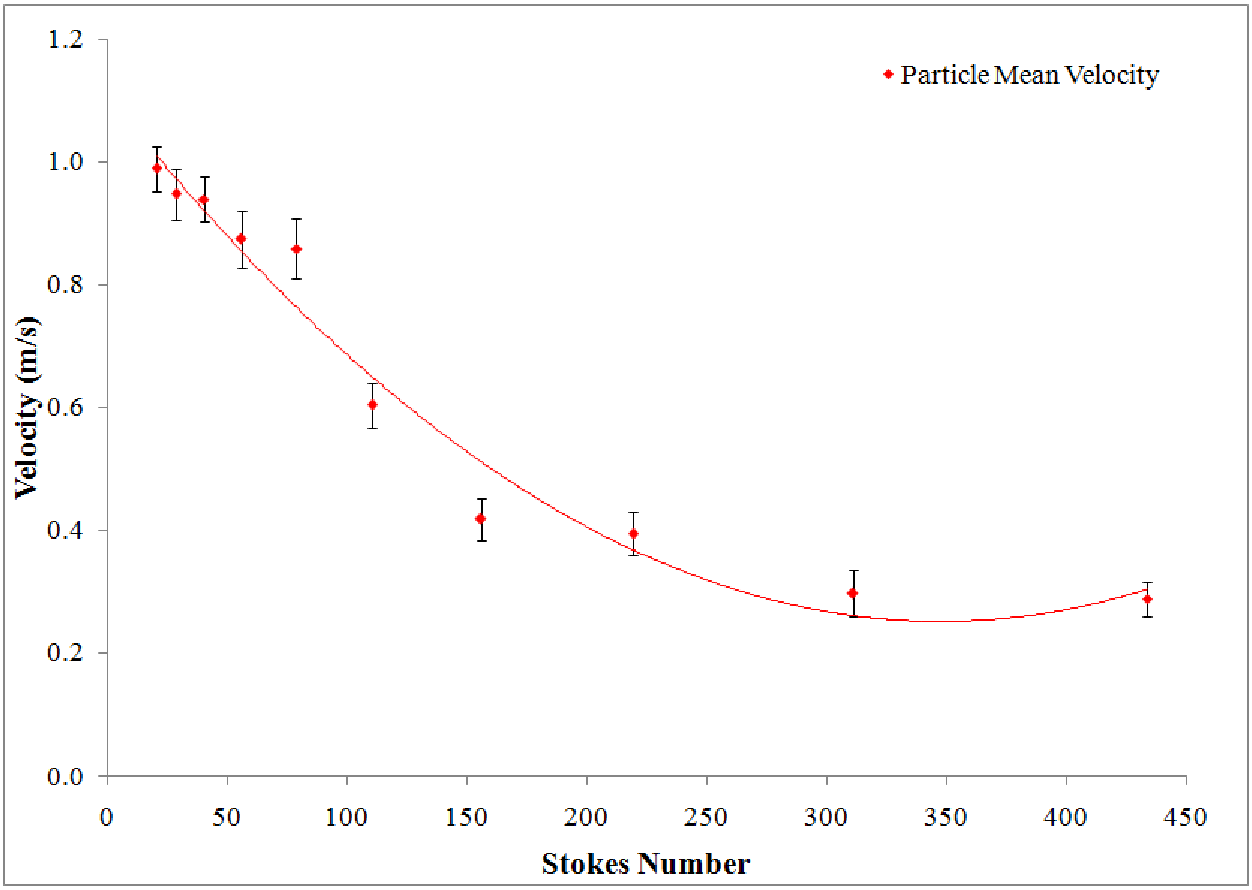

Figure 3.11: Average Particle velocity measured by PSV as a function of Stokes number for a mean flow velocity of 2.5 m/s.

3.4 Combustion Phenomenology

In order to establish combustion phenomenology of the coal-laden jets, high-resolution images taken using the Nikon D5100 and high-speed videos taken using the Phantom v.7.0 were analyzed. This was done so as to reveal the mode of interaction of the entrained coal particles with the flame. High-resolution images showing the non-diluted CH_4 diffusion flame, the weakly diluted CH_4 diffusion flame ($CH_4:N_2 \sim 1:1$ by mass) and the strongly diluted CH_4 diffusion flame ($CH_4:N_2 \sim 1:2.5$ by mass) are presented in Figure 3.12 (a), (b) and (c) respectively. It can be clearly seen that the pure diffusion flame was strongly luminescent due to soot formation. Diluting the flame with nitrogen decreased soot formation. By carefully adjusting the nitrogen flow rate, soot formation could be completely eliminated which resulted in achemi-luminescent blue diffusion, where the interaction of the entrained coal particles with the flame was studied.

High-resolution images from the non-diluted, the weakly diluted ($CH_4:N_2 \sim 1:1$ by mass) and the strongly diluted ($CH_4:N_2 \sim 1:2.5$ by mass) CH_4 diffusion flames are presented in Figure 3.13 (a), (b) and (c) respectively. Once flow is laden with coal particles due to entrainment caused by Venturi effect, the luminosity of the flame increased. This was because the coal particles started to incandesce as they crossed the flame front. The coal particles are seen as brightly incandescent streaks once they cross the flame front as shown in Figure 3.13.

However, since the coal particles did not incandesce until they were close enough to the flame front, Figure 3.13 does not reveal any information on how coal particles interact with the flame front as soon as they get entrained in the flow. To make the coal particles visible as they approached the flame front, an Argon Ion laser sheet was utilized as described in section 2.5. The coal particles that were on the plane of the laser sheet scattered light thereby making them visible as shown in the images presented in Figures 3.14 and 3.15. The laser sheet shows the trajectory of the coal particles right from the tip of the burner to the point where they start to incandesce as they cross the flame front. It is clear from Figure 3.14, that the trajectory of the coal particles is hardly affected by the presence of the flame front. The coal particles appear to shoot right through the flame front without any change in their initial trajectory as they are entrained in the flow. And in this process, once they approach the flame front, the temperature of the particle increases and they become luminescent. The coal particles start to burn and continue to get sintered as they traverse the flame front as shown in Figure 3.15.

Successive frames from one of the high-speed videos captured using the Phantom v.7.0 is shown in Figure 3.16. These high-speed snapshots again clearly show that the coal particles shoot right through the flame front and in the process they start to burn thereby becoming incandescent. Using a Fotodiox Canon EOS Macro Extension Tube Set Kit for Extreme Close-up, high-speed videos focusing on the region where they coal particles interact with the flame front was captured. Successive frames from one such video is presented in Figure 3.17. The trajectory of the coal particles before and after the flame front can be clearly seen in these images. It is evident from Figure 3.17, that the trajectory of the coal particles was unaffected by the presence of the flame front as the particles simply appear to traverse across the flame front. Also the particles, after crossing the flame front are found to be more luminescent than before, which implied that the coal particles started to sinter as a result of interacting with the flame front that resulted in increased luminosity and they continued to burn as they cross the flame front.

A high-resolution image showing the acceleration of the coal particles as they approach the flame front is presented in Figure 3.18. It can be seen that small streaklines which correspond to individual coal particles become longer as they near the flame front. This means that the particles in the given exposure time of the camera happen to travel a longer distance as they approach the flame front. This implied that the coal particles happen to experience a significant increase in velocity as they approach the flame front i.e., the coal particles experience acceleration. Successive frames from the high-speed video depicting the acceleration of the coal particle approaching the normal flame front and the side of the flame are presented in Figures 3.19 and 3.20 respectively. The red circle marked on the image tracks the streakline of an individual coal particle across different frames i.e., different instances of time. It can be clearly seen that the streamline get elongated in the successive frames owing to the increased distance travelled by the particle as it get accelerated towards the flame front. This acceleration of the coal particles as they approach the flame front can be attributed to the increase in the flow speed of coal-laden gas as it moves towards the flame. The gases get heated up as they approach flame front which results in a decrease in the density of the gases. Because of the decrease in density, the gas has to accelerate towards the flame front in order to maintain a constant mass flow rate (conservation of mass). This acceleration in the carrier fluid is also partly transferred onto the entrained coal particles which also as result accelerate towards the flame front. Figure 3.20 shows an individual coal particle accelerating and luminescing as it interact with side of the flame.

High-resolution images of the top view of the flame as the coal particles approaching and crossing the flame front is presented in Figures 3.21 and 3.22 respectively. From Figure 3.21, it is clear that the flame front gets punctured as result of the entrained coal particles shooting through the flame. The reason for this extinction is currently unclear. It is however reasonable to assume that because of the small residence time, solid fuel combustion is not completed and the particles behave as almost inert, so extinction can be attributed to a combination of increased flame strain and heat losses to the inert particles. Once the coal particles cross the flame zone, they accelerate and are seen as bright luminescent streaks as shown in Figures 3.22.


(a) (b) (c)

Figure 3.12: (a) Non-diluted CH_4 diffusion flame (b) Weakly diluted CH_4 diffusion flame(c) Strongly diluted CH_4 diffusion flame strongly diluted with N_2. No laser sheet present.

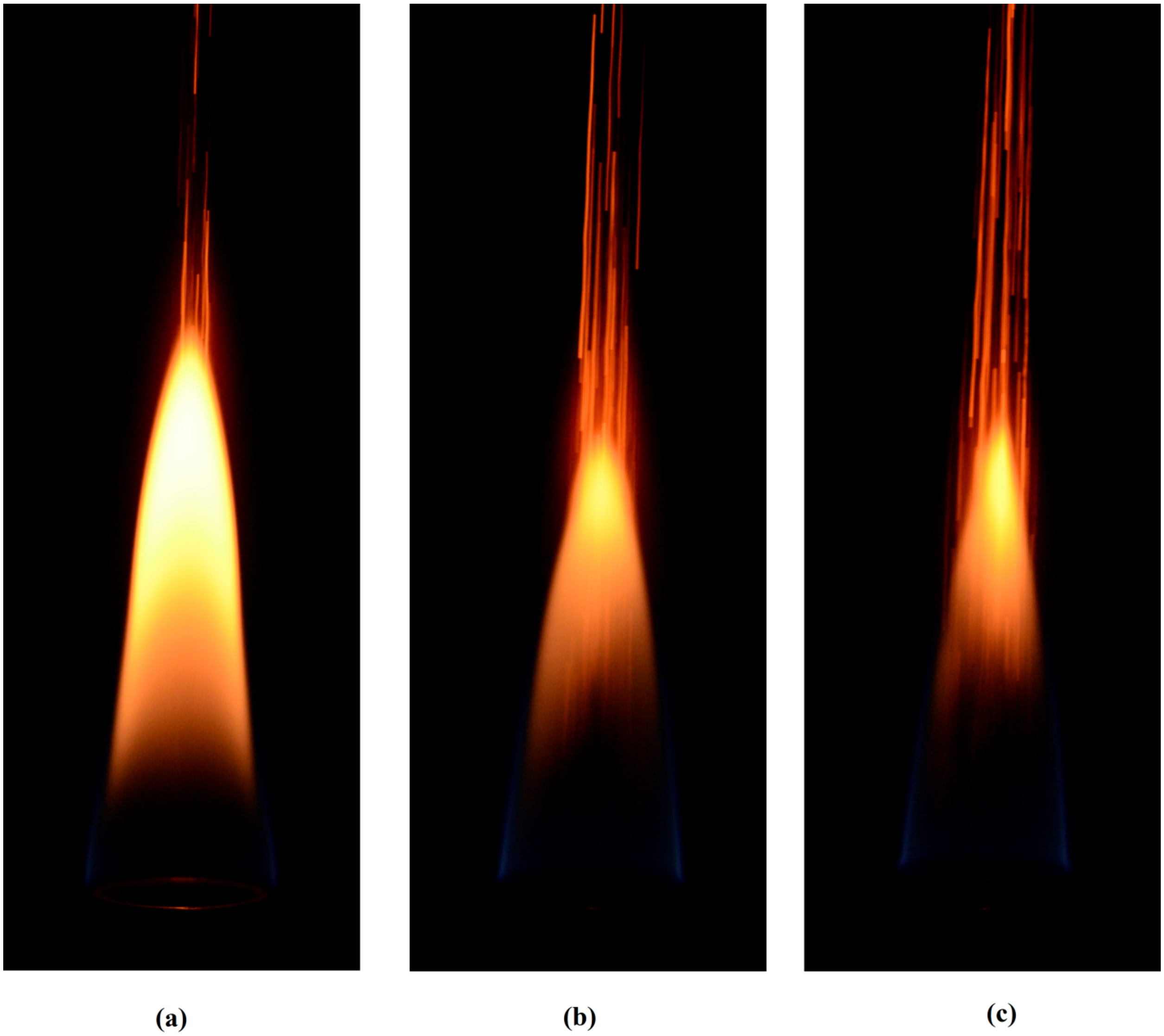

Figure 3.13: Coal particles shooting through (a) Non-diluted CH_4 diffusion flame (b) Weakly diluted CH_4 diffusion flame(c) Strongly diluted CH_4 diffusion flame. No laser sheet present.

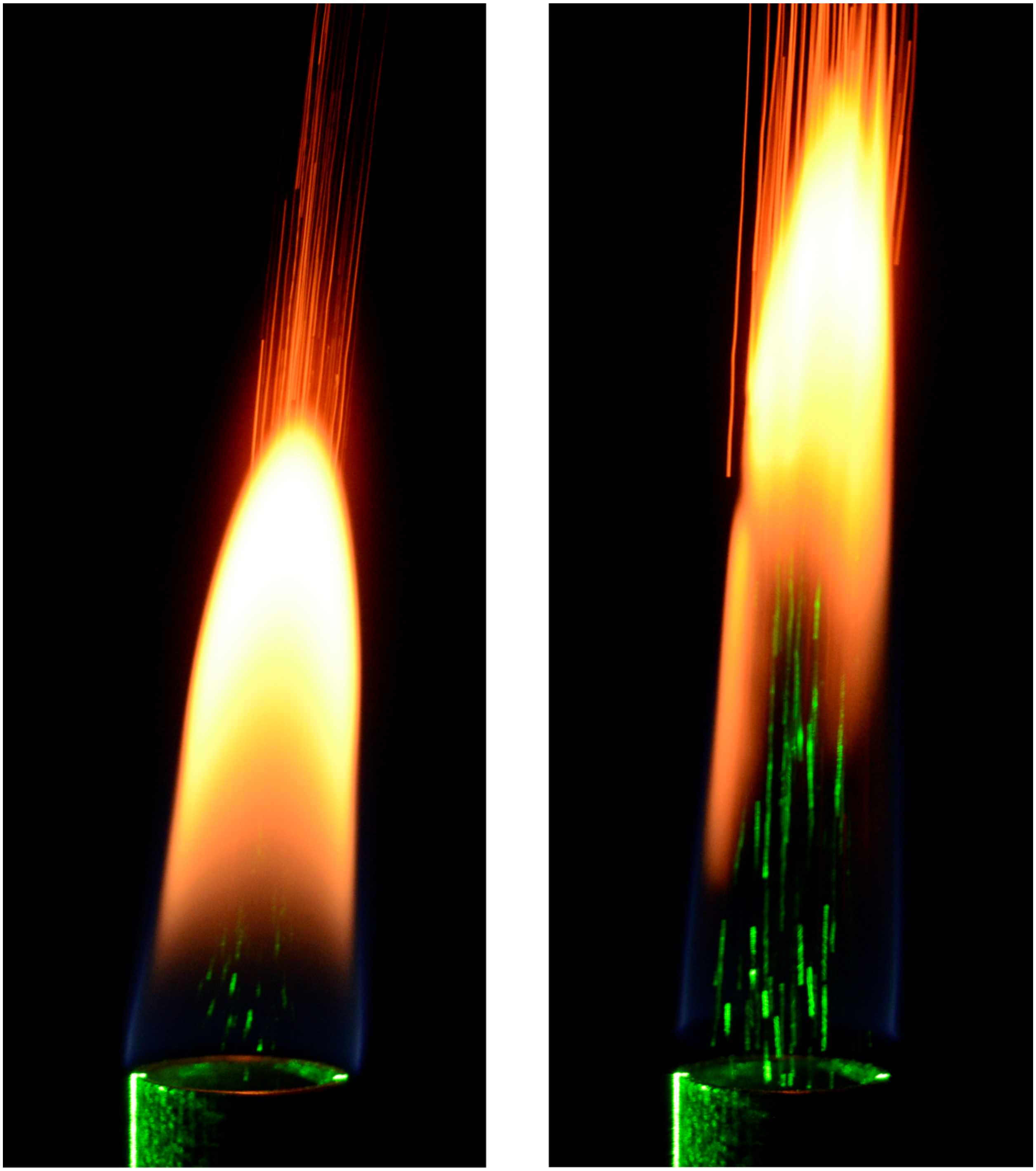

(a) **(b)**

Figure 3.14: Coal particles shooting through (a) Diffusion flame (b) Flame diluted with N_2. Laser sheet present.

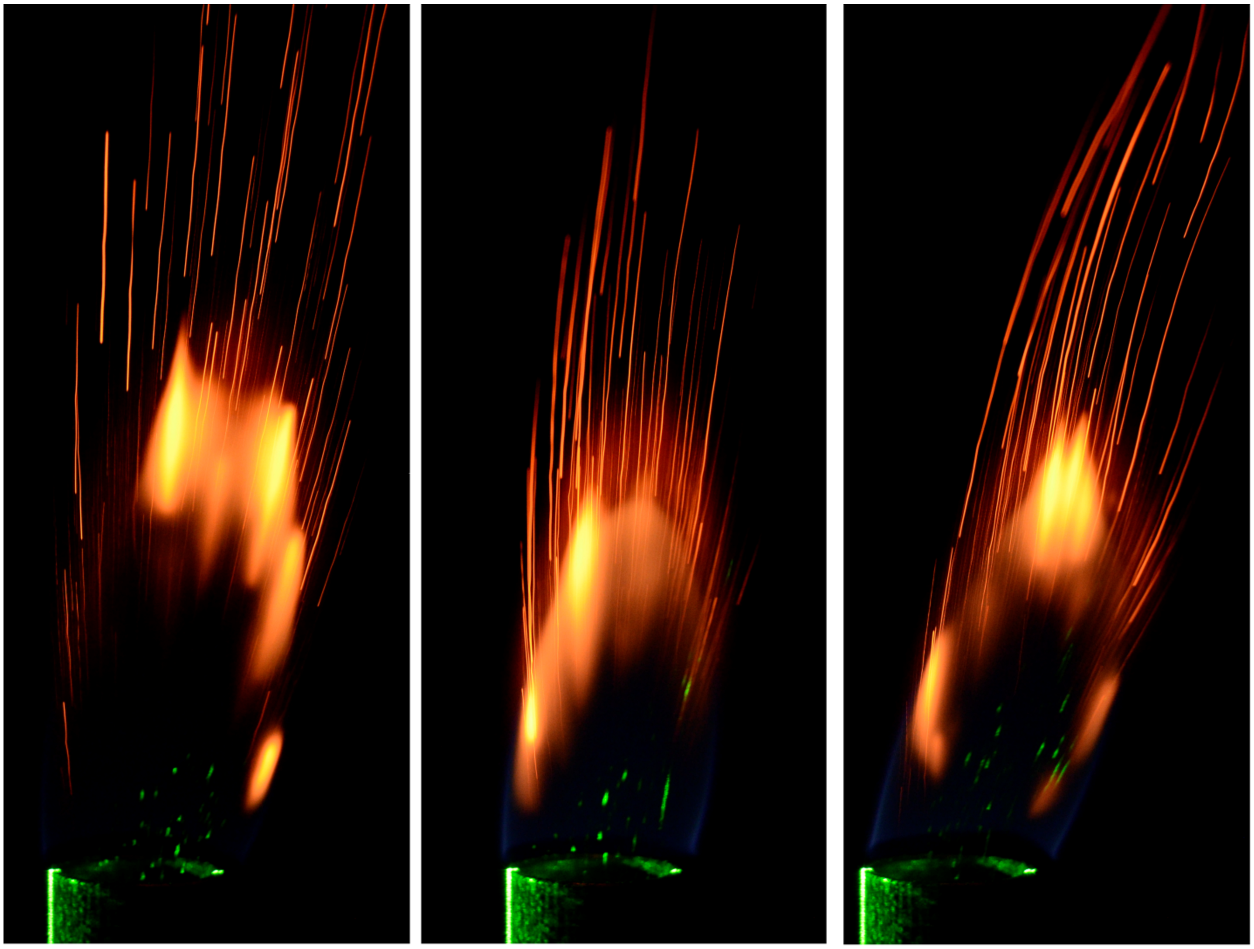

Figure 3.15: Coal particles interacting with the flame front (Laser sheet present).

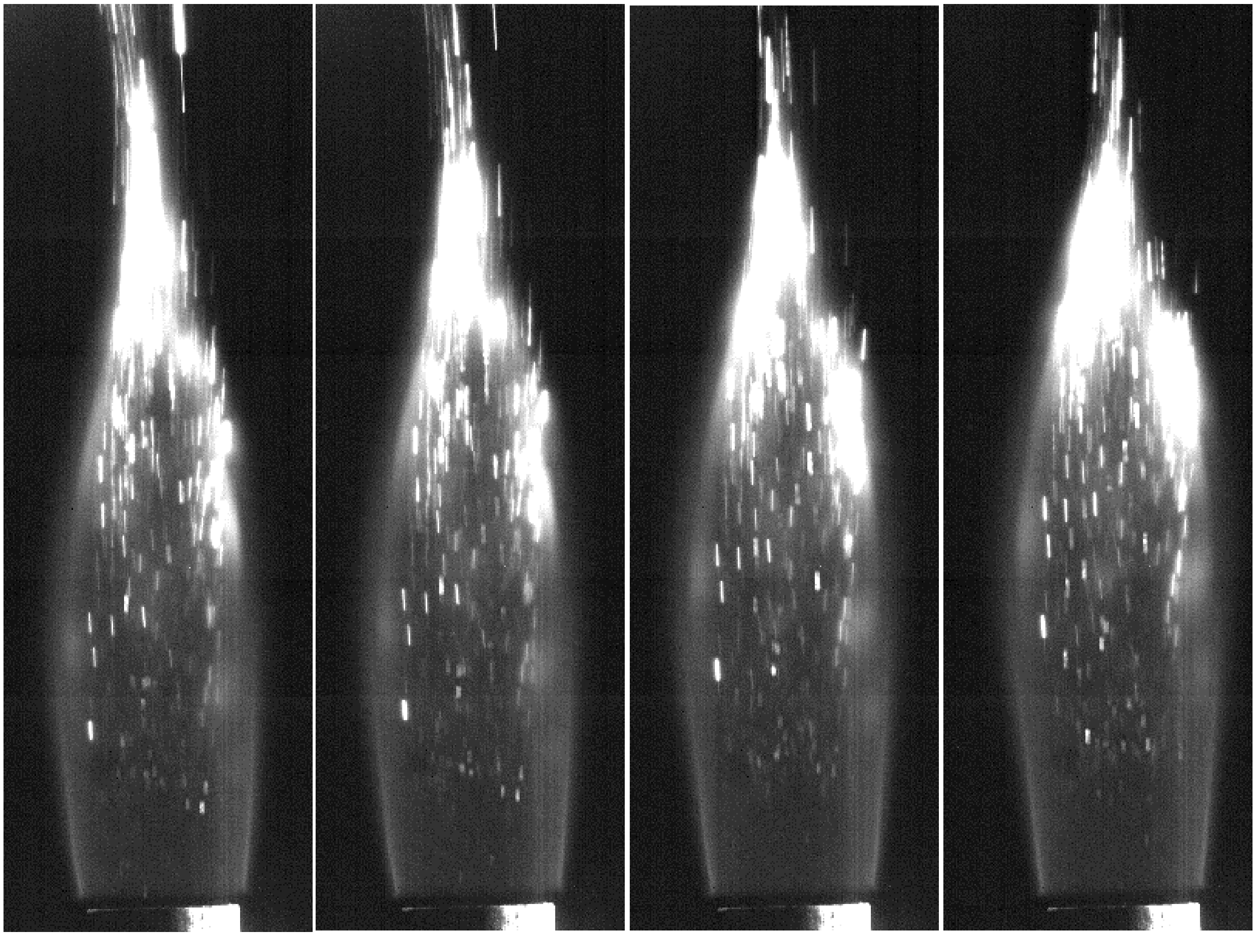

Figure 3.16: High-speed snapshots showing coal particles as they shoot through the flame.

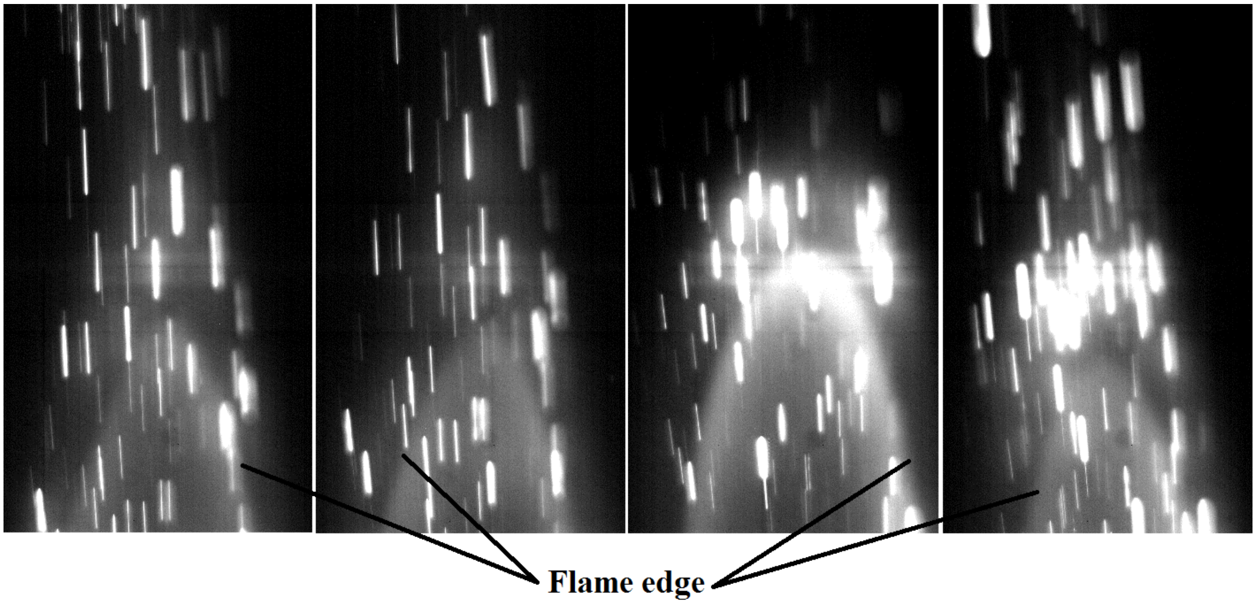

Figure 3.17: High-speed snapshots showing the trajectory of coal particles as they shoot through the flame.

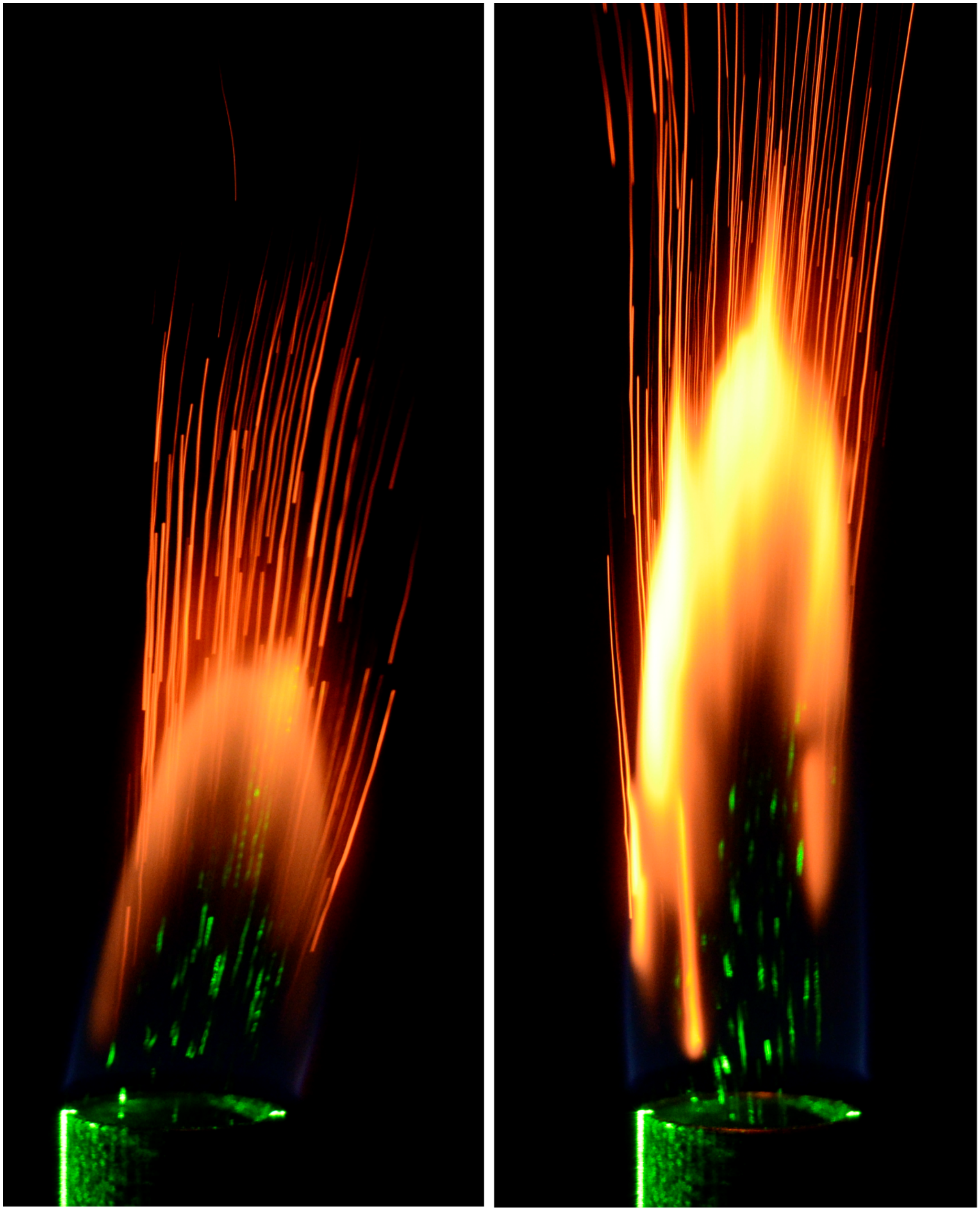

Figure 3.18: Coal particles accelerating as the approach the flame front (Laser sheet present).

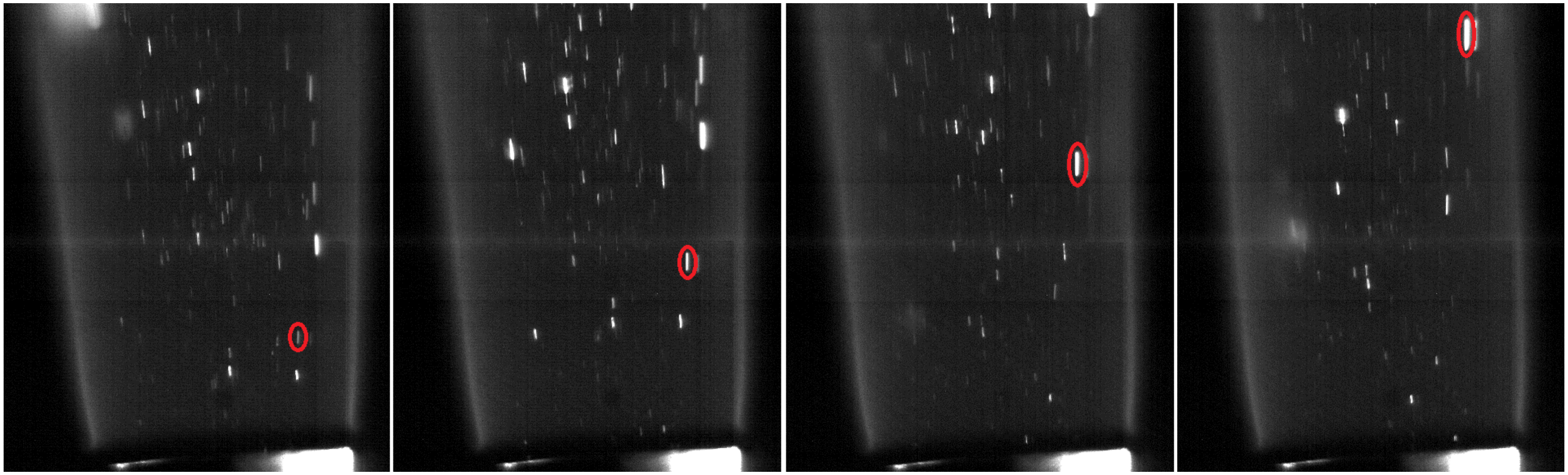

Figure 3.19: High-speed snapshots showing coal particles accelerating as they approach the flame front.

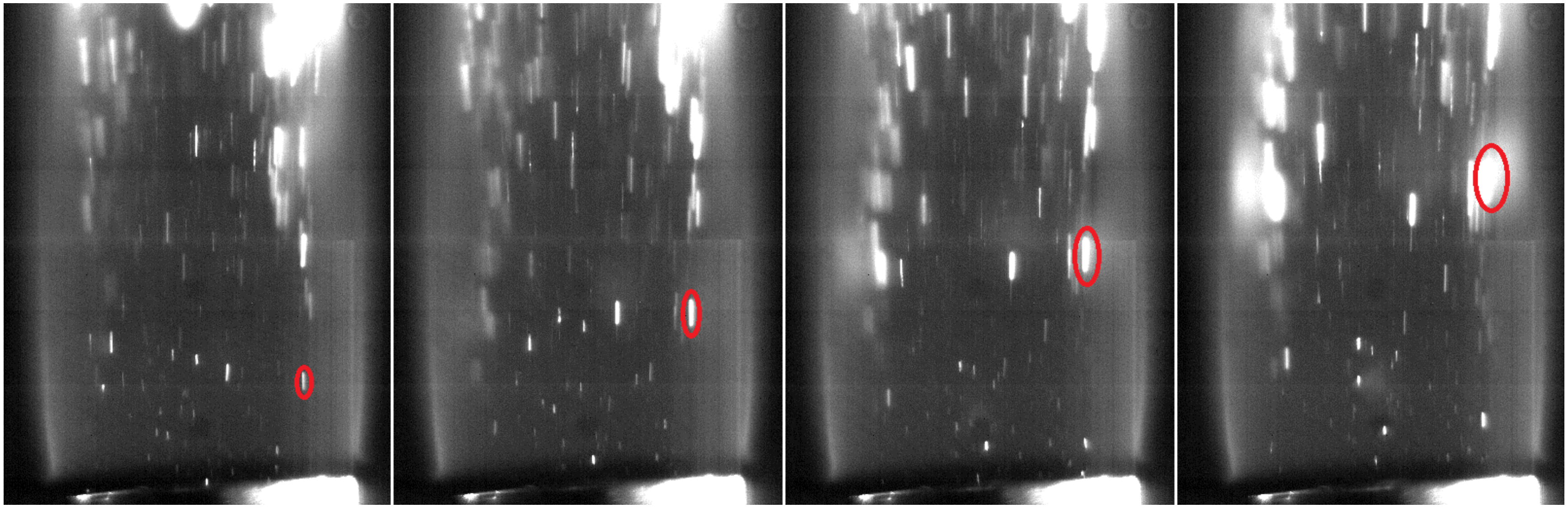

Figure 3.20: High-speed snapshots showing coal particles accelerating and interacting with the side of the flame front.

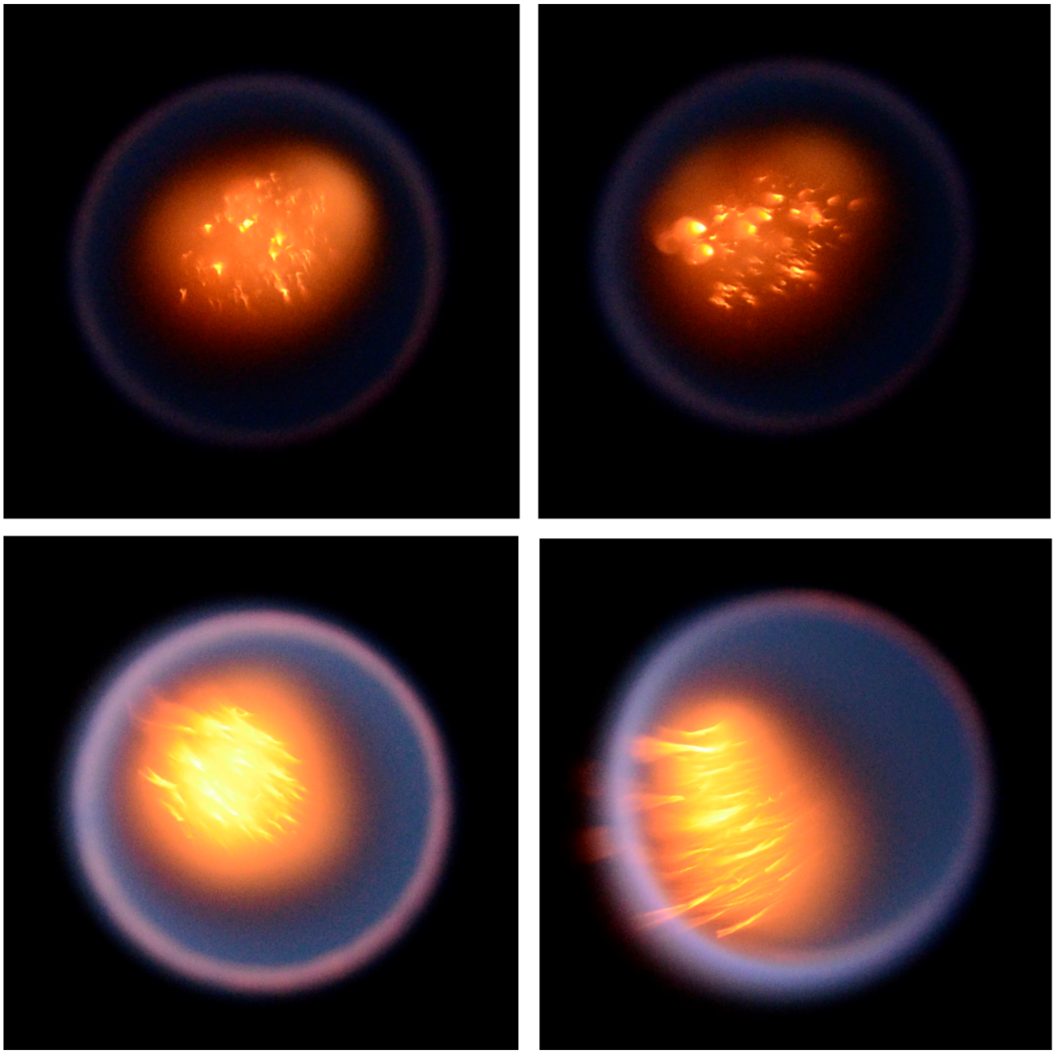

Figure 3.21: Top view of the flame showing the coal particles as they approach the flame front. (No laser sheet present).

Figure 3.22: Top view of the flame showing the coal particles as they shoot through the flame front. (No laser sheet present).

3.5 Particle Size Analysis

3.5.1 Effect of Optical Properties of Coal on Particle Size Measurement

The Malvern RT 97 Spraytec droplet-size measurement instrument employs laser diffraction for particle size measurement. The system is capable of performing the particle size analysis either using the complete Mie theory or the Fraunhofer approximation, which is basically a simplified version of the Mie theory.

Mie theory describes the scattering and absorption of electromagnetic radiation by spherical particles by providing complete solution to Maxwell equations. Mie theory uses the refractive index difference between the particle and the dispersing medium to predict the intensity of the scattered light. It also describes how the absorption characteristics of the particle affect the amount of light which is transmitted through the particle and either absorbed or refracted [36].

The Fraunhofer theory represents an approximation of the Mie theory. Fraunhofer approximation describes the portion of light deflection that occurs exclusively as a result of diffraction. For particles sufficiently large when compared to the wavelength of light, the diffraction pattern in the far field can be determined according to the Fraunhofer theory by applying Huygens's principle to the blocked wavefront, without reference to the particular optical properties of the blocking particle. One major advantage of Fraunhofer theory lies in the fact that no knowledge of the optical properties of the examined material is required. For particle diameters on the order of the wavelength of light, this approximation is inadmissible and the complete Mie theory must be utilized for the calculating particle size distributions [36].

The Fraunhofer approximation represents the easiest model to set-up in the Spraytec systems as it does not require the user to provide any optical property information. This is because the phase angle of the scattered light can be directly related to the particle size without using any of the optical properties. On the other hand the complete Mie theory requires the refractive index as one of the user input for computing the particle size distribution. The Fraunhofer approximation makes the following assumptions regarding the nature of the particles being measured:

- The particles being measured are spherical.
- The particles being measured are opaque.
- The particles are homogeneous.
- Particles of all sizes scatter light with the same efficiency.
- The suspension is dilute, such that the scattered light is measured before it is re-scattered by other particles.
- Light is scattered only at narrow angles.
- The refractive index difference between the particle and surrounding medium is infinite.

Particle size measurements for coal were performed using the simplified Fraunhofer approximation. The following considerations are to be kept in mind while using Fraunhofer approximation to measure particle size distribution [30].

- **Particle Absorption**: If the particles show some transparency (absorption < 0.2), then the Fraunhofer approximation will tend to yield inaccurate results for particles below 50 μm in size. If the absorption is high (> 0.2), good results may be obtained down to 2 μm in size, although this does depend on the refractive index.
- **Particle Refractive Index**: If the refractive index difference between the particle and the medium which surrounds it is low (n-1 << 1), then the Fraunhofer model can show errors, even up to very large particle sizes (> 200 μm).
- **Particle Size**: If the particle size distribution contains particles less than 2 μm in size then the Fraunhofer approximation will lead to an incorrect assessment of the fine particle fraction.

For coal samples that were analyzed in our experiments, the particle absorption, refractive index and size were well within the limits of the above assumptions.

- **Particle Absorption**: Pulverized coal particles are almost opaque and hardly show any transparency. The complex part of the refractive index indicates the amount of absorption loss as light passes through the material. For coal, this complex part ranges from around 0.2 to 1.2 [31, 32], which is above the threshold limit of absorption required for the Fraunhofer approximation to work. Also since, most particles other than the only sample of fine coal dust were above 178 μm in terms of the particle diameter, fairly accurate results can be obtained even if absorption was less than 0.2.

- **Particle Refractive Index**: The real part of the refractive index of pulverized coal ranges from 1.6 to around 2.7 [31, 32]. This results in a considerable difference in the refractive index between the particle and the medium (air) which surrounds it, thereby minimizing the errors involved in particle size measurement using Fraunhofer approximation.
- **Particle Size**: Since, most particles other than the only sample of fine coal dust were above 178µm in terms of the particle diameter which is much higher than the threshold limit of required particle size, Fraunhofer approximation will not lead to any incorrect assessment of the fine particle fraction.

These justifications about the assumptions involved in the nature of particles were convincing enough to suggest the use of Fraunhofer approximation in the Malvern system to measure particle size distribution of coal particles. Thus the data obtained was reliable despite no optical properties being used for particle size analysis. The only caveat in this analysis is that both Mie theory as well as Fraunhofer approximation requires the particles to be spherical. Coal particles cannot be simply treated as spheres and Mie theory does not apply even when intensities are averaged over many particles [37]. But however SEM analysis done on particles reveal that most particles are almost spherical which makes this approximation a legitimate one.

Also some preliminary particle size distribution analysis was attempted using a PDA (Phase Doppler Anemometry) system. The objective was to compare two individual optical measurement techniques namely the PDA and the Malvern for particle size measurement of pulverized coal particles. The PDA can be operated in two modes: Refraction mode and Reflection mode. Since the coal particles were opaque, measurement could not be taken using the refraction mode. However data taken using the reflection mode was highly erratic and unreliable. The spherical validation that measures the sphericity of the particles was hardly around 5 %, whereas a minimum of 70 % was required in order for the system's internal validation to classify the data as reliable and consistent. In addition to this, the particle size distribution generated a phase function that was scattered all around instead of the uni-modal distribution that was to be expected if the data had been reliable. Thus, based on the low spherical validation values, erratic and inconsistent data and scattered values of the phase function, it can be concluded that the PDA system simply cannot be used for non-spherical particles for size measurement.

3.5.2 Diffusion Flame

Particle size distributions were obtained before and after combustion for all the 11 different pre-sorted coal samples using the Malvern RT 97 Spraytec droplet-size measurement instrument by creating a coal-laden jet with the help of the experimental setup described in section 2.2. The Malvern system was used in the Fraunhofer approximation regime, which does not require any input of optical properties from the user for size distribution measurements. The Spraytec system was loaded with the calibration library ST45AIAC.cal which corresponded to a standard 450 mm lens on the detector side, a default opaque refractive index of 1.5+0.50i for the particles and a the refractive index of 1+0.00i for the surrounding air.

The Malvern was operated in the flash mode; and data were acquired at a rate of 500 Hz over a time period of 2000 ms for each trial to get an average particle size distribution. The duty cycle was maintained at 50 % for all the experiments. Before every experiment was conducted, a background and a reference noise signal were recorded. In order to minimize the effects of beam steering due to the flame, post-combustion particle size measurements were not carried out above the flame as the particles cross the flame zone. Instead, the burnt coal particles were collected once they passed through the flame and they were again entrained to create a jet now laden with burnt coal particles, which was used to determine the particle size distribution after combustion.

Each experiment was repeated for at least five trials at a given set of conditions. The particle size distribution was then computed as the average of the five trials. The mean volume percentages for each particle diameter for the different samples before and after combustion are presented graphically in this section. The error bars in the graph correspond to one unit of standard deviation. The abscissa for the graphs is the average between the lower and upper values of each particular bin size as recorded by the Malvern instrument. Detailed information on these bin sizes and the raw numeric data for each particle size distribution before after combustion along with the standard deviations from the five trials can be found in Appendix C.

The particle size distributions before and after combustion for the various sizes of coal particles ranging from sieve size: 18-20 to sieve size: < 80 is presented in Figures 3.23 - 3.33. From the figures, it is evident that the particle size distribution before and after combustion for almost all the samples is clearly uni-modal. The position of the uni-modal peak in each of the particle size distributions in terms of particle diameter is in good agreement with the average particle size diameter obtained previously through the sieving process. This good agreement in particle diameter from the Malvern size measurements and the sieving process can be considered that as a good indication that the Malvern size measurements are reliable and within the range of acceptable errors.

It is to be noted that the uni-modal peak shifts progressively towards smaller particle diameters as one moves from Figure 3.23 to Figure 3.32, which indicates decreasing particle size of the coal samples. The only discrepancy in terms of the particle size distribution can be seen in Figure 3.33 for the case of fine coal dust. The mean diameter for this sample from the sieving process was estimated to be less than 178 μm, but however Malvern size distributions provide a uni-modal peak centered around 500 μm. However, there is also another small peak centered at around 170 μm which correlates well with the expected particle size diameter of the coal sample.

This discrepancy in particle size distribution for the fine coal dust can be attributed due to the assumptions that were made earlier in employing Fraunhofer approximation for Malvern particle size measurements. This particular coal sample was near the limit of validity of the Fraunhofer approximation in terms of particle size (< 200 μm) [30]. The finest coal sample had a wide range of coal particles in terms of diameter ranging from a few microns to a few hundreds of microns. As discussed earlier in section 3.5.1, due to the smaller particle sizes in this sample, an incorrect assessment of fine particle fraction was to be expected. In addition to this, the calibration file ST45AIAC.cal used in the RT software included a default refractive index of 1.5+0.50i for the particles. The Fraunhofer approximation basically assumes that the wave front is completely blocked so the higher the index of refraction the better. Though strictly speaking, Fraunhofer approximation is not applicable only in cases where the index of refraction of the particles is too small (n-1 << 1); in our case the relatively small difference between the refractive index of the particles and the surrounding medium (~ 0.5) could be a source of potential error as the modifications imposed on the wavefront cannot be neglected. This could have led to significant errors in particle size measurements even for very large particle sizes (> 200 µm).

When comparing the particle size distribution of coal particle before and after combustion in a pure CH_4 diffusion flame, many interesting observations can be drawn. From Figures 3.23 - 3.33, it is clear that the particle size distributions before and after combustion are almost identical. It is also evident that the combustion process had a much pronounced effect on smaller coal samples (Sieve size: < 35) than on larger ones (Sieve size: > 35). When considering the particle size distribution of a particular coal sample, it is clear that the combustion process decreased the volume fraction for both the smallest and the largest size coal particles in the sample. The decrease in the volume fraction of smaller coal particles was significant when compared to those of larger coal particles. On the other hand, there was always an increase in the volume fraction of the mid-sized particles in each of these distributions. This can be attributed to two different phenomena namely, the larger coal particles started to sinter and continued to burn as they crossed the flame front, leading to a decreased particle diameter; meanwhile some of the finer coal particles were either burnt completely or agglomerated thus generating larger-diameter particles. These two processes led to an increase in the volume fraction of mid-sized particles in almost all the samples.

From the results, it is also evident that the combustion process hardly changed the mean particle diameter. This was due to the incomplete devolatilization of coal particles that led to hardly any change in mean particle diameter as result of combustion. For pulverized coal flames, it has been reported by I.W. Smith [34] that the time required for complete devolatilization is in the order of 0.1 s; but in our case, the residence time for the coal particles inside the flame front is estimated to be on the order of 0.01 s which results in only partial devolatilization, causing no change in mean particle diameter. This estimate was acquired by dividing an average particle speed with the thickness of the flame zone that was approximated as the thickness of the luminous zone in flame visualizations.

This finding is also well supported by the negligible changes observed in loose density after the combustion process. As discussed earlier in section 3.1, the loose density was found to be a function of the particle diameter. Since the particle diameter remained almost unchanged because of the small residence time, the loose density after combustion did not vary by any significant extent. Also, a slight shift was observed in the particle size distribution in terms of mean particle diameter for finer coal samples (Sieve size : < 70) towards smaller particle sizes after combustion. That shift was reflected as a significant change in the corresponding loose density measurements made after combustion for these samples when compared to coarser coal samples.

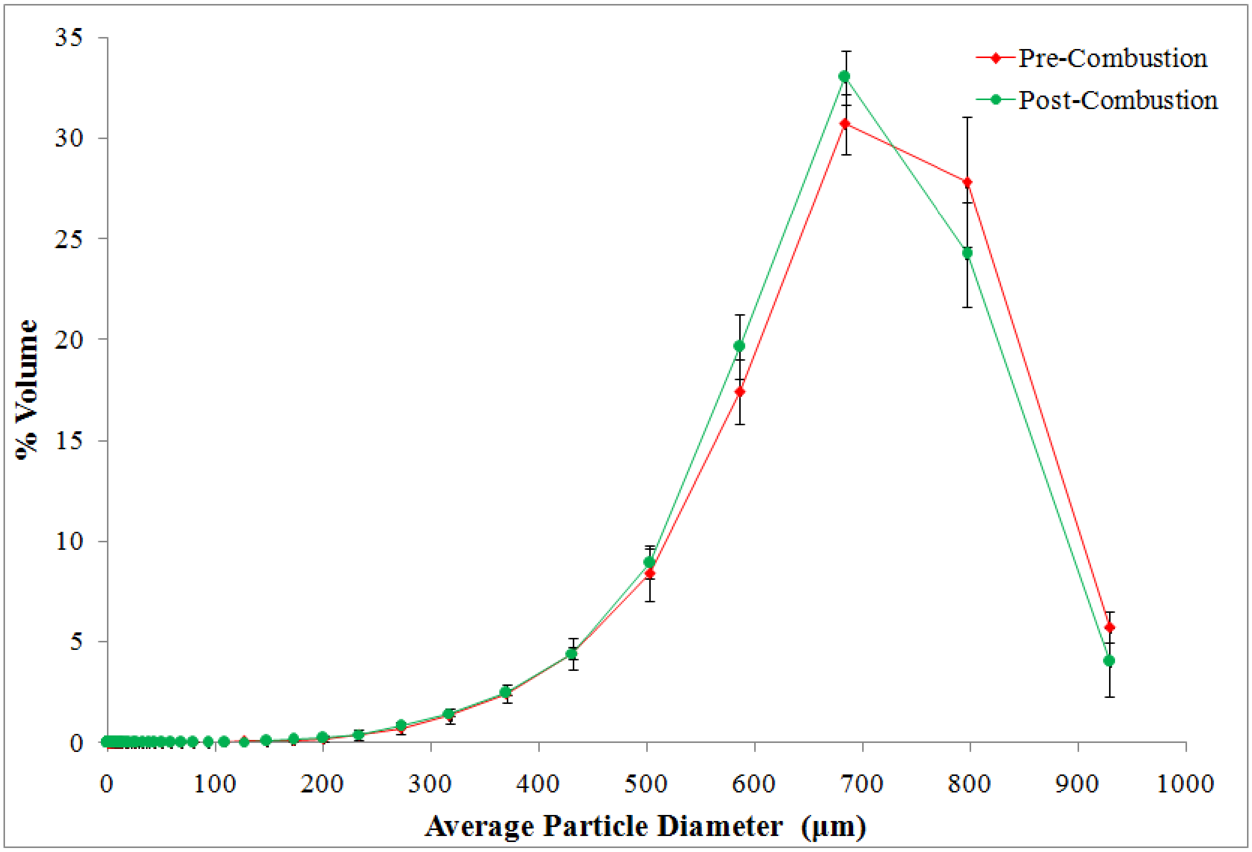

Figure 3.23: Particle size distribution of coal particles before and after combustion. (CH_4 diffusion flame; Sieve size: 18-20).

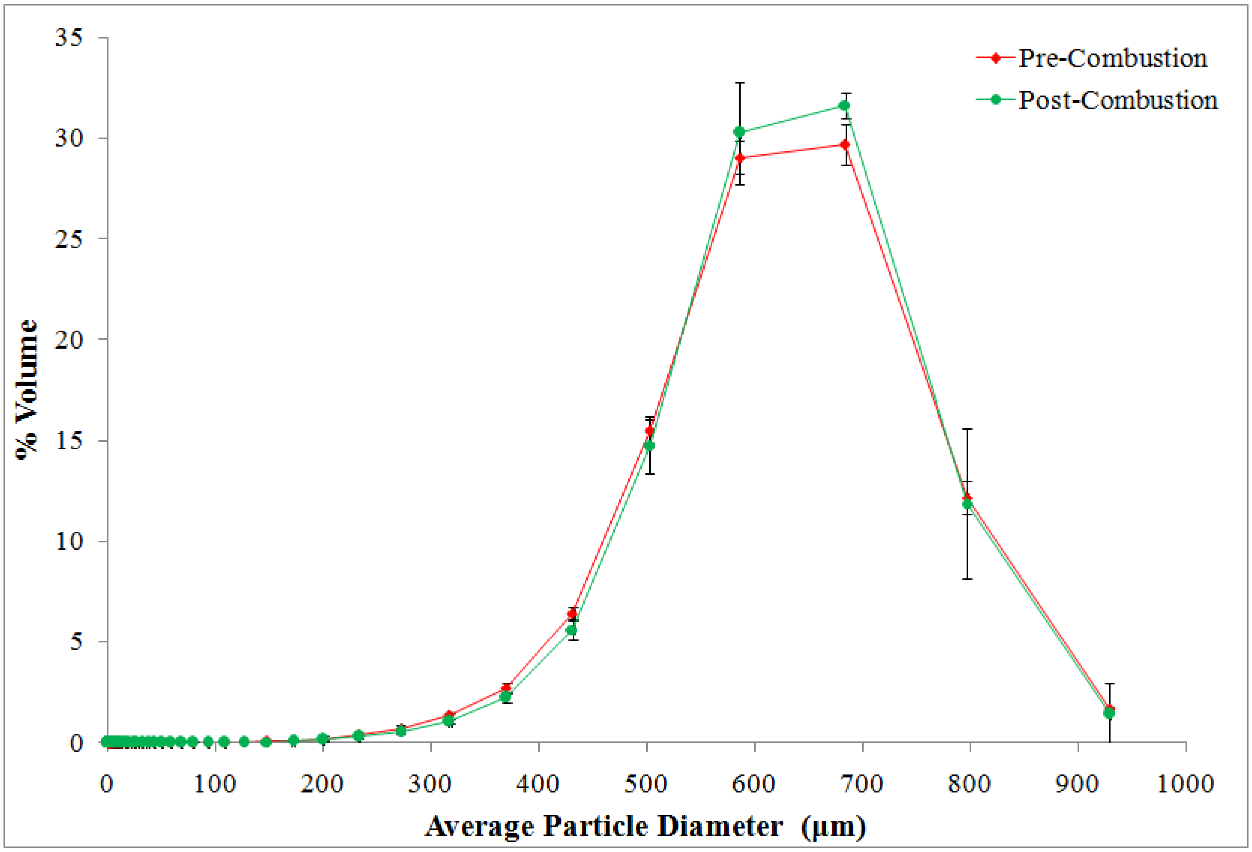

Figure 3.24: Particle size distribution of coal particles before and after combustion. (CH_4 diffusion flame; Sieve size: 20-25).

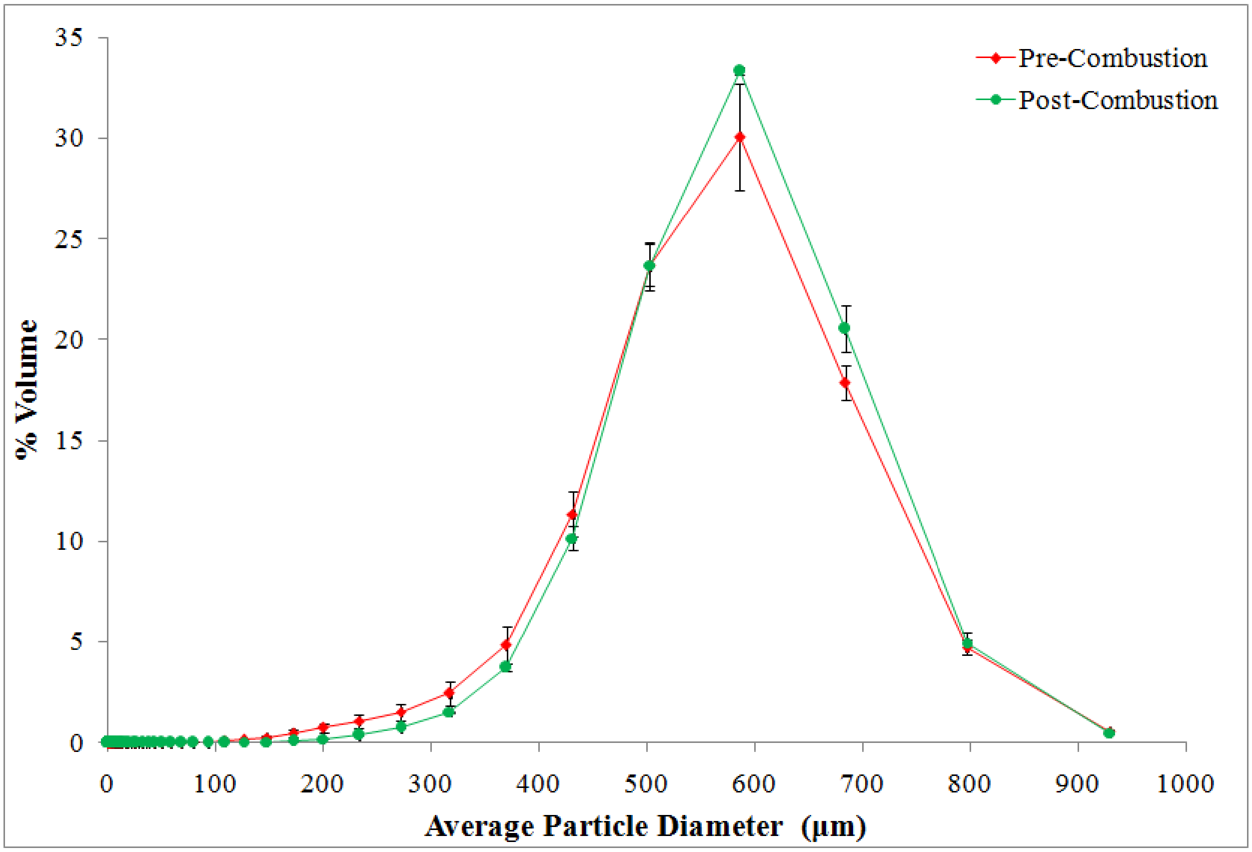

Figure 3.25: Particle size distribution of coal particles before and after combustion. (CH_4 diffusion flame; Sieve size: 25-30).

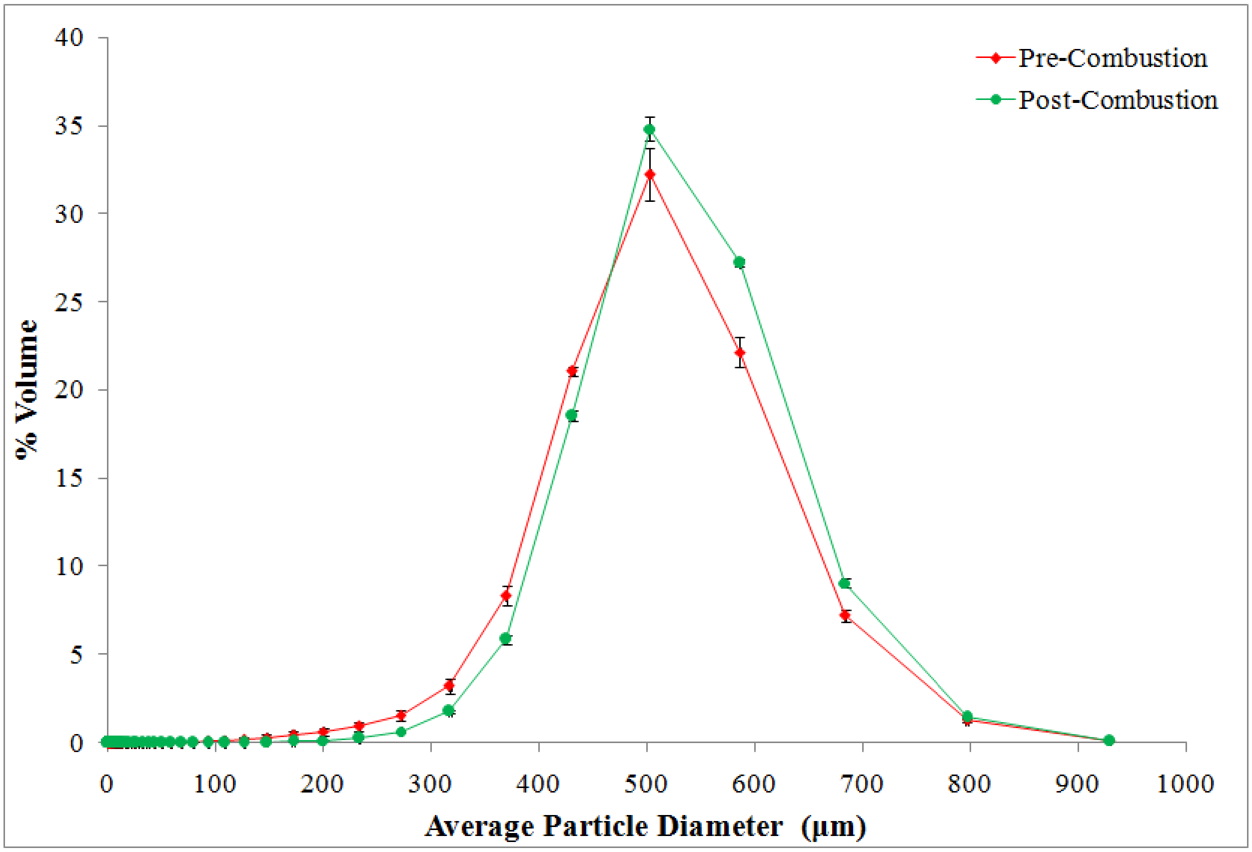

Figure 3.26: Particle size distribution of coal particles before and after combustion. (CH_4 diffusion flame; Sieve size: 30-35).

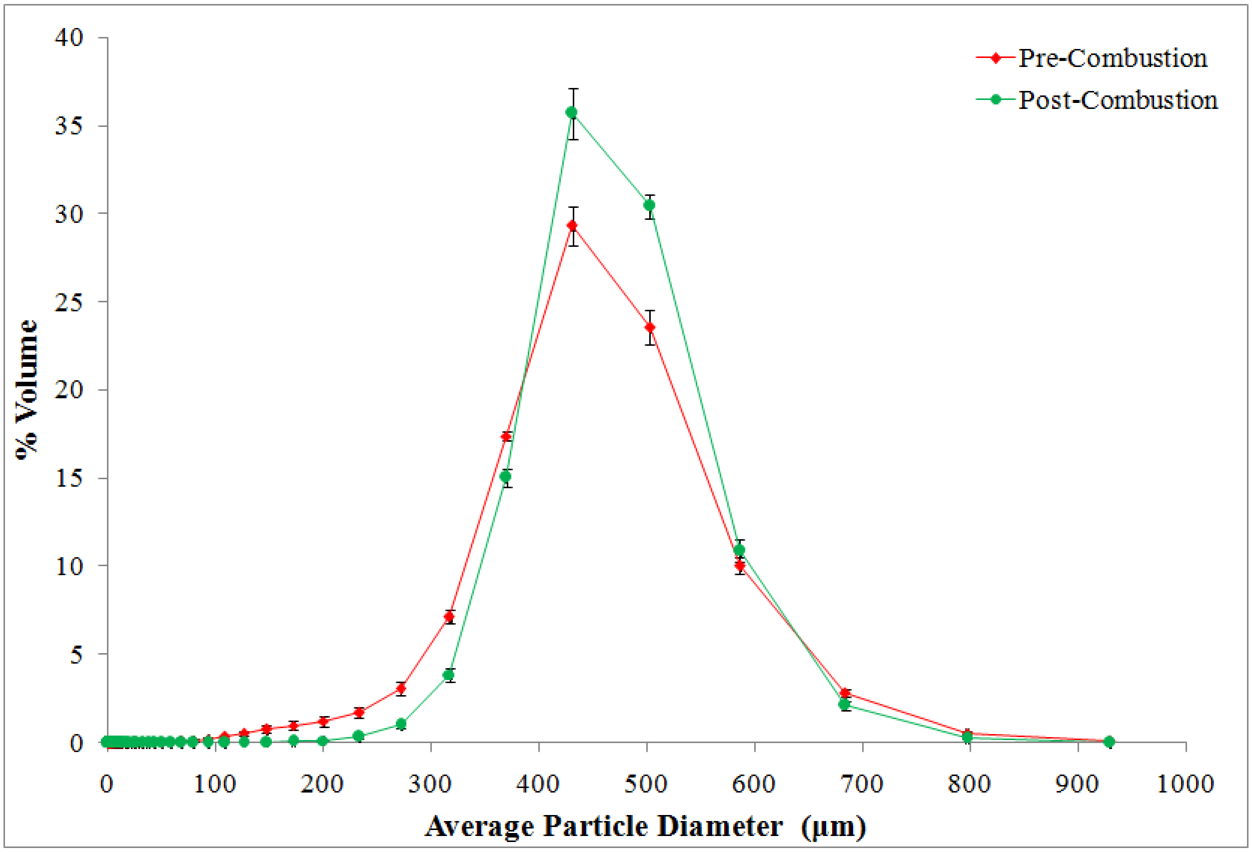

Figure 3.27: Particle size distribution of coal particles before and after combustion. (CH_4 diffusion flame; Sieve size: 35-40).

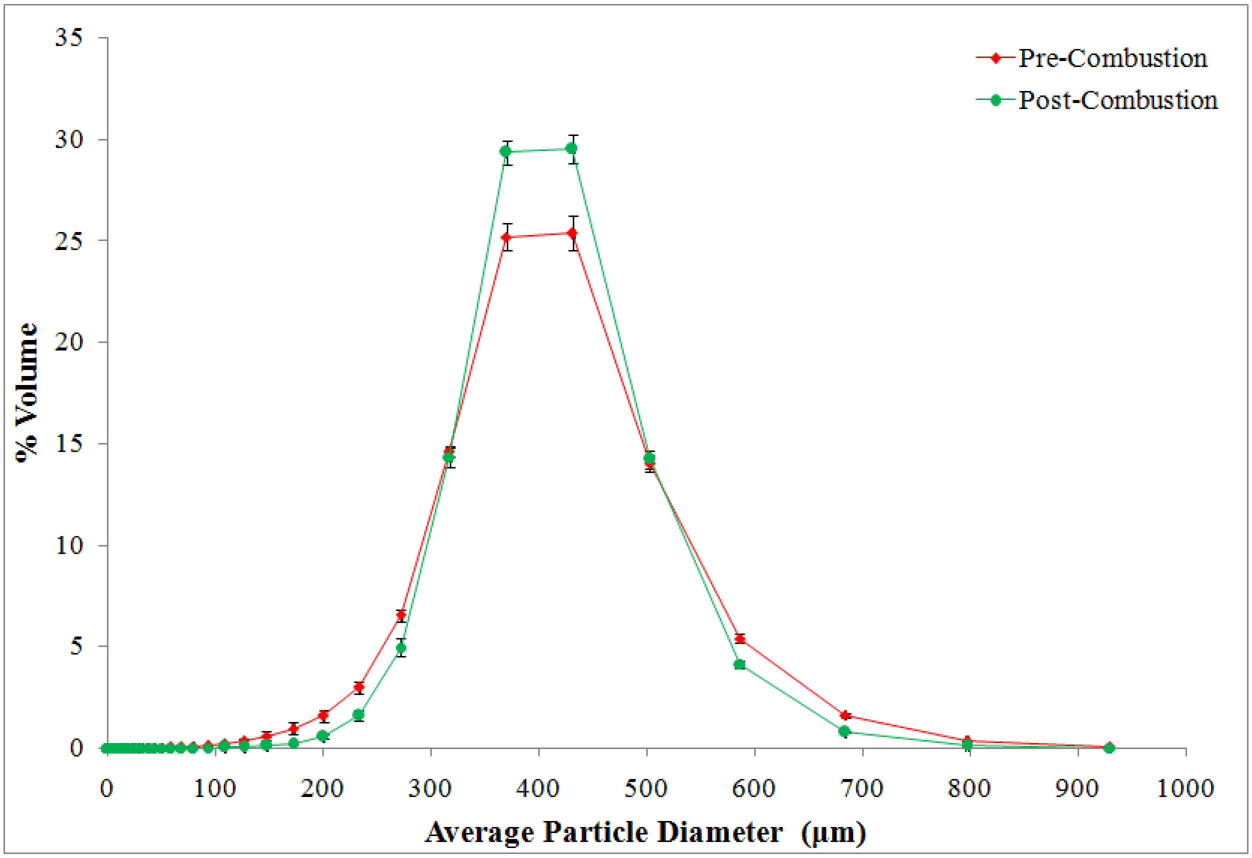

Figure 3.28: Particle size distribution of coal particles before and after combustion. (CH_4 diffusion flame; Sieve size: 40-45).

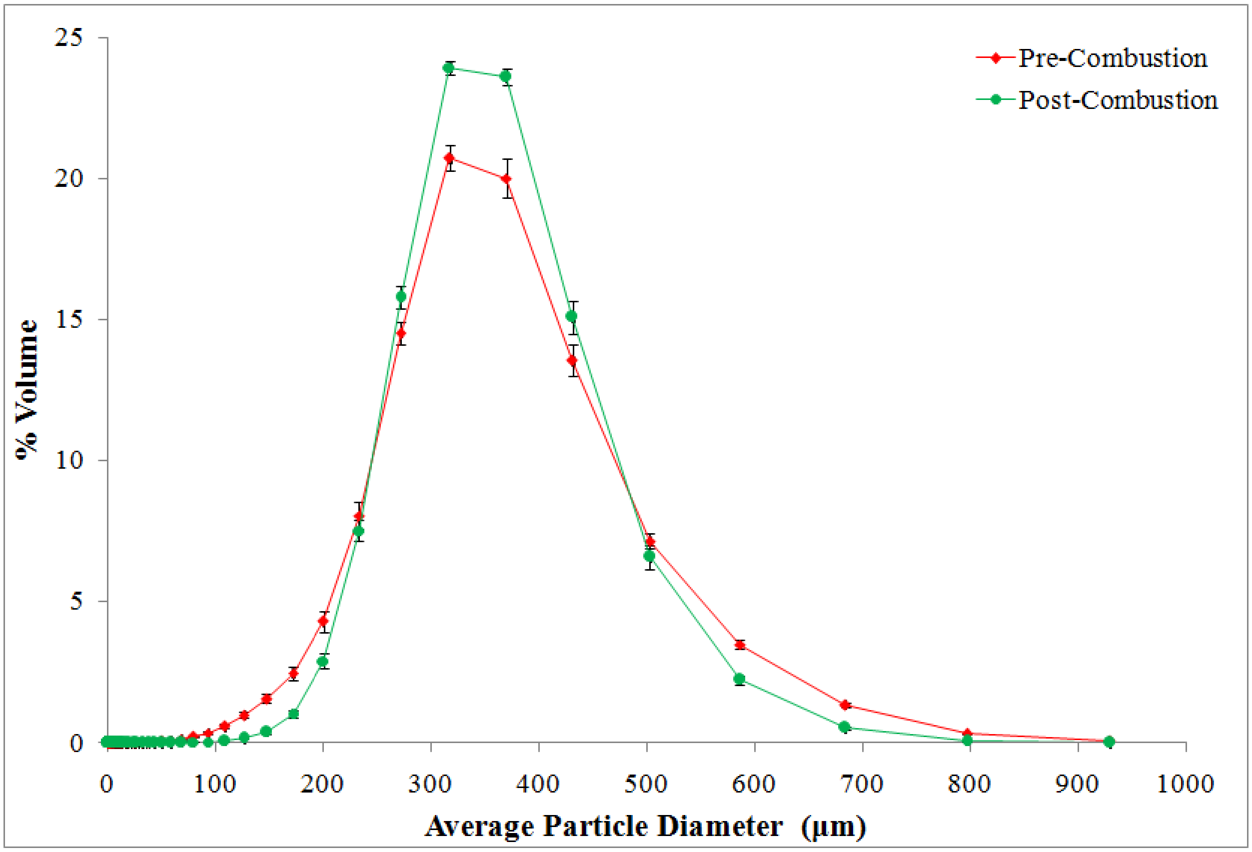

Figure 3.29: Particle size distribution of coal particles before and after combustion. (CH_4 diffusion flame; Sieve size: 45-50).

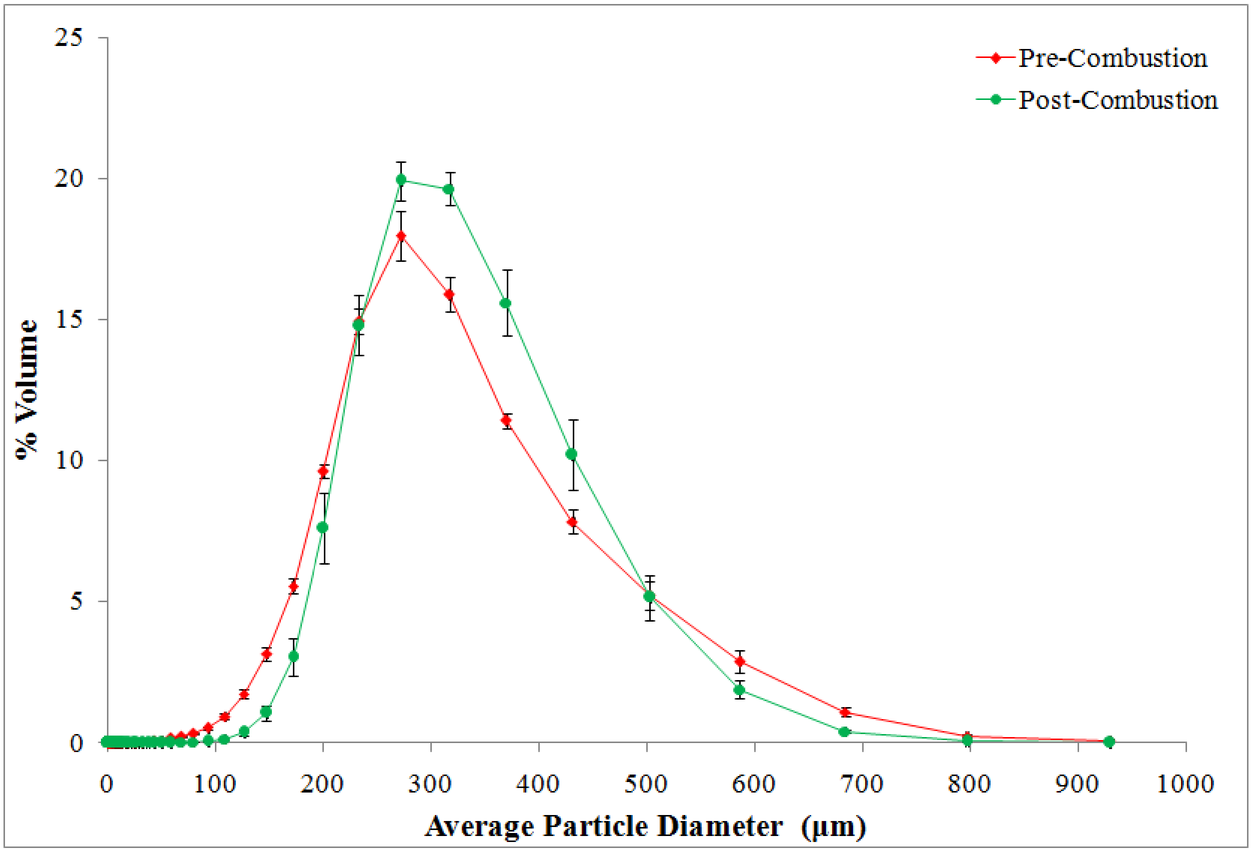

Figure 3.30: Particle size distribution of coal particles before and after combustion. (CH_4 diffusion flame; Sieve size: 50-60).

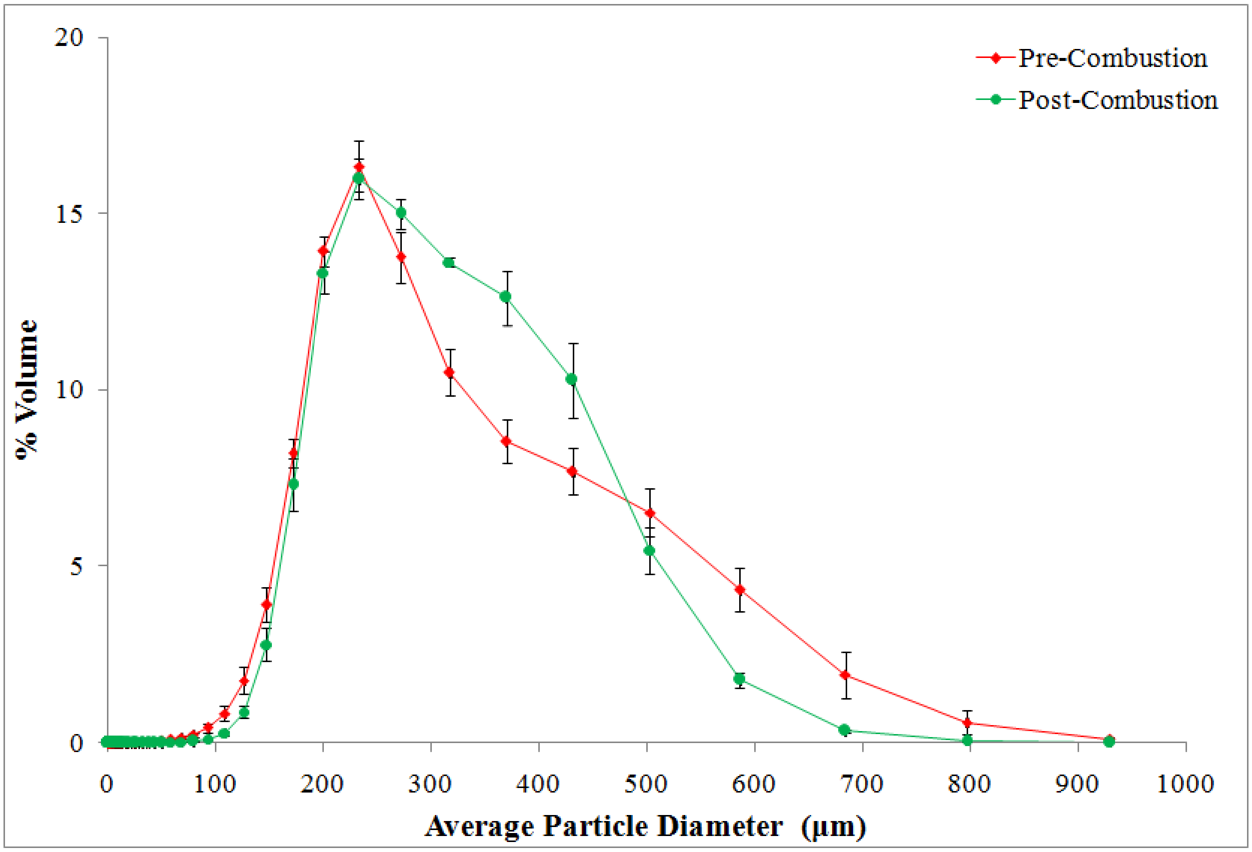

Figure 3.31: Particle size distribution of coal particles before and after combustion. (CH_4 diffusion flame; Sieve size: 60-70).

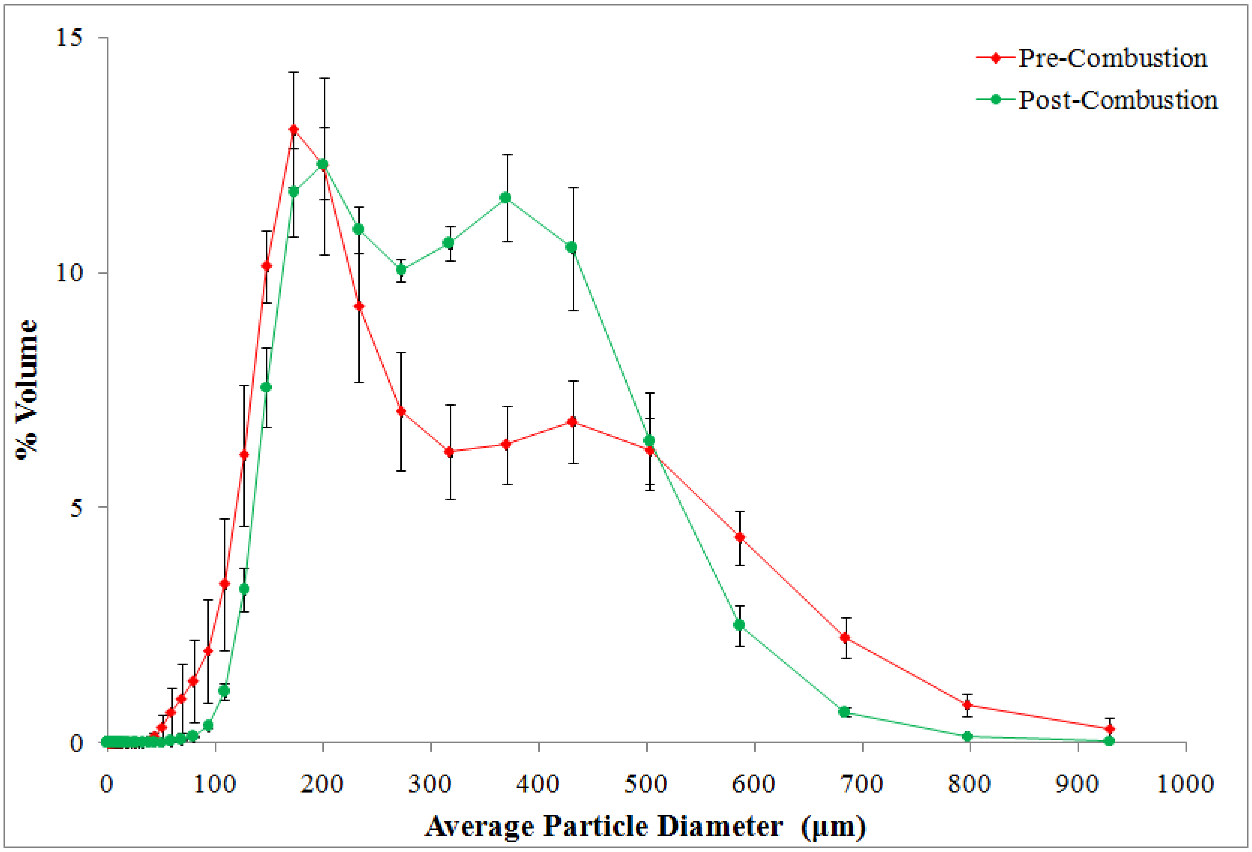

Figure 3.32: Particle size distribution of coal particles before and after combustion. (CH_4 diffusion flame; Sieve size: 70-80).

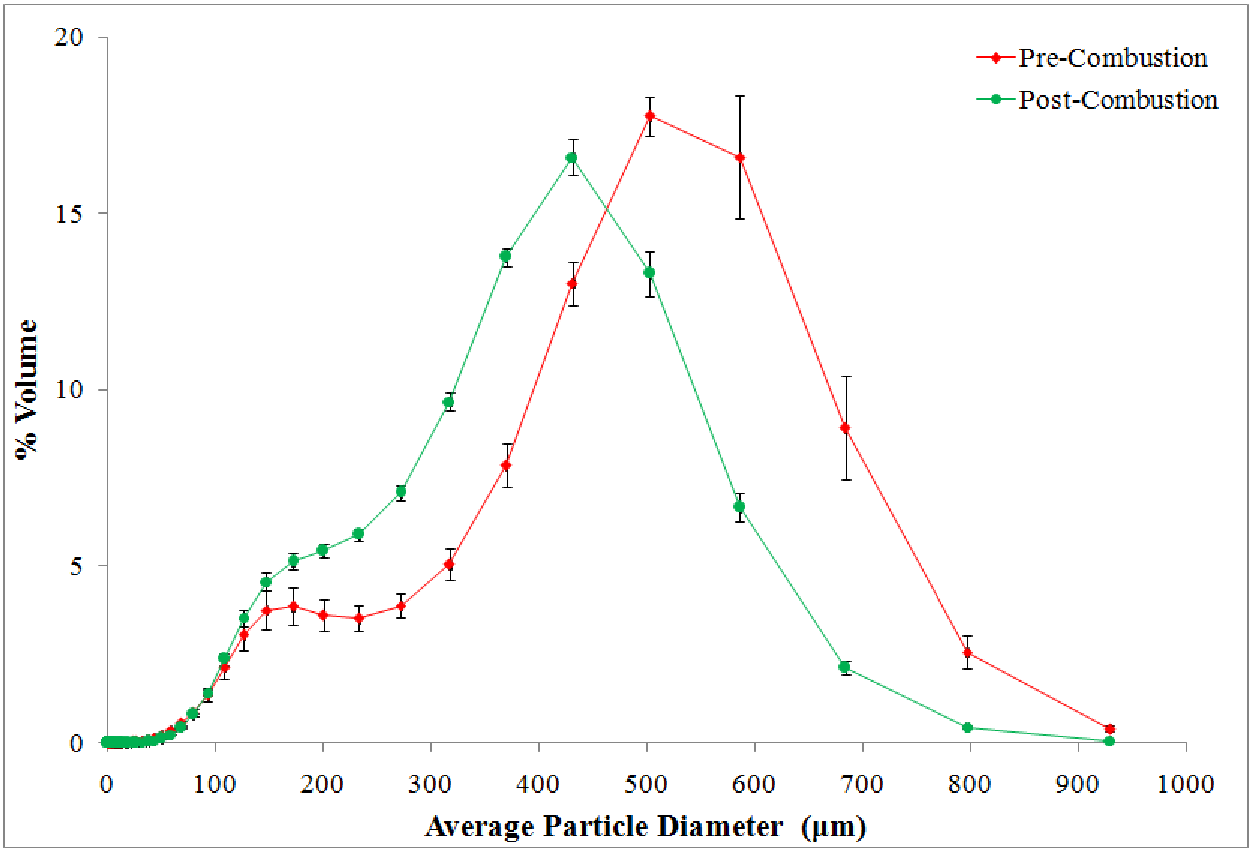

Figure 3.33: Particle size distribution of coal particles before and after combustion. (CH_4 diffusion flame; Sieve size: < 80).

3.5.3 Premixed Flame

In order to compare the effect of nature of the flame on particle size distribution of coal particles before and after combustion, two representative coal samples namely sieve size: 40-45 and < 80 were selected for analysis. These coal samples were then entrained and subjected to the following types of premixed flames:

- CH_4/air premixed flame at stoichiometric conditions ($\phi = 1$).
- $CH_4/O_2/CO_2$ premixed flame at stoichiometric conditions ($\phi = 1$).
- CH_4/O_2 premixed flame at stoichiometric conditions ($\phi = 1$).

In addition to maintaining the air-fuel ratios of these flames at stoichiometric conditions, it was ensured that the CH_4/air and the $CH_4/O_2/CO_2$ premixed flame had the same adiabatic flame temperature by suitably adjusting the amount of CO_2 in the combustible mixture. The relative proportion of the gases in the combustible mixture required in order to maintain constant adiabatic flame temperature was evaluated using a chemical equilibrium solver GASEQ by iteration. The mole fractions of the constituent gases in the premixed flame and the adiabatic flame temperatures are presented in Table 3.2.

S.No.	**Type of Premixed flame**	**Adiabatic Flame Temperature (K)**	**Mole Fraction of CH_4**	**Mole Fraction of N_2**	**Mole Fraction of O_2**	**Mole Fraction of CO_2**
1	CH_4/air	2226.4	0.095	0.715	0.190	-
2	$CH_4/O_2/CO_2$	2226.4	0.139	-	0.277	0.584
3	CH_4/O_2	3053.9	0.333	-	0.667	-

Table 3.2: Adiabatic flame temperature and mole fraction of constituent gases in the combustible mixture for various premixed flame types based on GASEQ.

The particle size distributions before and after combustion for coarse (Sieve size: 40-45) and fine (Sieve size: < 80) coal particles presented in Figure 3.34 and 3.35 respectively. It is evident from these graphs, that the particle size distributions obtained with the premixed flame is qualitatively similar to those obtained with the diffusion flame. This can be attributed to similar residence times (~ 0.01 s) associated with both types of flames.

The variation in particle size distribution was found to be more significant in case of finer coal particles. Similar to what was observed with the diffusion flame, there was a decrease in the volume fraction of both smaller and larger size coal particles and a nominal increase in the volume fraction of mid-sized particles. The particle size distribution for the premixed CH_4/air and $CH_4/CO_2/O_2$ flames were almost identical. This was to be expected due to same adiabatic flame temperatures (2226 K) in both the cases. However for the CH_4/O_2 premixed flame, the variation in the particle size distribution after combustion was more pronounced. There is a slightly higher decrease in volume fraction for all diameters as shown in Figure 3.35. This was due to the fact that the coal particles in the case of CH_4/O_2 premixed flame was subjected to a slight higher adiabatic flame temperature (3053 K), that resulted in increased burning rate resulting in further decrease in particle size when compared to other premixed flames.

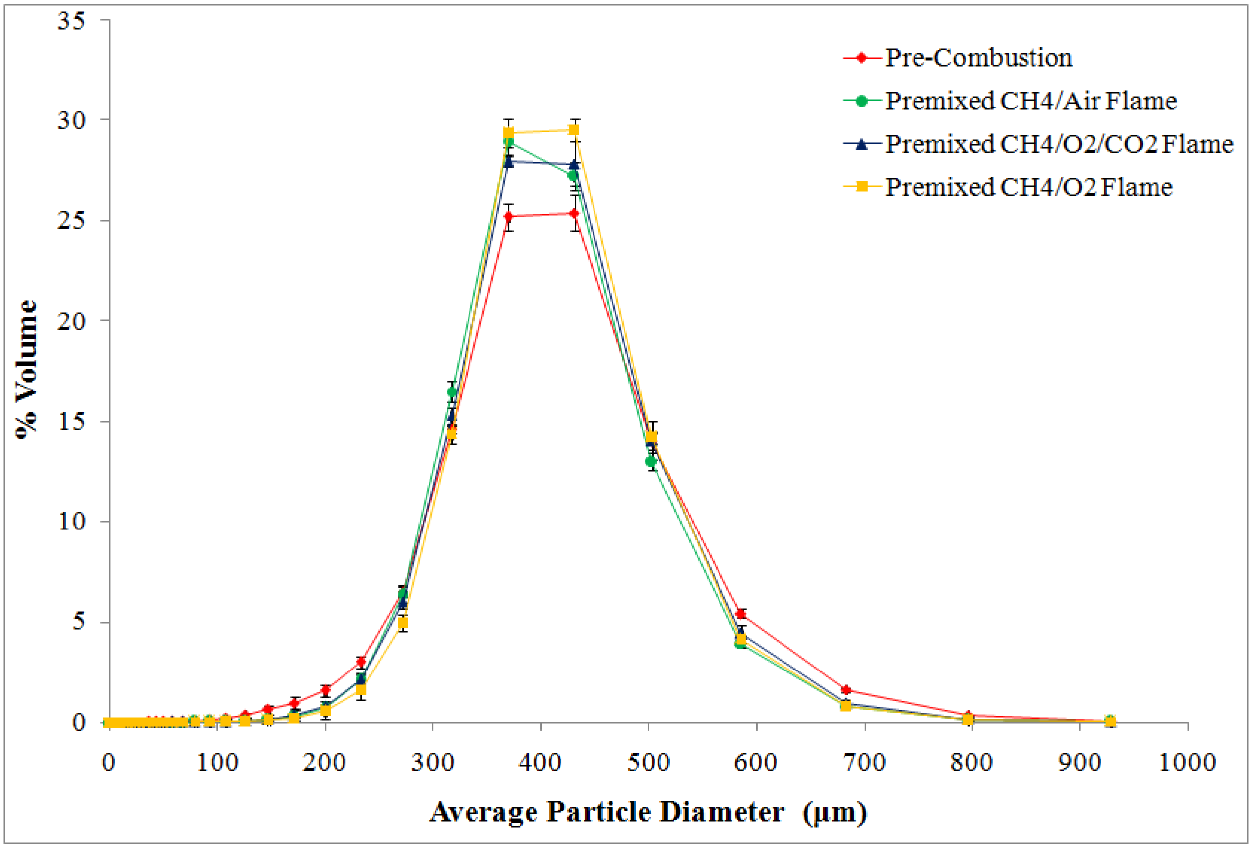

Figure 3.34: Particle size distribution of coal particles before and after combustion. (CH_4/air, $CH_4/O_2/CO_2$, CH_4/O_2 premixed flames; Sieve size: 40-45).

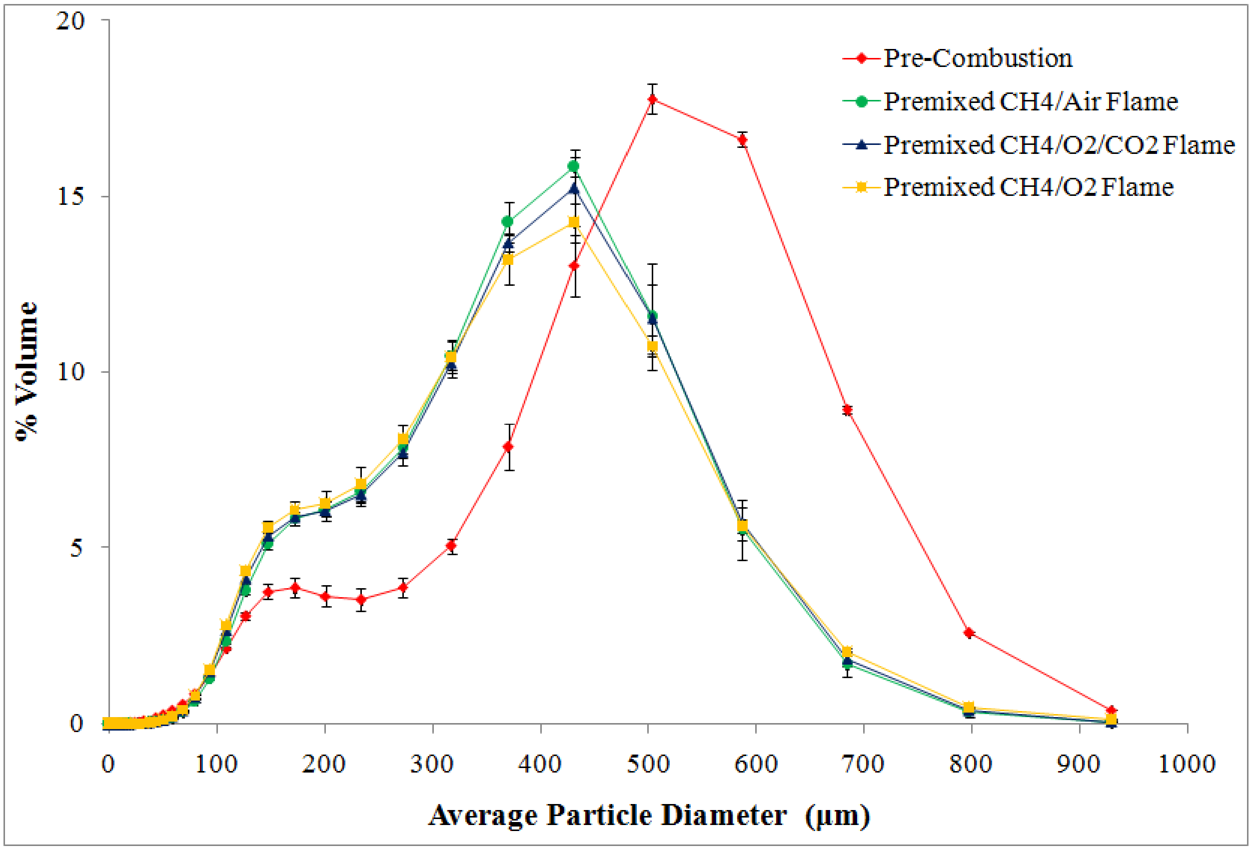

Figure 3.35: Particle size distribution of coal particles before and after combustion. (CH_4/air, $CH_4/O_2/CO_2$, CH_4/O_2 premixed flames; Sieve size: < 80).

3.6 SEM Analysis

The morphological changes induced on the macrostructure and microstructure as result of combustion was studied by analyzing selected samples of coal particles using SEM imaging. SEM photographs taken on these samples before and after the combustion process were compared to reveal any interesting changes in the morphology of coal particles due to combustion. It is remarkable to note how different the effect on macro and microstructure is.

SEM images comparing the macrostructure of the coal particles for selected sizes before and after combustion are presented in Figures 3.36 - 3.39. From these images, it is evident that the macrostructure of the coal particles was not affected to any significant extent due to the combustion process. This is attributed to the fact that the residence time for the coal particles inside the flame front was so small, that the particles did not have sufficient time to interact with the flame. So in spite of the particles undergoing a thermal shocking as they crossed the flame front; the small residence time prevented any permanent noticeable change on the macrostructure of these particles after combustion. The images presented in Figures 3.36 and 3.37, reveal that there is hardly any noticeable change in macrostructure after combustion for comparatively coarser coal particles. The coal particles even after combustion retained their sharp edges and angular features similar to that of unburnt coal particles. But on close observation it can be seen that the surface of the coal particles after combustion was less corrugated with fewer surface irregularities when compared to the one before combustion. On the other hand, the SEM images presented in Figures 3.38 and 3.39 reveal a few conspicuous changes in the overall macrostructure of the coal particles after combustion. The coal particles after combustion were more rounded with a comparatively smoother surface in contrast to the highly angular edges and corrugated surfaces before combustion. It is also interesting to note that, especially in the images presented in Figures 3.39 that many of the finer coal particles had completely vanished after combustion. This was due to the fact that these particles were too small that they had either got burnt completely or had fused together into larger particles due to the combustion process.

SEM images comparing the microstructure of the coal particles for selected sizes before and after combustion are presented in Figures 3.40 - 3.43. From the images, it can be seen that the microstructure of the coal particles reveal a completely different picture in terms of the drastic changes that are evident as a result of combustion. It is clearly seen that the surface of the coal particles after combustion lacked many of the surface features and embedded smaller particles that were present before combustion. Also the surface of the coal particles after combustion is pockmarked with minute holes. These holes referred to as “blow holes” are caused as a result of rapid devolatilization of volatiles as the coal particles interact with the flame front. The rapid devolatilization process creates adequate internal pressure to rupture the surface of the coal particle thereby generating a blow hole. In addition to the formation of blow holes, some particles also showed signs of plastic deformation as result of combustion. These findings seem to be in good agreement with the observations made earlier by Hertzberg et al. [11]. The plastic deformation observed in certain cases has been theorized as the result of rapid heating of coal particles that cause them to pyrolyze, soften or melt into a plastic phase. The heavier products of pyrolysis are liquid that held together by surface tension forces causing them to assume a spherical shape. Other SEM images revealing some very interesting features about the morphology of coal particles as a result of combustion are presented in Figures 3.44 - 3.47. Also Figure 3.48 shows SEM images of cenospheres, a characteristic formation seen in coal combustion.

Since the macrostructure looks unaffected and the measured loose density does not change much, it is reasonable to conclude the combustion process of such entrained coal particles is a surface phenomenon. It looks like the generation of these “blow holes” takes a long time, much longer than the residence time in the flames. Hence, in order for a particle to volatize completely, enough time has to be provided for this process to be completed.

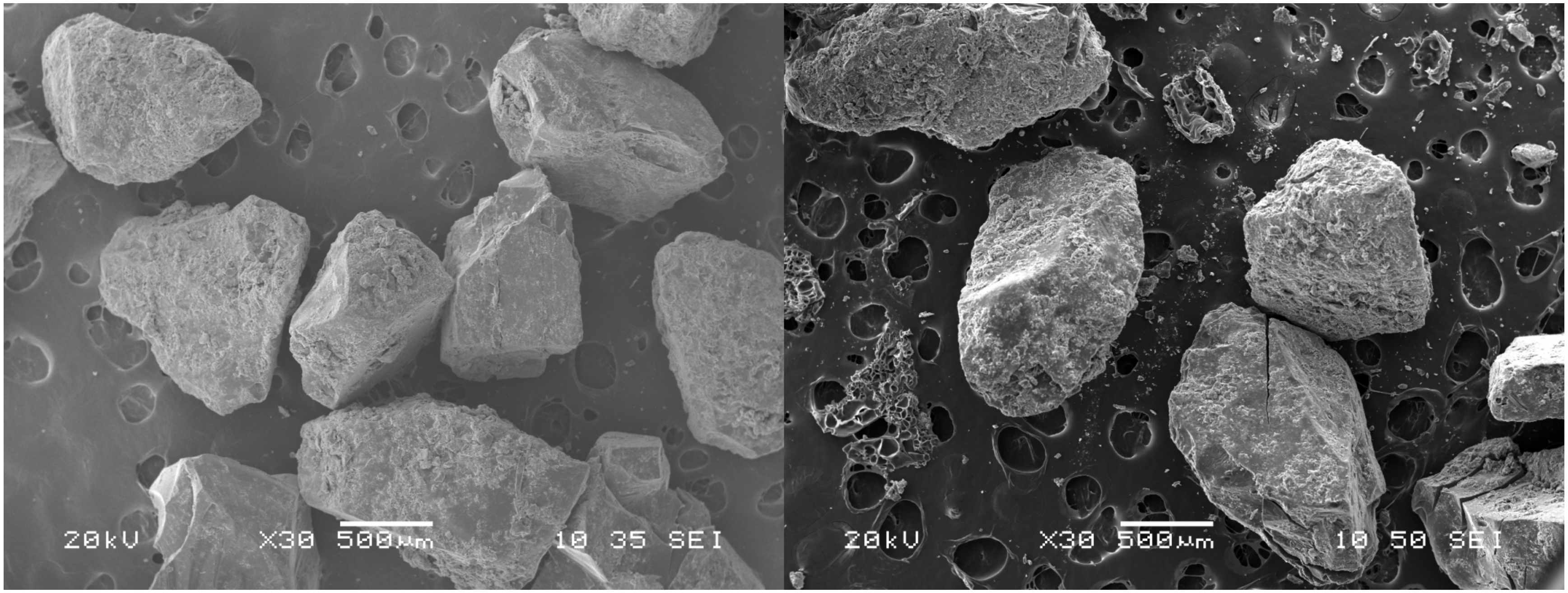

Figure 3.36: SEM photographs comparing the macrostructure of coal particles (Sieve size: 18-20) before (left) and after (right) combustion.

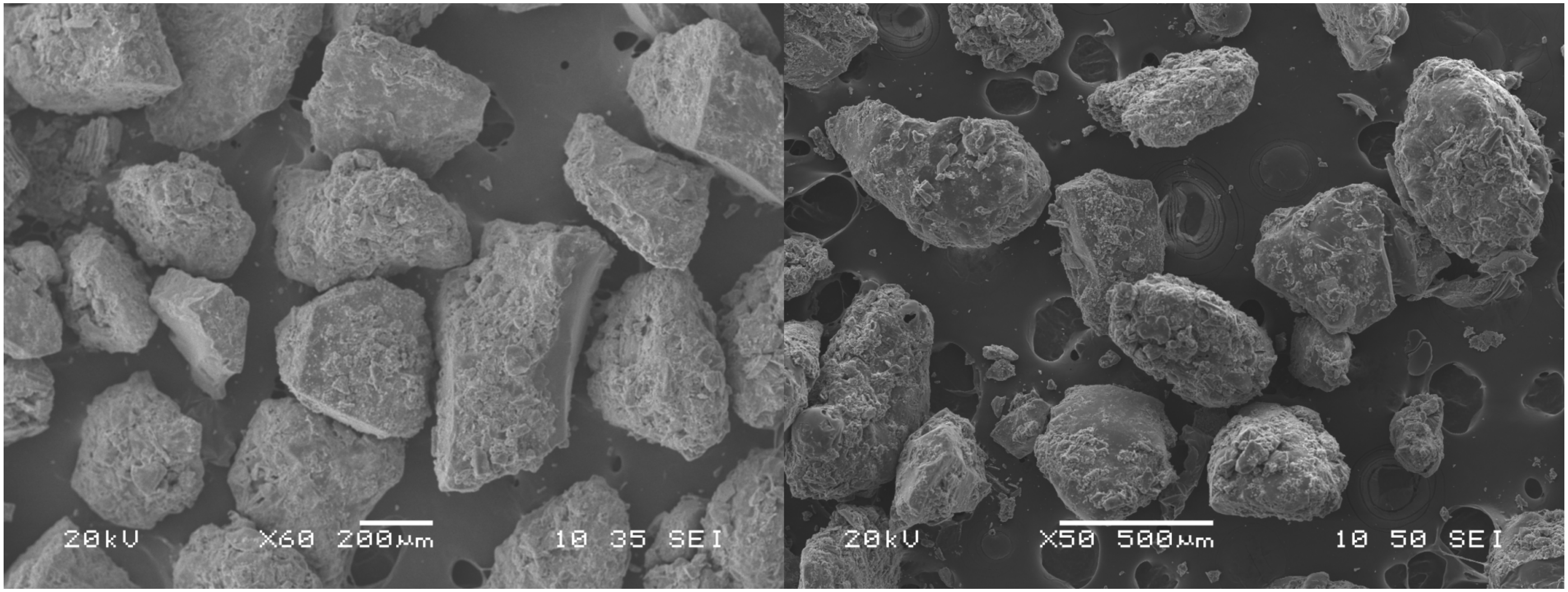

Figure 3.37: SEM photographs comparing the macrostructure of coal particles (Sieve size: 40-45) before (left) and after (right) combustion.

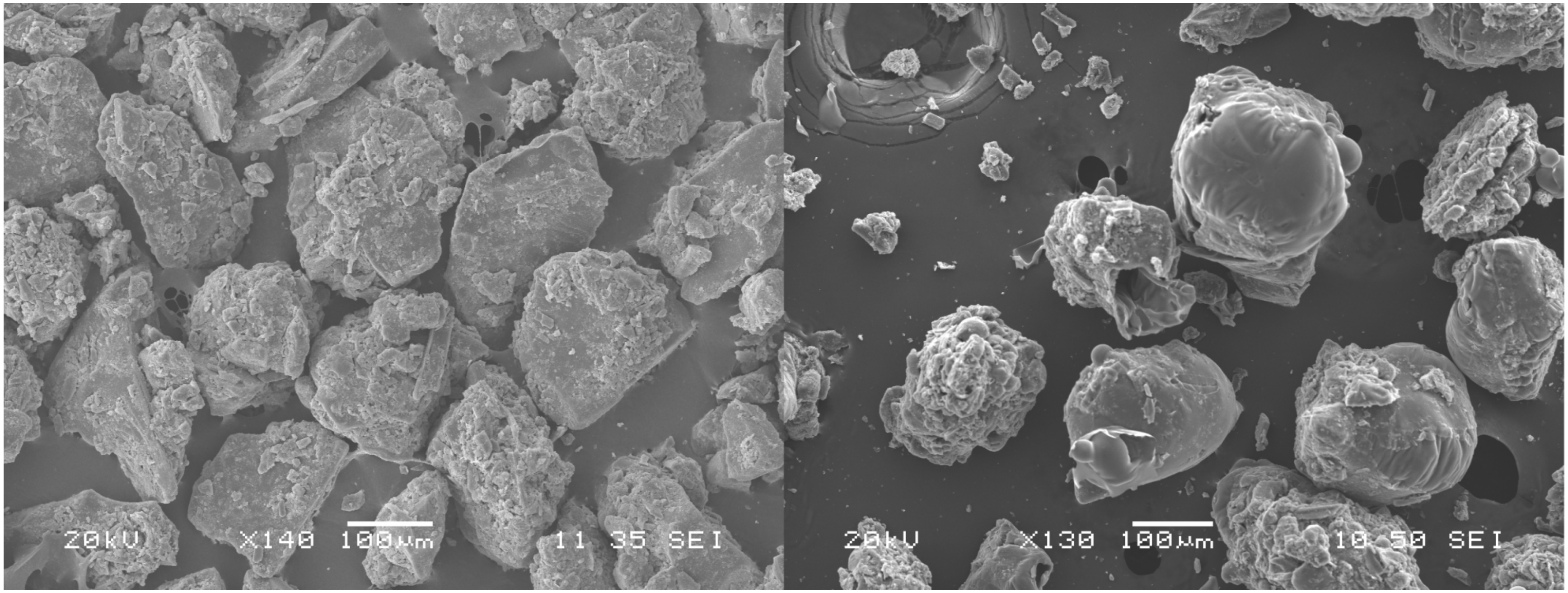

Figure 3.38: SEM photographs comparing the macrostructure of coal particles (Sieve size: 70-80) before (left) and after (right) combustion.

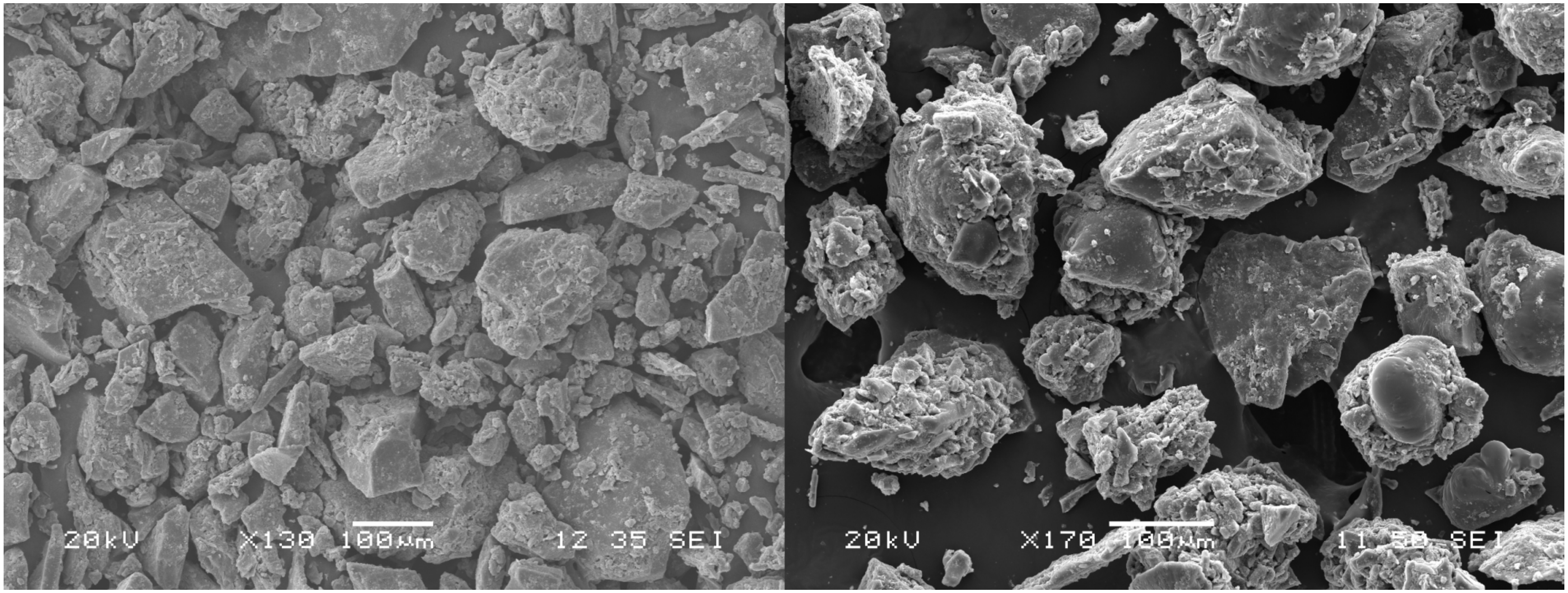

Figure 3.39: SEM photographs comparing the macrostructure of coal particles (Sieve size: < 80) before (left) and after (right) combustion.

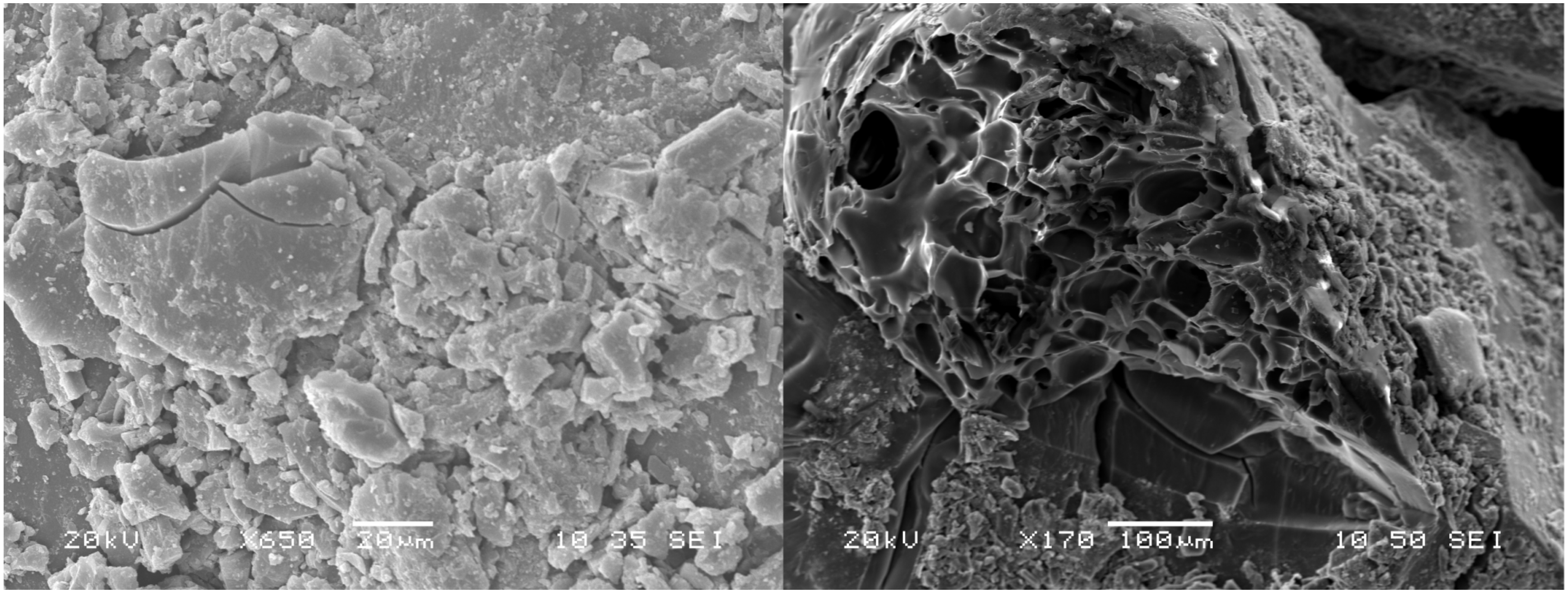

Figure 3.40: SEM photographs comparing the microstructure of coal particles (Sieve size: 18-20) before (left) and after (right) combustion.

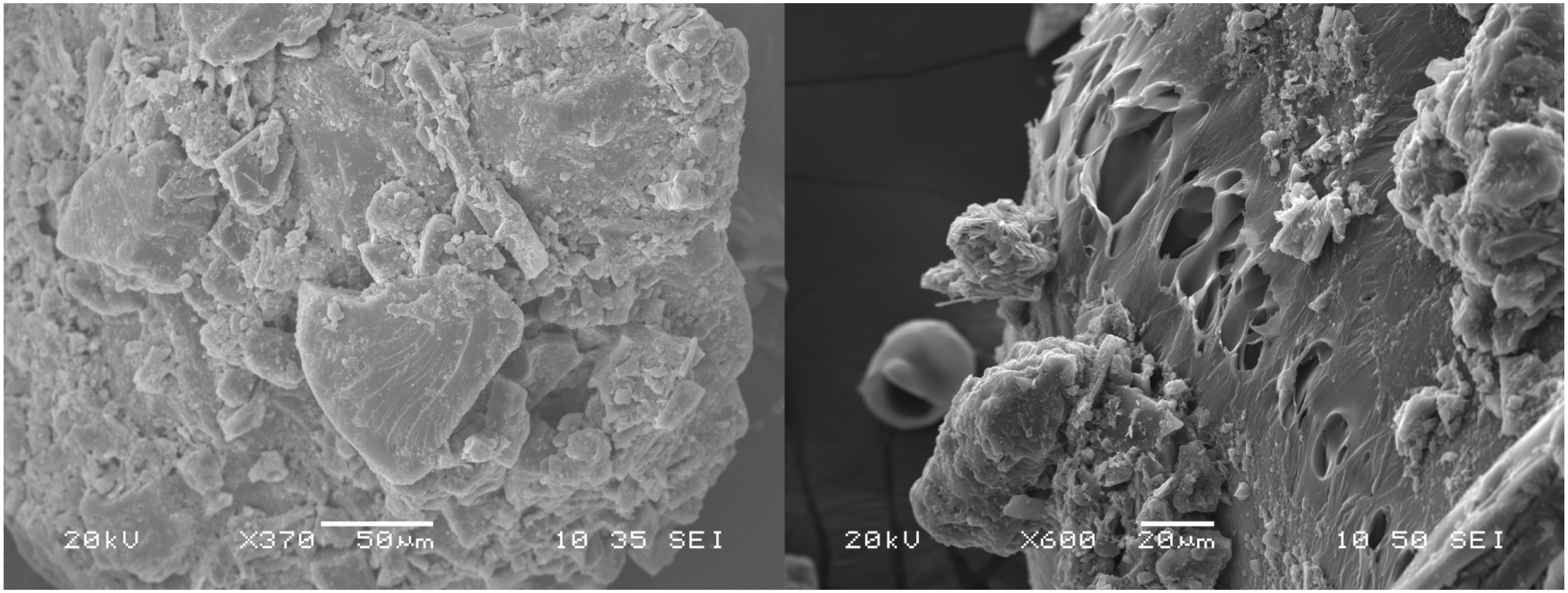

Figure 3.41: SEM photographs comparing the microstructure of coal particles (Sieve size: 40-45) before (left) and after (right) combustion.

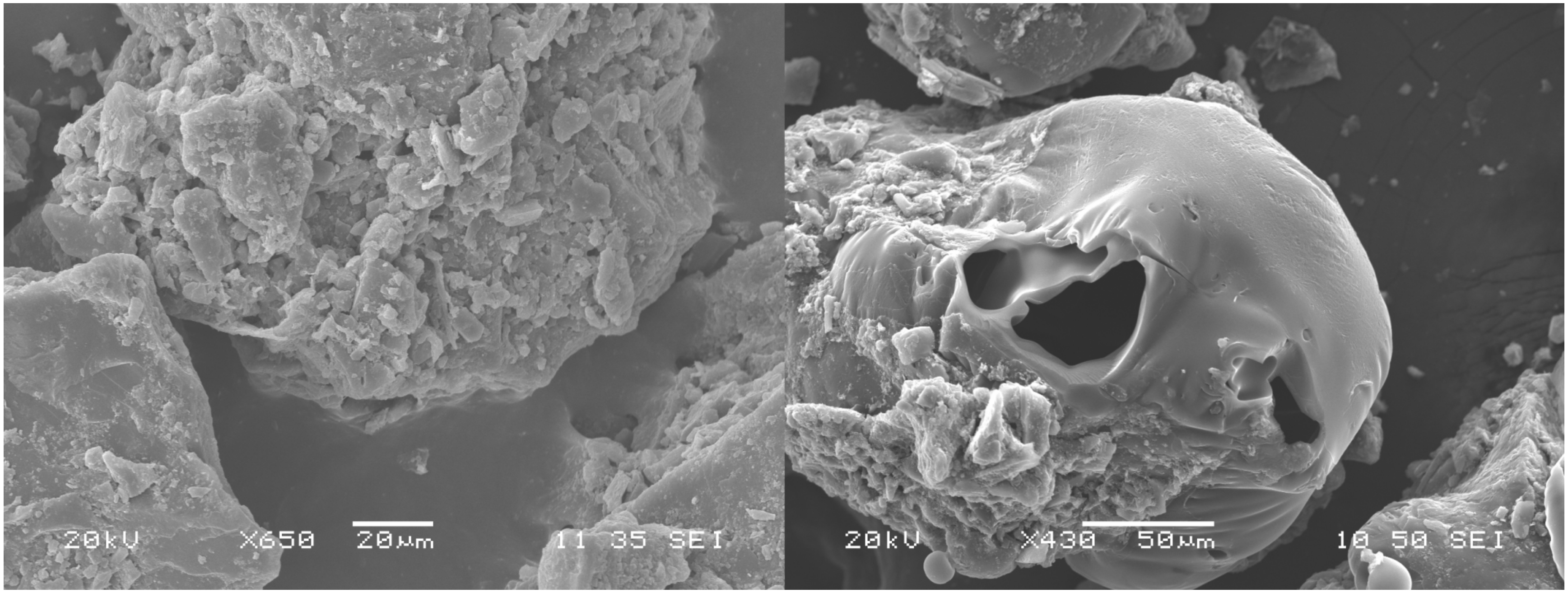

Figure 3.42: SEM photographs comparing the microstructure of coal particles (Sieve size: 70-80) before (left) and after (right) combustion.

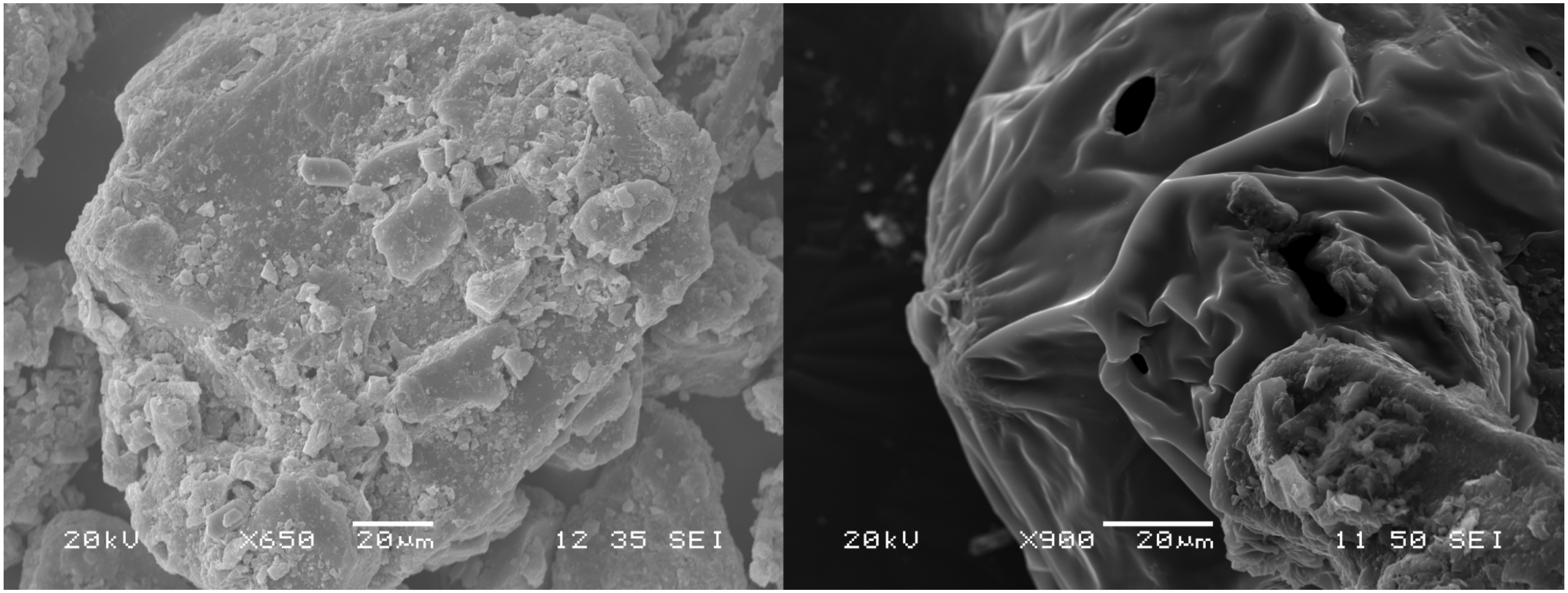

Figure 3.43: SEM photographs comparing the microstructure of coal particles (Sieve size: < 80) before (left) and after (right) combustion.

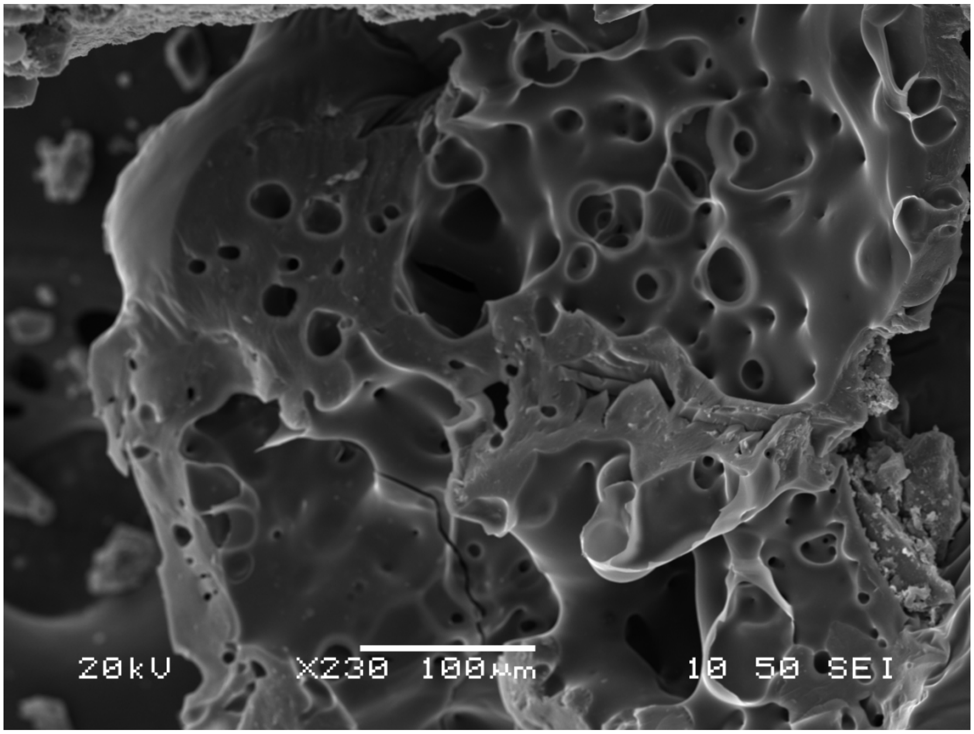

Figure 3.44: SEM photograph revealing a series of blow holes on the surface after combustion.

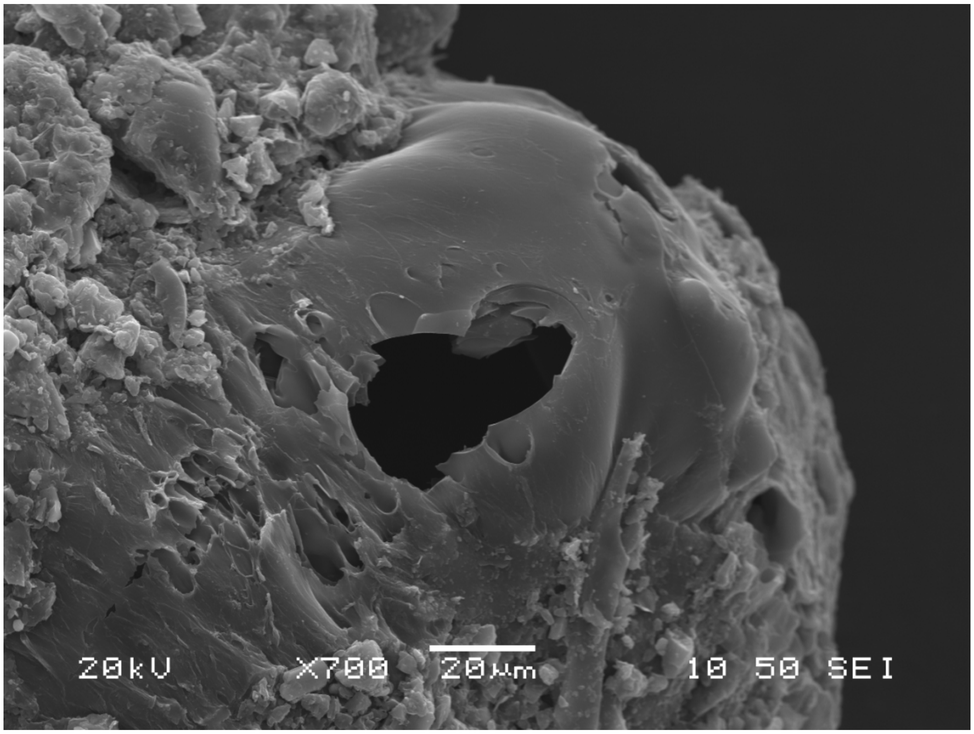

Figure 3.45: SEM photograph showing the collapse of a sintered surface after combustion.

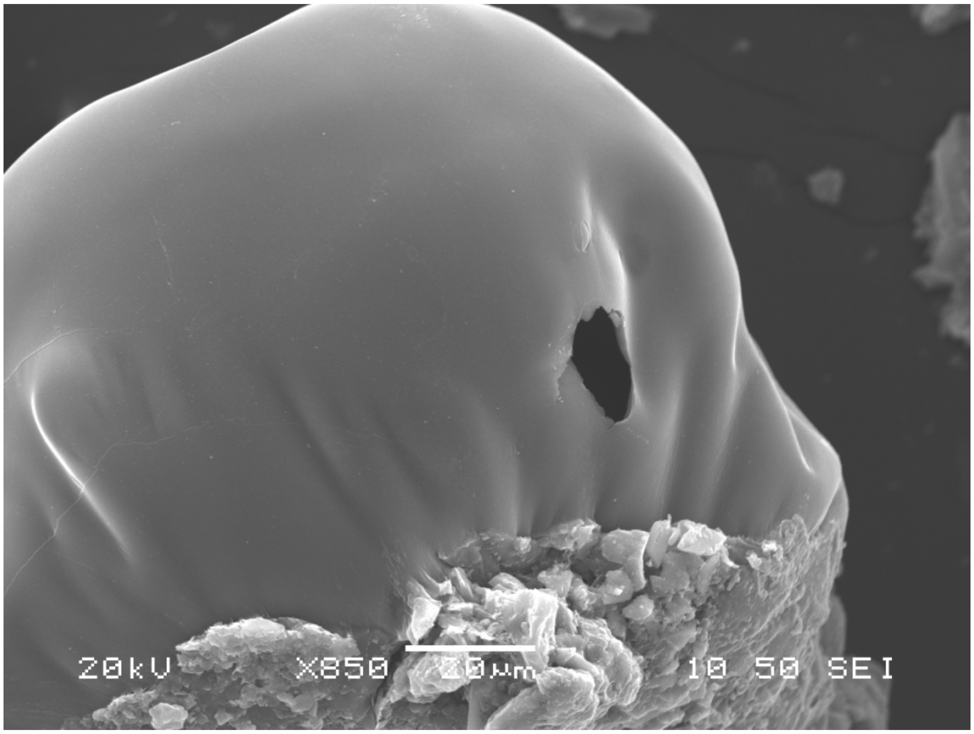

Figure 3.46: SEM photograph showing a blow hole on a completely sintered surface after combustion.

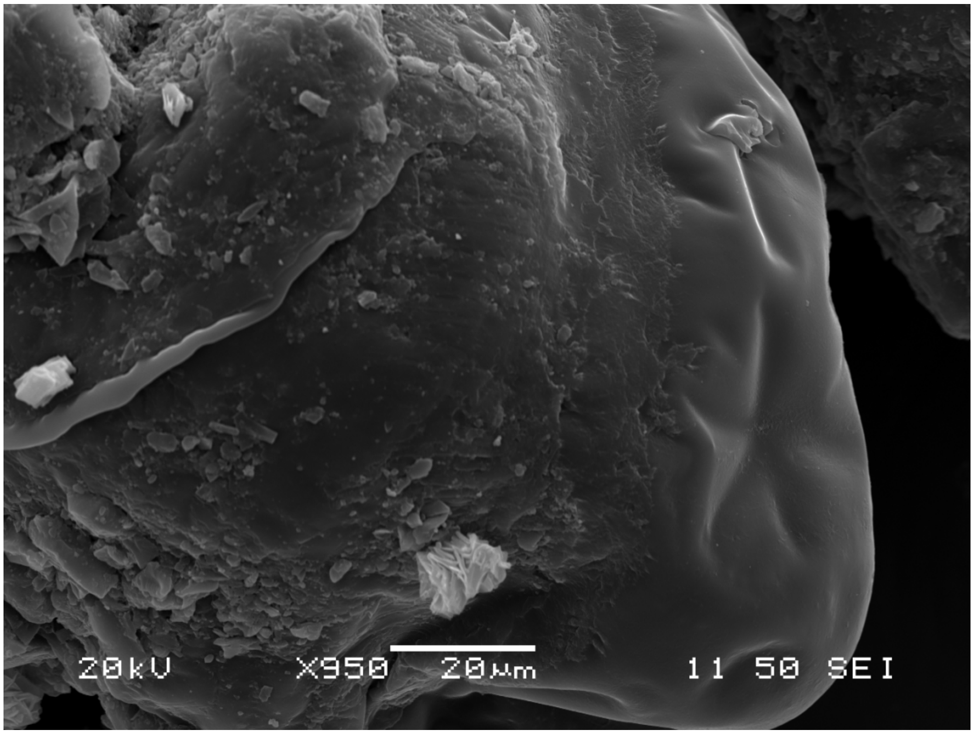

Figure 3.47: SEM photograph revealing the start of sintering process on the surface.

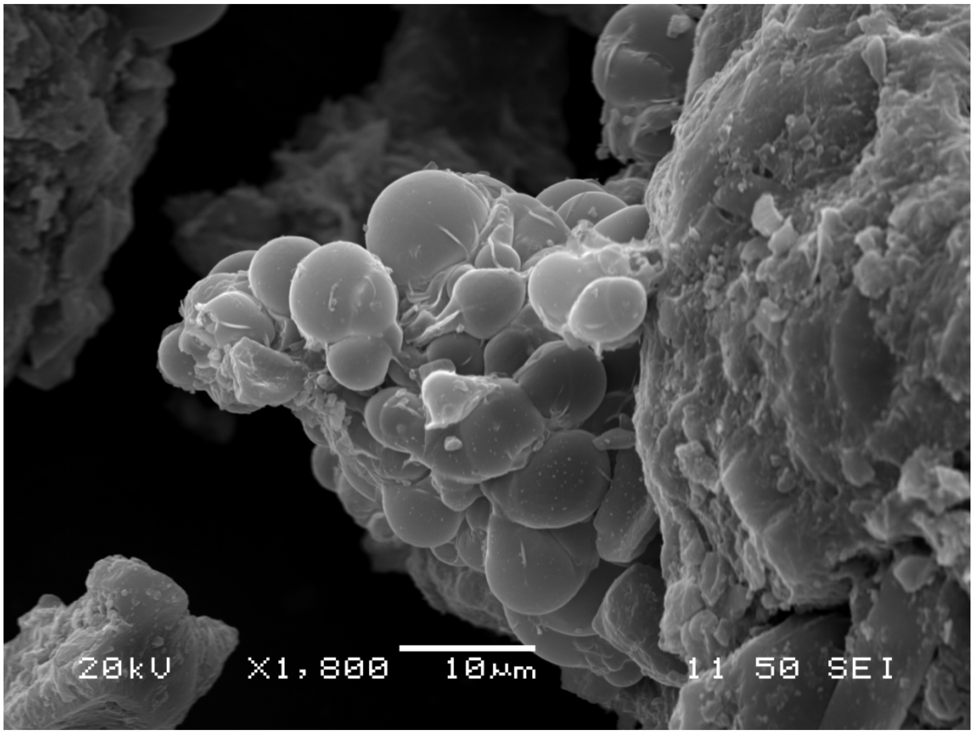

Figure 3.48: SEM photograph showing the formation of cenospheres as result of combustion.

CHAPTER 4

SUMMARY, CONCLUSIONS & RECOMMENDATIONS

4.1 Summary and Concluding Remarks

In this study, a vertically oriented solid particle injector capable of creating a coal-laden particle jet utilizing the Venturi effect was designed and fabricated. The injector used the pressure drop created due to air flow across an orifice plate fitted inside a circular tube to entrain pulverized coal particles. The entrainment rate for different sizes of coal samples was studied as a function of mass flow rate of air. It was found that the entrainment increased almost linearly with mass flow rate of air. Also for a fixed flow rate, the entrainment rate was found to decrease with increase in particle size. It was also observed that there is a minimum flow rate for each particle size below which there is no significant entrainment of particles. Particle Streak Velocimetry was performed on coal-laden jets by tracking the streaklines of individual particles using the ImageJ software of the National Institutes of Health. It was observed that due to the large Stokes number associated with these flows, the particles deviated substantially from the fluid flow field resulting in significant momentum transfer from the coal particles to the surrounding fluid.

The interaction of entrained coal particles with the flame front was studied. High-resolution still images and high-speed videos were taken in order to establish the combustion phenomenology. It was concluded that the trajectory of the coal particles was unaffected by the presence of the flame front. The coal particles shot through the flame front and punctured it; the extinction of the flame front was attributed to a combination of increased flame strain and heat loss to the solid coal particles. The coal particles began to sinter and continued to burn as they crossed the flame. Despite no change in trajectory, clear acceleration of coal particles was observed as they approached the flame front. This was due to the increase in velocity of the fluid; as the gases approached the flame front, the velocity of the gas had to increase in order to compensate for the decreasing gas density due to the increase in temperature.

The effect of combustion on the macrostructure of entrained coal particles was studied by analyzing the loose density and particle size distribution of coal particles before and after combustion using a CH_4 diffusion flame. It was observed that there was no significant change in the loose density of the coal particles after combustion and that the mean diameter of the particles remained unchanged during passage through the flame. This hypothesis was confirmed by the particle size distributions of the coal particles obtained before and after combustion using Malvern RT 97 Spraytec droplet-size measurement instrument. The Fraunhofer diffraction approximation was used to obtain the particle size distribution thereby circumventing the lack of knowledge of the refractive index of pulverized coal particles. The measurement unambiguously showed that the mean particle diameter of the particles was almost unaffected by the combustion process; however a clear decrease in the volume fraction of smaller and larger coal particles was observed. Also, in all these distributions, a slight increase in the volume fraction of mid-sized particles was observed. This was due to the decrease in diameter of larger particles and/or agglomeration of smaller particles as a result of combustion. It can be thus concluded that the coal particles undergo only partial devolatilization due to the small residence times within the flame (~ 0.01 s) as opposed to much larger time scales required for complete devolatilization (~ 0.1s). The effect of the nature of flame on the combustion of coal particles was also studied by analyzing the effect of premixed CH_4/air, $CH_4/O_2/CO_2$ and CH_4/O_2 flames on selected representative sizes of coal particles. It was found that the particle size distributions were qualitatively similar due to similar residence times in all these flames. However a slight decrease in the volume fraction for all particles, independent of size was observed in the premixed case especially in the CH_4/O_2 case when compared with the non-premixed case. This effect was more pronounced in the case of finer coal particles. This was due to the increased rate of burning of coal particles in the CH_4/O_2 case as a result of higher adiabatic flame temperature due to the lack of dilution.

Comparison of SEM images taken before and after combustion revealed a completely different picture in terms of microstructure of coal particles. The surface irregularities that were observed before combustion were entirely wiped out after combustion. In addition, the entire surface of the coal particles was seen to be pockmarked with “blow holes”, which were created as a result of release of volatile gases during the devolatilization of coal particles. The internal pressure generated during the combustion process caused the sintered surface of the coal particles to rupture leaving behind these characteristic surface features. Negligible change in terms of loose density and mean particle diameter coupled with SEM images proved that the combustion of such entrained coal particles is a surface phenomenon because of the small residence times in the flames, which did not allow for substantial volatilization throughout the particle volume.

4.2 Recommendations for Future Study

The present study was successful in extracting both qualitative results in terms of characterizing combustion morphology of entrained coal particles in jet flames and quantitative results in terms of particle size distribution before and after combustion. However, it is clear that as result of insufficient residence time within the flame, the coal particles underwent only partial devolatilization. Hence, it is necessary to investigate the possibility of designing a burner capable of increasing the residence times of these particles within the flame for durations sufficiently long enough to cause complete devolatilization and char burnout.

It was also evident that the effects of combustion were much more pronounced on finer coal particles as opposed to coarser ones. So studying the effect of combustion on much finer coal particles (tens of microns) is expected to provide more valuable insight on solid particle interaction with flames.

Also this study presented a new outlook into pulverized oxy-coal combustion technologies. The possibility of developing a practical burner capable of entraining coal particles and/or fluidized biomass for combustion would be essential for oxy-coal technology in the long run. This is a crucial factor in oxy-coal technology as the burner should be capable of delivering high concentration CO_2 ready for sequestration. Also, the prospects of designing a burner that would be capable of burning oxy-coal under pressure thereby improving not only the combustion efficiency but also the sequestration efficiency by delivering a steady stream of pressurized CO_2 gas is to be carried out. Such an oxy-coal burner design will be capable of drastically reducing the carbon footprint that is normally associated with coal combustion in existing conventional systems. The important finding of this thesis is that substantial residence times are needed for the volatilization of coal particles. This may be a challenge in the thin flames that are to be expected at high pressures.

LIST OF REFERENCES

[1] Intergovernmental Panel on Climate Change (IPCC): "Fourth Assessment Report - Climate Change", 2007 (AR4). Available at: http://www.ipcc.ch

[2] International Energy Agency (IEA): "World Energy Outlook", 2004. Available at: http://www.iea.org

[3] World Energy Council (WEC): "Sustainable Global Energy Development: The Case for Coal", 2004. Available at: http:// www.worldenergy.org

[4] B.J.P. Buhre, L.K. Elliott, C.D. Sheng, R.P. Gupta, and T.F. Wall. "Oxy-fuel combustion technology for coal-fired power generation". Progress in Energy and Combustion Science, vol. 31, pp. 283-307, 2005.

[5] A. Williams, M. Pourkashanian, and J.M. Jones. "Combustion of Pulverized coal and Biomass". Progress in Energy and Combustion Science, vol. 27, pp. 587-610, 2001.

[6] R. Sampath, D.J. Maloney, and J.W. Zondlo. "Evaluation of Thermo physical and Thermochemical Heat Requirements for Coals at Combustion Level Heat Fluxes". Proceedings of the Combustion Institute, vol.2, pp. 2915-2924, 1998.

[7] J.R. Gibbins, J. Zhang, H. Afzal, G. Riley, and T. Beeley. Editors: B.Q. Li and Z.Y. Liu "Prospects for coal science in the 21st century". Proceedings of the 10th International Conference on Coal Science, Taiyuan: Shanxi Science and Technology Press, vol. 1, pp. 459-462, 1999.

[8] N.V. Russel, T.J. Beeley, C.K. Man, J.R. Gibbins, and J. Wialliamson. "Development of TG measurements of intrinsic char combustion reactivity for industrial and research purposes". Fuel Processing Technology, vol. 57, pp. 113-130, 1998.

[9] Kenneth L. Cashdollar. "Coal Dust Explosibility". Journal of Loss Prevention in the Process Industries, vol. 9, no.1, pp. 65-76, 1996.

[10] Paul R. Amyotte, Kenneth J. Mintz, Michael J. Pegg, and Yu Hong Sun. “The ignitability of coal dust-air and methane-coal dust-air mixtures”. Fuel, vol. 72, no.5, pp. 671-679, 1993.

[11] Martin Hertzberg, Kenneth L. Cashdollar, Daniel L. NG, and Ronald S. Conti. “Domains of Flammability and Thermal Ignitability for pulverized coals and other dusts: Particle size dependences and microscopic residue analyses”. Proceedings of the Combustion Institute, vol.1, pp. 1169-1180, 1982.

[12] R.A. Ogle, J.K Beddow, and A.F. Vetter. “A Thermal Theory of Laminar Premixed Dust Flame Propagation”. Combustion and Flame, vol. 58, pp. 77-79, 1984.

[13] I. Glassman. “Combustion”. Academic Press, New York, pp. 66-68, 1977.

[14] H.M. Cassel, A.K. Das Gupta, and S. Guruswamy. “Factors affecting Flame propagation through Dust Clouds”. The 3rd Symposium on Combustion, Flames, and Explosion Processes, pp. 185-190, 1949.

[15] M.D. Horton, F.P. Goodson, and L.D. Smoot. “Characteristics of Flat, Laminar Coal-Dust Flames”. Combustion and Flame, vol. 28, pp. 187-195, 1977.

[16] Scoot E. Slezak, Dennis J. Fitch, Herman Krier, and Richard O. Buckius. “Coal Dust Flame Propagation in a Laboratory Flammability Tube”. Combustion and Flame, vol. 54, pp. 103-119, 1983.

[17] Yi Liu, Jinhua Sun, and Dongliang Chen. “Flame propagation in hybrid mixture of coal dust and methane”. Journal of Loss Prevention in the Process Industries, vol. 20, pp. 691-697, 2007.

[18] Clayton T. Crowe, John D. Schwarzkopf, Martin Sommerfeld, and Yutaka Tsuji. “Multiphase Flows with Droplets and Particles”. 2nd Edition, Taylor and Francis Group LLC, pp. 243-249, 2012.

[19] S.K. Friedlander. “Smoke, Dust, and Haze: Fundamentals of Aerosol Dynamics”. 2nd Edition, Oxford University Press, New York, 2000.

[20] U. Wagenknecht and M. Bohnet “Aerodynamic studies of gas/solid-injectors”. Chemical Engineering and Technology, vol. 50, no.2, pp. 298, 1978.

[21] YanxuanXie, Vasudevan Raghavan, and Ali S. Rangwala. “Naturally Entraining Solid Particle Injector”. Powder Technology, 2011.

[22] Yanxuan Xie, Vasudevan Raghavan, and Ali S. Rangwala. “Study of interaction of entrained coal dust particles in lean methane-air premixed flames”. Combustion and Flame, vol. 159, pp. 2449-2456, 2012.

[23] B.M. Franchetti, F. Cavallo Marincola, S. Navarro-Martinez, and A.M. Kempf. “Large Eddy simulation of a pulverized coal jet flame”. Proceedings of the Combustion Institute, vol. 34, pp. 2419-2426, 2013.

[24] Scott R. Rockwell, and Ali S. Rangwala. “Influence of coal dust on premixed turbulent methane-air flames”. Combustion and Flame, vol. 160, pp. 635-640, 2013.

[25] D. Singh, E. Croiset, P.L. Douglas, and M.A. Douglas. “Techno-economic study of CO_2 capture from an existing coal-fired power plant: MEA scrubbing vs. O_2/CO_2 recycle combustion”. Energy Conversion and Management, vol. 44, pp. 3073-3091, 2003.

[26] T.F. Wall, R.P. Gupta, B.J.P. Buhre, and S. Khare. “Oxy-fuel (O_2/CO_2, O_2/RFG) technology for sequestration-ready CO_2 and emission compliance”. The Clearwater Coal Conference: The 30th international technical conference on coal utilization & fuel systems, Coal technology: yesterday - today - tomorrow, Clearwater, USA, April 17-21, 2005.

[27] Gunter Scheffknecht, Leema Al-Makhadmeh1, Uwe Schnell, and Jorg Maier. “Oxy-fuel coal combustion - A review of the current state-of-the-art”. International Journal of Greenhouse Gas Control, vol. 5S, pp. S16-S35, 2011.

[28] K.J. McCauley, S.A. Moorman, and D.K. McDonald. "Oxy-Coal Combustion for Low Carbon Electric Power Generation". The 5th International Conference on Clean Coal Technologies, May 8-12, 2011, Zaragoza, Spain.

[29] T.F. Wall, and J. Yu. "Coal-fired oxyfuel technology status and progress to deployment". The 34th International Conference on Coal Utilization and Fuel Systems, Clearwater, USA, 2009.

[30] Malvern, "Using Mie theory and the Fraunhofer approximation". Available at: http://www.malvern.com/labeng/technology/laser_diffraction/mie_theory_fraunhofer.htm

[31] G. Gouesbet, G. Grehan, and B. Maheu. "Single scattering characteristics of volume elements in coal clouds". Applied Optics, vol. 22, no. 13, pp. 2038-2051, 1983.

[32] S. Manickavasagam and M.P. Menguc. "Effective Optical Properties of Pulverized Coal Particles Determined from FT-IR Spectrometer Experiments". Energy and Fuels, vol. 7, pp. 860-869, 1993.

[33] David Pui-Yin Tse. "Experimental Investigation of the flow field during Combustion in Narrow Circular Ducts". MS Thesis, Department of Mechanical Science and Engineering, University of Illinois at Urbana-Champaign, 2012.

[34] I.W. Smith. "The combustion rates of coal chars: A review". Proceedings of the Combustion Institute, vol.1, pp. 1045-1065, 1982.

[35] Omega, "Variable Area Flow meters: Flow reference section". Available at: http://www.omega.com/Green/pdf/TECHREF_SECT_B.pdf

[36] H.C. Van de Hulst. "Light scattering by small particles". 1st Edition, Dover Publications Inc., New York, 1981.

[37] R.K. Avery and A.R Jones. "Measurement of the complex refractive index of pulverized coal by light scattering: an attempt and some comments". Journal of Physics D: Applied Physics, vol. 15, 1373-1384, 1982.

APPENDIX A

ROTAMETER CALIBRATION

A.1 Omega FL-3839 ST

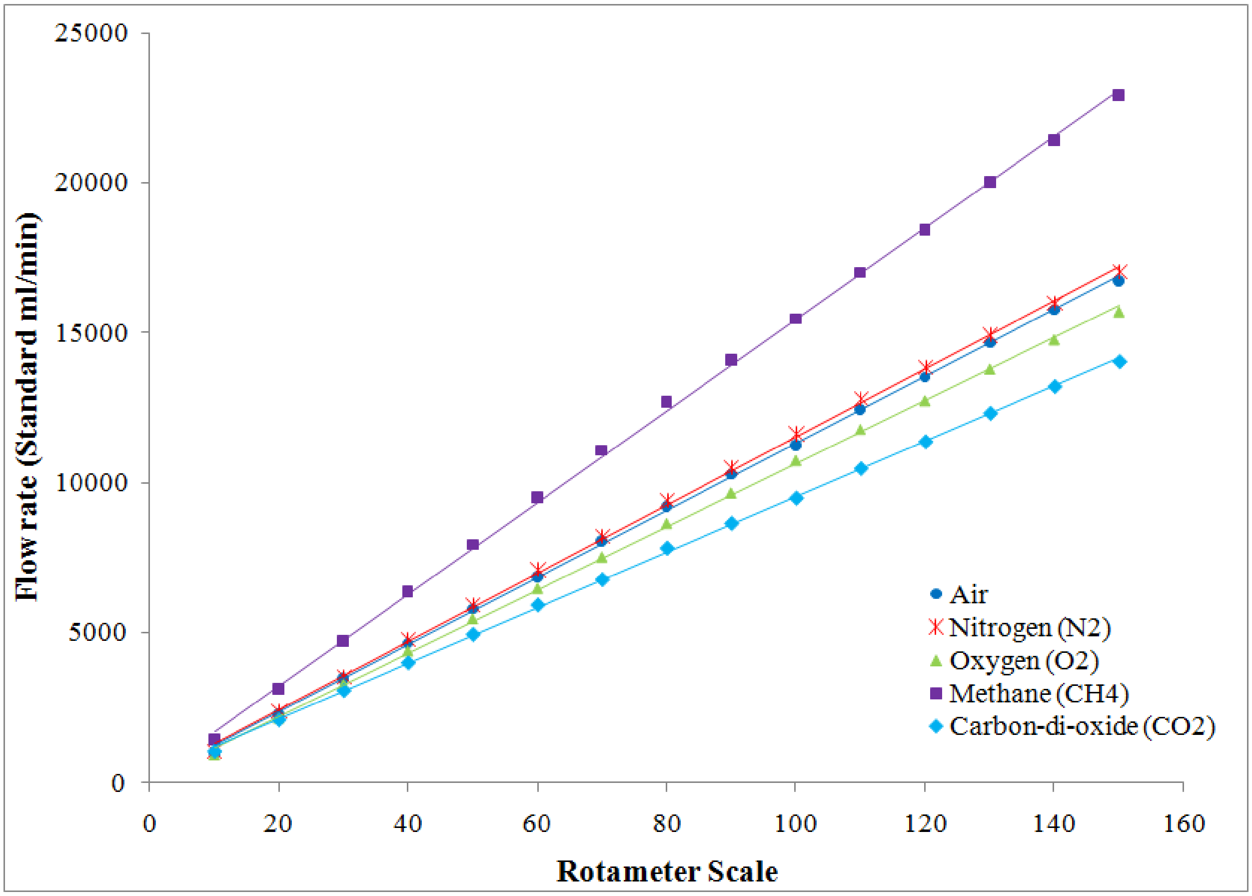

Figure A.1: Calibration curves for Omega FL-3839 ST rotameter.

A.2 Omega FL-3840 G

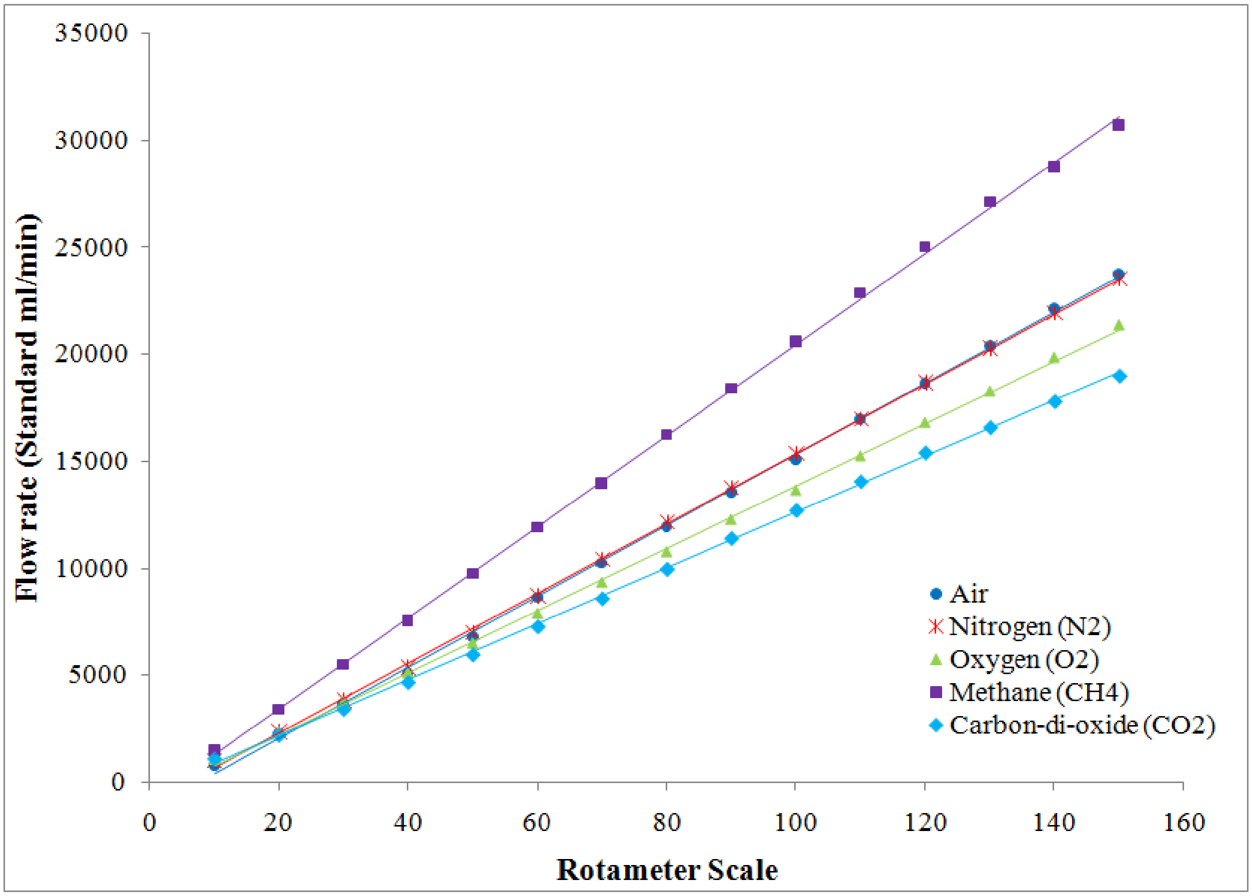

Figure A.2: Calibration curves for Omega FL-3840 G rotameter.

APPENDIX B

PERSPECTIVE VIEW AT 45° TO LASER SHEET

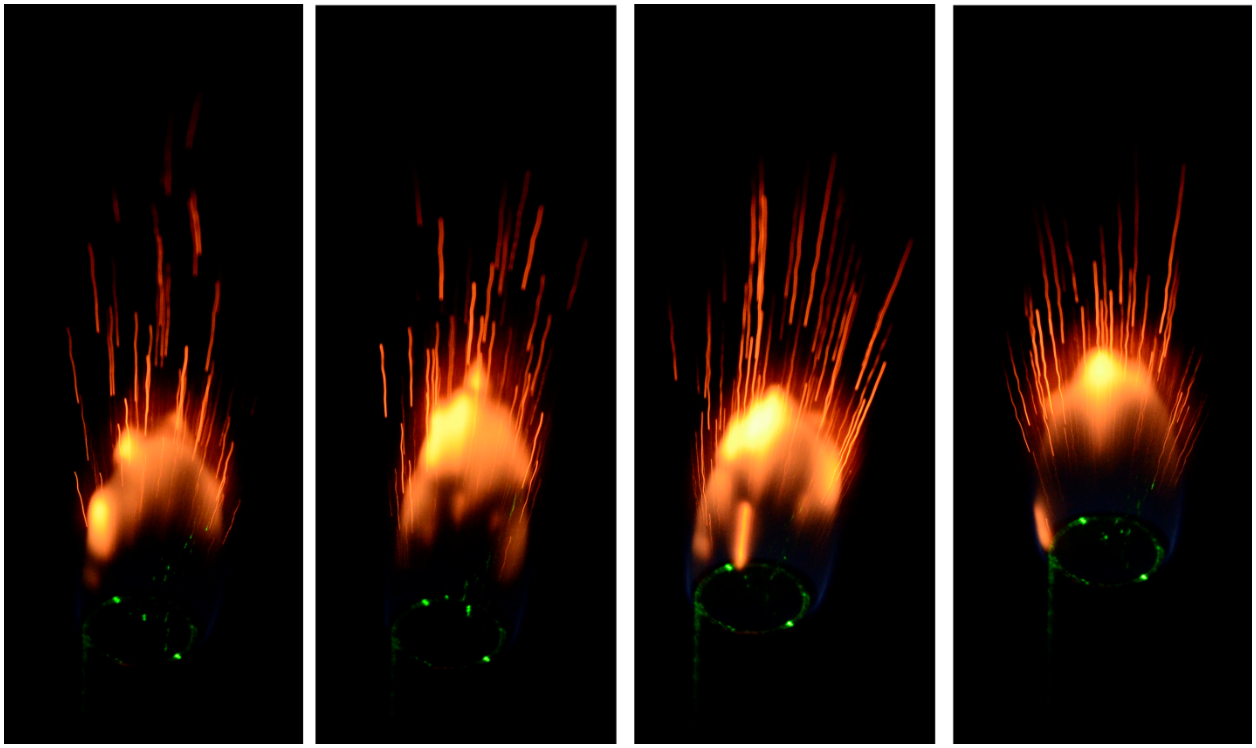

Figure B.1: Coal particles shooting through the flame front.
(Captured at a 45° angle to the laser sheet).

Figure B.2: Coal particles interacting with the flame front.

(Captured at a 45° angle to the laser sheet).

APPENDIX C

PARTICLE SIZE DATA

C.1 Malvern Bin Size

Upper diameter (μm)	**Lower diameter (μm)**	**Average diameter (μm)**	**Upper diameter (μm)**	**Lower diameter (μm)**	**Average diameter (μm)**
0.1166	0.1000	0.1083	11.6591	10.0000	10.8296
0.1359	0.1166	0.1263	13.5936	11.6591	12.6264
0.1585	0.1359	0.1472	15.8489	13.5936	14.7213
0.1848	0.1585	0.1717	18.4785	15.8489	17.1637
0.2154	0.1848	0.2001	21.5443	18.4785	20.0114
0.2512	0.2154	0.2333	25.1189	21.5443	23.3316
0.2929	0.2512	0.2721	29.2864	25.1189	27.2027
0.3415	0.2929	0.3172	34.1455	29.2864	31.7160
0.3981	0.3415	0.3698	39.8107	34.1455	36.9781
0.4642	0.3981	0.4312	46.4159	39.8107	43.1133
0.5412	0.4642	0.5027	54.1170	46.4159	50.2665
0.6310	0.5412	0.5861	63.0957	54.1170	58.6064
0.7356	0.6310	0.6833	73.5642	63.0957	68.3300
0.8577	0.7356	0.7967	85.7696	73.5642	79.6669
1.0000	0.8577	0.9289	100.0000	85.7696	92.8848
1.1659	1.0000	1.0830	116.5914	100.0000	108.2957
1.3594	1.1659	1.2627	135.9356	116.5914	126.2635
1.5849	1.3594	1.4722	158.4893	135.9356	147.2125
1.8478	1.5849	1.7164	184.7850	158.4893	171.6372
2.1544	1.8478	2.0011	215.4435	184.7850	200.1143
2.5119	2.1544	2.3332	251.1886	215.4435	233.3161
2.9286	2.5119	2.7203	292.8645	251.1886	272.0266
3.4145	2.9286	3.1716	341.4549	292.8645	317.1597
3.9811	3.4145	3.6978	398.1072	341.4549	369.7811
4.6416	3.9811	4.3114	464.1589	398.1072	431.1331
5.4117	4.6416	5.0267	541.1695	464.1589	502.6642
6.3096	5.4117	5.8607	630.9573	541.1695	586.0634
7.3564	6.3096	6.8330	735.6423	630.9573	683.2998
8.5770	7.3564	7.9667	857.6959	735.6423	796.6691
10.0000	8.5770	9.2885	1000.0000	857.6959	928.8480

Table C.1: Average diameter based on upper and lower diameter limits of bin sizes provided by RT Sizer software.

C.2 Particle Size Distribution before Combustion

Average diameter (µm)	Volume (%)	Standard Deviation (%)	Average diameter (µm)	Volume (%)	Standard Deviation (%)
0.1083	0.00	0.00	10.8296	0.00	0.00
0.1263	0.00	0.00	12.6264	0.00	0.00
0.1472	0.00	0.00	14.7213	0.00	0.00
0.1717	0.00	0.00	17.1637	0.00	0.00
0.2001	0.00	0.00	20.0114	0.00	0.00
0.2333	0.00	0.00	23.3316	0.00	0.00
0.2721	0.00	0.00	27.2027	0.00	0.00
0.3172	0.00	0.00	31.7160	0.00	0.00
0.3698	0.00	0.00	36.9781	0.01	0.01
0.4312	0.00	0.00	43.1133	0.01	0.01
0.5027	0.00	0.00	50.2665	0.01	0.01
0.5861	0.00	0.00	58.6064	0.01	0.01
0.6833	0.00	0.00	68.3300	0.01	0.01
0.7967	0.00	0.00	79.6669	0.02	0.01
0.9289	0.00	0.00	92.8848	0.03	0.02
1.0830	0.00	0.00	108.2957	0.05	0.03
1.2627	0.00	0.00	126.2635	0.07	0.05
1.4722	0.00	0.00	147.2125	0.08	0.10
1.7164	0.00	0.00	171.6372	0.12	0.19
2.0011	0.00	0.00	200.1143	0.20	0.34
2.3332	0.00	0.00	233.3161	0.37	0.50
2.7203	0.00	0.00	272.0266	0.71	0.64
3.1716	0.00	0.00	317.1597	1.33	0.73
3.6978	0.00	0.00	369.7811	2.43	0.93
4.3114	0.00	0.00	431.1331	4.42	1.53
5.0267	0.00	0.00	502.6642	8.41	2.77
5.8607	0.00	0.00	586.0634	17.44	3.16
6.8330	0.00	0.00	683.2998	30.72	2.97
7.9667	0.00	0.00	796.6691	27.83	6.51
9.2885	0.00	0.00	928.8480	5.72	1.54

Table C.2: Particle size distribution of coal particles before combustion (Sieve size: 18-20).

Average diameter (µm)	Volume (%)	Standard Deviation (%)	Average diameter (µm)	Volume (%)	Standard Deviation (%)
0.1083	0.00	0.00	10.8296	0.00	0.00
0.1263	0.00	0.00	12.6264	0.00	0.00
0.1472	0.00	0.00	14.7213	0.00	0.00
0.1717	0.00	0.00	17.1637	0.00	0.00
0.2001	0.00	0.00	20.0114	0.00	0.00
0.2333	0.00	0.00	23.3316	0.00	0.00
0.2721	0.00	0.00	27.2027	0.00	0.00
0.3172	0.00	0.00	31.7160	0.00	0.00
0.3698	0.00	0.00	36.9781	0.00	0.00
0.4312	0.00	0.00	43.1133	0.00	0.01
0.5027	0.00	0.00	50.2665	0.00	0.02
0.5861	0.00	0.00	58.6064	0.00	0.02
0.6833	0.00	0.00	68.3300	0.00	0.03
0.7967	0.00	0.00	79.6669	0.00	0.04
0.9289	0.00	0.00	92.8848	0.01	0.06
1.0830	0.00	0.00	108.2957	0.02	0.09
1.2627	0.00	0.00	126.2635	0.03	0.14
1.4722	0.00	0.00	147.2125	0.06	0.19
1.7164	0.00	0.00	171.6372	0.11	0.24
2.0011	0.00	0.00	200.1143	0.20	0.27
2.3332	0.00	0.00	233.3161	0.37	0.29
2.7203	0.00	0.00	272.0266	0.71	0.29
3.1716	0.00	0.00	317.1597	1.33	0.32
3.6978	0.00	0.00	369.7811	2.71	0.44
4.3114	0.00	0.00	431.1331	6.43	0.66
5.0267	0.00	0.00	502.6642	15.46	1.16
5.8607	0.00	0.00	586.0634	29.06	1.64
6.8330	0.00	0.00	683.2998	29.72	2.02
7.9667	0.00	0.00	796.6691	12.18	1.63
9.2885	0.00	0.00	928.8480	1.62	0.24

Table C.3: Particle size distribution of coal particles before combustion (Sieve size: 20-25).

Average diameter (µm)	**Volume (%)**	**Standard Deviation (%)**	**Average diameter (µm)**	**Volume (%)**	**Standard Deviation (%)**
0.1083	0.00	0.00	10.8296	0.00	0.00
0.1263	0.00	0.00	12.6264	0.00	0.00
0.1472	0.00	0.00	14.7213	0.00	0.00
0.1717	0.00	0.00	17.1637	0.00	0.00
0.2001	0.00	0.00	20.0114	0.00	0.00
0.2333	0.00	0.00	23.3316	0.00	0.00
0.2721	0.00	0.00	27.2027	0.00	0.00
0.3172	0.00	0.00	31.7160	0.00	0.00
0.3698	0.00	0.00	36.9781	0.00	0.01
0.4312	0.00	0.00	43.1133	0.01	0.01
0.5027	0.00	0.00	50.2665	0.01	0.02
0.5861	0.00	0.00	58.6064	0.02	0.02
0.6833	0.00	0.00	68.3300	0.02	0.02
0.7967	0.00	0.00	79.6669	0.03	0.02
0.9289	0.00	0.00	92.8848	0.04	0.03
1.0830	0.00	0.00	108.2957	0.07	0.06
1.2627	0.00	0.00	126.2635	0.14	0.11
1.4722	0.00	0.00	147.2125	0.27	0.20
1.7164	0.00	0.00	171.6372	0.47	0.33
2.0011	0.00	0.00	200.1143	0.74	0.48
2.3332	0.00	0.00	233.3161	1.07	0.64
2.7203	0.00	0.00	272.0266	1.53	0.82
3.1716	0.00	0.00	317.1597	2.45	1.17
3.6978	0.00	0.00	369.7811	4.84	1.86
4.3114	0.00	0.00	431.1331	11.35	2.21
5.0267	0.00	0.00	502.6642	23.65	2.44
5.8607	0.00	0.00	586.0634	30.08	5.29
6.8330	0.00	0.00	683.2998	17.88	1.67
7.9667	0.00	0.00	796.6691	4.73	0.77
9.2885	0.00	0.00	928.8480	0.57	0.14

Table C.4: Particle size distribution of coal particles before combustion (Sieve size: 25-30).

Average diameter (μm)	**Volume (%)**	**Standard Deviation (%)**	**Average diameter (μm)**	**Volume (%)**	**Standard Deviation (%)**
0.1083	0.00	0.00	10.8296	0.00	0.00
0.1263	0.00	0.00	12.6264	0.00	0.00
0.1472	0.00	0.00	14.7213	0.00	0.00
0.1717	0.00	0.00	17.1637	0.00	0.00
0.2001	0.00	0.00	20.0114	0.00	0.00
0.2333	0.00	0.00	23.3316	0.00	0.00
0.2721	0.00	0.00	27.2027	0.00	0.00
0.3172	0.00	0.00	31.7160	0.00	0.00
0.3698	0.00	0.00	36.9781	0.00	0.00
0.4312	0.00	0.00	43.1133	0.00	0.00
0.5027	0.00	0.00	50.2665	0.01	0.01
0.5861	0.00	0.00	58.6064	0.01	0.02
0.6833	0.00	0.00	68.3300	0.03	0.03
0.7967	0.00	0.00	79.6669	0.04	0.05
0.9289	0.00	0.00	92.8848	0.07	0.08
1.0830	0.00	0.00	108.2957	0.11	0.13
1.2627	0.00	0.00	126.2635	0.19	0.20
1.4722	0.00	0.00	147.2125	0.30	0.30
1.7164	0.00	0.00	171.6372	0.45	0.39
2.0011	0.00	0.00	200.1143	0.63	0.43
2.3332	0.00	0.00	233.3161	0.93	0.48
2.7203	0.00	0.00	272.0266	1.53	0.58
3.1716	0.00	0.00	317.1597	3.23	0.83
3.6978	0.00	0.00	369.7811	8.34	1.13
4.3114	0.00	0.00	431.1331	21.08	0.56
5.0267	0.00	0.00	502.6642	32.26	2.98
5.8607	0.00	0.00	586.0634	22.15	1.73
6.8330	0.00	0.00	683.2998	7.22	0.71
7.9667	0.00	0.00	796.6691	1.29	0.32
9.2885	0.00	0.00	928.8480	0.13	0.07

Table C.5: Particle size distribution of coal particles before combustion (Sieve size: 30-35).

Average diameter (µm)	**Volume (%)**	**Standard Deviation (%)**	**Average diameter (µm)**	**Volume (%)**	**Standard Deviation (%)**
0.1083	0.00	0.00	10.8296	0.00	0.00
0.1263	0.00	0.00	12.6264	0.00	0.00
0.1472	0.00	0.00	14.7213	0.00	0.00
0.1717	0.00	0.00	17.1637	0.00	0.00
0.2001	0.00	0.00	20.0114	0.00	0.00
0.2333	0.00	0.00	23.3316	0.00	0.00
0.2721	0.00	0.00	27.2027	0.00	0.00
0.3172	0.00	0.00	31.7160	0.00	0.00
0.3698	0.00	0.00	36.9781	0.00	0.00
0.4312	0.00	0.00	43.1133	0.01	0.00
0.5027	0.00	0.00	50.2665	0.02	0.01
0.5861	0.00	0.00	58.6064	0.05	0.04
0.6833	0.00	0.00	68.3300	0.08	0.07
0.7967	0.00	0.00	79.6669	0.14	0.11
0.9289	0.00	0.00	92.8848	0.22	0.15
1.0830	0.00	0.00	108.2957	0.33	0.20
1.2627	0.00	0.00	126.2635	0.52	0.29
1.4722	0.00	0.00	147.2125	0.75	0.41
1.7164	0.00	0.00	171.6372	0.98	0.51
2.0011	0.00	0.00	200.1143	1.23	0.56
2.3332	0.00	0.00	233.3161	1.73	0.60
2.7203	0.00	0.00	272.0266	3.08	0.70
3.1716	0.00	0.00	317.1597	7.13	0.78
3.6978	0.00	0.00	369.7811	17.38	0.52
4.3114	0.00	0.00	431.1331	29.33	2.18
5.0267	0.00	0.00	502.6642	23.55	1.96
5.8607	0.00	0.00	586.0634	10.03	0.92
6.8330	0.00	0.00	683.2998	2.80	0.38
7.9667	0.00	0.00	796.6691	0.56	0.13
9.2885	0.00	0.00	928.8480	0.07	0.03

Table C.6: Particle size distribution of coal particles before combustion (Sieve size: 35-40).

Average diameter (μm)	Volume (%)	Standard Deviation (%)	Average diameter (μm)	Volume (%)	Standard Deviation (%)
0.1083	0.00	0.00	10.8296	0.00	0.00
0.1263	0.00	0.00	12.6264	0.00	0.00
0.1472	0.00	0.00	14.7213	0.00	0.00
0.1717	0.00	0.00	17.1637	0.00	0.00
0.2001	0.00	0.00	20.0114	0.00	0.00
0.2333	0.00	0.00	23.3316	0.00	0.00
0.2721	0.00	0.00	27.2027	0.00	0.00
0.3172	0.00	0.00	31.7160	0.00	0.00
0.3698	0.00	0.00	36.9781	0.00	0.00
0.4312	0.00	0.00	43.1133	0.00	0.01
0.5027	0.00	0.00	50.2665	0.01	0.01
0.5861	0.00	0.00	58.6064	0.02	0.02
0.6833	0.00	0.00	68.3300	0.04	0.02
0.7967	0.00	0.00	79.6669	0.06	0.03
0.9289	0.00	0.00	92.8848	0.10	0.05
1.0830	0.00	0.00	108.2957	0.18	0.11
1.2627	0.00	0.00	126.2635	0.34	0.22
1.4722	0.00	0.00	147.2125	0.60	0.41
1.7164	0.00	0.00	171.6372	0.96	0.55
2.0011	0.00	0.00	200.1143	1.57	0.60
2.3332	0.00	0.00	233.3161	2.97	0.62
2.7203	0.00	0.00	272.0266	6.53	0.54
3.1716	0.00	0.00	317.1597	14.60	0.43
3.6978	0.00	0.00	369.7811	25.19	1.35
4.3114	0.00	0.00	431.1331	25.39	1.75
5.0267	0.00	0.00	502.6642	14.00	0.85
5.8607	0.00	0.00	586.0634	5.40	0.43
6.8330	0.00	0.00	683.2998	1.62	0.21
7.9667	0.00	0.00	796.6691	0.35	0.06
9.2885	0.00	0.00	928.8480	0.05	0.01

Table C.7: Particle size distribution of coal particles before combustion (Sieve size: 40-45).

Average diameter (µm)	Volume (%)	Standard Deviation (%)	Average diameter (µm)	Volume (%)	Standard Deviation (%)
0.1083	0.00	0.00	10.8296	0.00	0.00
0.1263	0.00	0.00	12.6264	0.00	0.00
0.1472	0.00	0.00	14.7213	0.00	0.00
0.1717	0.00	0.00	17.1637	0.00	0.00
0.2001	0.00	0.00	20.0114	0.00	0.00
0.2333	0.00	0.00	23.3316	0.00	0.00
0.2721	0.00	0.00	27.2027	0.00	0.00
0.3172	0.00	0.00	31.7160	0.01	0.00
0.3698	0.00	0.00	36.9781	0.01	0.01
0.4312	0.00	0.00	43.1133	0.03	0.01
0.5027	0.00	0.00	50.2665	0.05	0.01
0.5861	0.00	0.00	58.6064	0.09	0.02
0.6833	0.00	0.00	68.3300	0.13	0.03
0.7967	0.00	0.00	79.6669	0.21	0.06
0.9289	0.00	0.00	92.8848	0.34	0.09
1.0830	0.00	0.00	108.2957	0.58	0.15
1.2627	0.00	0.00	126.2635	0.97	0.22
1.4722	0.00	0.00	147.2125	1.56	0.32
1.7164	0.00	0.00	171.6372	2.48	0.49
2.0011	0.00	0.00	200.1143	4.30	0.75
2.3332	0.00	0.00	233.3161	8.06	1.00
2.7203	0.00	0.00	272.0266	14.53	0.79
3.1716	0.00	0.00	317.1597	20.72	0.91
3.6978	0.00	0.00	369.7811	20.02	1.41
4.3114	0.00	0.00	431.1331	13.55	1.12
5.0267	0.00	0.00	502.6642	7.16	0.57
5.8607	0.00	0.00	586.0634	3.49	0.35
6.8330	0.00	0.00	683.2998	1.34	0.20
7.9667	0.00	0.00	796.6691	0.32	0.06
9.2885	0.00	0.00	928.8480	0.05	0.02

Table C.8: Particle size distribution of coal particles before combustion (Sieve size: 45-50).

Average diameter (μm)	Volume (%)	Standard Deviation (%)	Average diameter (μm)	Volume (%)	Standard Deviation (%)
0.1083	0.00	0.00	10.8296	0.00	0.00
0.1263	0.00	0.00	12.6264	0.00	0.00
0.1472	0.00	0.00	14.7213	0.00	0.00
0.1717	0.00	0.00	17.1637	0.00	0.00
0.2001	0.00	0.00	20.0114	0.00	0.00
0.2333	0.00	0.00	23.3316	0.00	0.00
0.2721	0.00	0.00	27.2027	0.01	0.01
0.3172	0.00	0.00	31.7160	0.01	0.00
0.3698	0.00	0.00	36.9781	0.02	0.01
0.4312	0.00	0.00	43.1133	0.04	0.01
0.5027	0.00	0.00	50.2665	0.09	0.03
0.5861	0.00	0.00	58.6064	0.15	0.05
0.6833	0.00	0.00	68.3300	0.22	0.07
0.7967	0.00	0.00	79.6669	0.32	0.08
0.9289	0.00	0.00	92.8848	0.52	0.12
1.0830	0.00	0.00	108.2957	0.93	0.21
1.2627	0.00	0.00	126.2635	1.73	0.33
1.4722	0.00	0.00	147.2125	3.16	0.48
1.7164	0.00	0.00	171.6372	5.56	0.57
2.0011	0.00	0.00	200.1143	9.63	0.50
2.3332	0.00	0.00	233.3161	14.95	0.86
2.7203	0.00	0.00	272.0266	17.96	1.78
3.1716	0.00	0.00	317.1597	15.90	1.20
3.6978	0.00	0.00	369.7811	11.42	0.56
4.3114	0.00	0.00	431.1331	7.85	0.90
5.0267	0.00	0.00	502.6642	5.21	1.02
5.8607	0.00	0.00	586.0634	2.89	0.80
6.8330	0.00	0.00	683.2998	1.10	0.36
7.9667	0.00	0.00	796.6691	0.25	0.08
9.2885	0.00	0.00	928.8480	0.08	0.08

Table C.9: Particle size distribution of coal particles before combustion (Sieve size: 50-60).

Average diameter (μm)	Volume (%)	Standard Deviation (%)	Average diameter (μm)	Volume (%)	Standard Deviation (%)
0.1083	0.00	0.00	10.8296	0.00	0.00
0.1263	0.00	0.00	12.6264	0.00	0.00
0.1472	0.00	0.00	14.7213	0.00	0.00
0.1717	0.00	0.00	17.1637	0.00	0.00
0.2001	0.00	0.00	20.0114	0.00	0.00
0.2333	0.00	0.00	23.3316	0.00	0.00
0.2721	0.00	0.00	27.2027	0.00	0.00
0.3172	0.00	0.00	31.7160	0.01	0.01
0.3698	0.00	0.00	36.9781	0.01	0.02
0.4312	0.00	0.00	43.1133	0.03	0.03
0.5027	0.00	0.00	50.2665	0.05	0.05
0.5861	0.00	0.00	58.6064	0.09	0.07
0.6833	0.00	0.00	68.3300	0.14	0.09
0.7967	0.00	0.00	79.6669	0.23	0.14
0.9289	0.00	0.00	92.8848	0.42	0.24
1.0830	0.00	0.00	108.2957	0.83	0.43
1.2627	0.00	0.00	126.2635	1.77	0.74
1.4722	0.00	0.00	147.2125	3.93	0.97
1.7164	0.00	0.00	171.6372	8.22	0.79
2.0011	0.00	0.00	200.1143	13.94	0.82
2.3332	0.00	0.00	233.3161	16.35	1.46
2.7203	0.00	0.00	272.0266	13.77	1.45
3.1716	0.00	0.00	317.1597	10.51	1.31
3.6978	0.00	0.00	369.7811	8.56	1.26
4.3114	0.00	0.00	431.1331	7.69	1.32
5.0267	0.00	0.00	502.6642	6.53	1.36
5.8607	0.00	0.00	586.0634	4.33	1.23
6.8330	0.00	0.00	683.2998	1.93	1.32
7.9667	0.00	0.00	796.6691	0.57	0.69
9.2885	0.00	0.00	928.8480	0.08	0.12

Table C.10: Particle size distribution of coal particles before combustion (Sieve size: 60-70).

Average diameter (µm)	Volume (%)	Standard Deviation (%)	Average diameter (µm)	Volume (%)	Standard Deviation (%)
0.1083	0.00	0.00	10.8296	0.00	0.00
0.1263	0.00	0.00	12.6264	0.00	0.00
0.1472	0.00	0.00	14.7213	0.00	0.00
0.1717	0.00	0.00	17.1637	0.00	0.00
0.2001	0.00	0.00	20.0114	0.00	0.00
0.2333	0.00	0.00	23.3316	0.00	0.01
0.2721	0.00	0.00	27.2027	0.01	0.00
0.3172	0.00	0.00	31.7160	0.02	0.01
0.3698	0.00	0.00	36.9781	0.05	0.05
0.4312	0.00	0.00	43.1133	0.14	0.18
0.5027	0.00	0.00	50.2665	0.34	0.52
0.5861	0.00	0.00	58.6064	0.65	1.04
0.6833	0.00	0.00	68.3300	0.95	1.44
0.7967	0.00	0.00	79.6669	1.30	1.75
0.9289	0.00	0.00	92.8848	1.96	2.20
1.0830	0.00	0.00	108.2957	3.37	2.81
1.2627	0.00	0.00	126.2635	6.12	3.00
1.4722	0.00	0.00	147.2125	10.14	1.52
1.7164	0.00	0.00	171.6372	13.04	2.46
2.0011	0.00	0.00	200.1143	12.27	3.79
2.3332	0.00	0.00	233.3161	9.30	3.26
2.7203	0.00	0.00	272.0266	7.05	2.52
3.1716	0.00	0.00	317.1597	6.19	2.01
3.6978	0.00	0.00	369.7811	6.34	1.67
4.3114	0.00	0.00	431.1331	6.83	1.74
5.0267	0.00	0.00	502.6642	6.21	1.40
5.8607	0.00	0.00	586.0634	4.36	1.16
6.8330	0.00	0.00	683.2998	2.23	0.87
7.9667	0.00	0.00	796.6691	0.81	0.48
9.2885	0.00	0.00	928.8480	0.30	0.46

Table C.11: Particle size distribution of coal particles before combustion (Sieve size: 70-80).

Average diameter (μm)	**Volume (%)**	**Standard Deviation (%)**	**Average diameter (μm)**	**Volume (%)**	**Standard Deviation (%)**
0.1083	0.00	0.00	10.8296	0.00	0.01
0.1263	0.00	0.00	12.6264	0.01	0.00
0.1472	0.00	0.00	14.7213	0.01	0.01
0.1717	0.00	0.00	17.1637	0.01	0.01
0.2001	0.00	0.00	20.0114	0.02	0.01
0.2333	0.00	0.00	23.3316	0.03	0.02
0.2721	0.00	0.00	27.2027	0.05	0.02
0.3172	0.00	0.00	31.7160	0.07	0.02
0.3698	0.00	0.00	36.9781	0.10	0.03
0.4312	0.00	0.00	43.1133	0.16	0.04
0.5027	0.00	0.00	50.2665	0.24	0.06
0.5861	0.00	0.00	58.6064	0.36	0.09
0.6833	0.00	0.00	68.3300	0.55	0.14
0.7967	0.00	0.00	79.6669	0.86	0.23
0.9289	0.00	0.00	92.8848	1.37	0.38
1.0830	0.00	0.00	108.2957	2.15	0.63
1.2627	0.00	0.00	126.2635	3.07	0.92
1.4722	0.00	0.00	147.2125	3.76	1.12
1.7164	0.00	0.00	171.6372	3.87	1.06
2.0011	0.00	0.00	200.1143	3.63	0.87
2.3332	0.00	0.00	233.3161	3.53	0.71
2.7203	0.00	0.00	272.0266	3.89	0.68
3.1716	0.00	0.00	317.1597	5.06	0.91
3.6978	0.00	0.00	369.7811	7.87	1.24
4.3114	0.00	0.00	431.1331	13.04	1.24
5.0267	0.00	0.00	502.6642	17.77	1.12
5.8607	0.00	0.00	586.0634	16.61	3.50
6.8330	0.00	0.00	683.2998	8.94	2.97
7.9667	0.00	0.00	796.6691	2.58	0.97
9.2885	0.00	0.00	928.8480	0.40	0.18

Table C.12: Particle size distribution of coal particles before combustion (Sieve size: < 80).

C.3 Particle Size Distribution after Combustion (CH_4 Diffusion Flame)

Average diameter (µm)	Volume (%)	Standard Deviation (%)	Average diameter (µm)	Volume (%)	Standard Deviation (%)
0.1083	0.00	0.00	10.8296	0.00	0.00
0.1263	0.00	0.00	12.6264	0.00	0.00
0.1472	0.00	0.00	14.7213	0.00	0.00
0.1717	0.00	0.00	17.1637	0.00	0.00
0.2001	0.00	0.00	20.0114	0.00	0.00
0.2333	0.00	0.00	23.3316	0.00	0.00
0.2721	0.00	0.00	27.2027	0.00	0.00
0.3172	0.00	0.00	31.7160	0.00	0.00
0.3698	0.00	0.00	36.9781	0.00	0.00
0.4312	0.00	0.00	43.1133	0.00	0.01
0.5027	0.00	0.00	50.2665	0.01	0.00
0.5861	0.00	0.00	58.6064	0.01	0.00
0.6833	0.00	0.00	68.3300	0.01	0.00
0.7967	0.00	0.00	79.6669	0.01	0.01
0.9289	0.00	0.00	92.8848	0.01	0.01
1.0830	0.00	0.00	108.2957	0.02	0.02
1.2627	0.00	0.00	126.2635	0.04	0.01
1.4722	0.00	0.00	147.2125	0.08	0.02
1.7164	0.00	0.00	171.6372	0.13	0.03
2.0011	0.00	0.00	200.1143	0.23	0.07
2.3332	0.00	0.00	233.3161	0.42	0.11
2.7203	0.00	0.00	272.0266	0.80	0.18
3.1716	0.00	0.00	317.1597	1.45	0.24
3.6978	0.00	0.00	369.7811	2.48	0.30
4.3114	0.00	0.00	431.1331	4.43	0.56
5.0267	0.00	0.00	502.6642	8.91	1.44
5.8607	0.00	0.00	586.0634	19.67	3.20
6.8330	0.00	0.00	683.2998	33.02	2.65
7.9667	0.00	0.00	796.6691	24.25	5.23
9.2885	0.00	0.00	928.8480	4.02	3.44

Table C.13: Particle size distribution of coal particles after combustion - CH_4 diffusion flame. (Sieve size: 18-20).

Average diameter (µm)	Volume (%)	Standard Deviation (%)	Average diameter (µm)	Volume (%)	Standard Deviation (%)
0.1083	0.00	0.00	10.8296	0.00	0.00
0.1263	0.00	0.00	12.6264	0.00	0.00
0.1472	0.00	0.00	14.7213	0.00	0.00
0.1717	0.00	0.00	17.1637	0.00	0.00
0.2001	0.00	0.00	20.0114	0.00	0.00
0.2333	0.00	0.00	23.3316	0.00	0.00
0.2721	0.00	0.00	27.2027	0.00	0.00
0.3172	0.00	0.00	31.7160	0.00	0.00
0.3698	0.00	0.00	36.9781	0.00	0.01
0.4312	0.00	0.00	43.1133	0.00	0.01
0.5027	0.00	0.00	50.2665	0.00	0.01
0.5861	0.00	0.00	58.6064	0.00	0.00
0.6833	0.00	0.00	68.3300	0.00	0.00
0.7967	0.00	0.00	79.6669	0.00	0.01
0.9289	0.00	0.00	92.8848	0.00	0.02
1.0830	0.00	0.00	108.2957	0.01	0.03
1.2627	0.00	0.00	126.2635	0.02	0.02
1.4722	0.00	0.00	147.2125	0.04	0.01
1.7164	0.00	0.00	171.6372	0.07	0.02
2.0011	0.00	0.00	200.1143	0.14	0.05
2.3332	0.00	0.00	233.3161	0.28	0.09
2.7203	0.00	0.00	272.0266	0.54	0.16
3.1716	0.00	0.00	317.1597	1.04	0.24
3.6978	0.00	0.00	369.7811	2.23	0.42
4.3114	0.00	0.00	431.1331	5.63	1.02
5.0267	0.00	0.00	502.6642	14.78	2.81
5.8607	0.00	0.00	586.0634	30.27	5.09
6.8330	0.00	0.00	683.2998	31.66	1.25
7.9667	0.00	0.00	796.6691	11.88	7.49
9.2885	0.00	0.00	928.8480	1.40	3.12

Table C.14: Particle size distribution of coal particles after combustion - CH_4 diffusion flame. (Sieve size: 20-25).

Average diameter (µm)	**Volume (%)**	**Standard Deviation (%)**	**Average diameter (µm)**	**Volume (%)**	**Standard Deviation (%)**
0.1083	0.00	0.00	10.8296	0.00	0.00
0.1263	0.00	0.00	12.6264	0.00	0.00
0.1472	0.00	0.00	14.7213	0.00	0.00
0.1717	0.00	0.00	17.1637	0.00	0.00
0.2001	0.00	0.00	20.0114	0.00	0.00
0.2333	0.00	0.00	23.3316	0.00	0.00
0.2721	0.00	0.00	27.2027	0.00	0.00
0.3172	0.00	0.00	31.7160	0.00	0.00
0.3698	0.00	0.00	36.9781	0.00	0.00
0.4312	0.00	0.00	43.1133	0.00	0.00
0.5027	0.00	0.00	50.2665	0.00	0.00
0.5861	0.00	0.00	58.6064	0.00	0.00
0.6833	0.00	0.00	68.3300	0.00	0.00
0.7967	0.00	0.00	79.6669	0.01	0.01
0.9289	0.00	0.00	92.8848	0.01	0.01
1.0830	0.00	0.00	108.2957	0.02	0.01
1.2627	0.00	0.00	126.2635	0.03	0.01
1.4722	0.00	0.00	147.2125	0.05	0.01
1.7164	0.00	0.00	171.6372	0.09	0.02
2.0011	0.00	0.00	200.1143	0.18	0.03
2.3332	0.00	0.00	233.3161	0.37	0.03
2.7203	0.00	0.00	272.0266	0.74	0.03
3.1716	0.00	0.00	317.1597	1.54	0.08
3.6978	0.00	0.00	369.7811	3.74	0.37
4.3114	0.00	0.00	431.1331	10.16	1.20
5.0267	0.00	0.00	502.6642	23.70	2.05
5.8607	0.00	0.00	586.0634	33.36	0.31
6.8330	0.00	0.00	683.2998	20.55	2.31
7.9667	0.00	0.00	796.6691	4.94	1.11
9.2885	0.00	0.00	928.8480	0.49	0.16

Table C.15: Particle size distribution of coal particles after combustion - CH_4 diffusion flame. (Sieve size: 25-30).

Average diameter (µm)	**Volume (%)**	**Standard Deviation (%)**	**Average diameter (µm)**	**Volume (%)**	**Standard Deviation (%)**
0.1083	0.00	0.00	10.8296	0.00	0.00
0.1263	0.00	0.00	12.6264	0.00	0.00
0.1472	0.00	0.00	14.7213	0.00	0.00
0.1717	0.00	0.00	17.1637	0.00	0.00
0.2001	0.00	0.00	20.0114	0.00	0.00
0.2333	0.00	0.00	23.3316	0.00	0.00
0.2721	0.00	0.00	27.2027	0.00	0.00
0.3172	0.00	0.00	31.7160	0.00	0.00
0.3698	0.00	0.00	36.9781	0.00	0.00
0.4312	0.00	0.00	43.1133	0.00	0.00
0.5027	0.00	0.00	50.2665	0.00	0.00
0.5861	0.00	0.00	58.6064	0.00	0.00
0.6833	0.00	0.00	68.3300	0.00	0.00
0.7967	0.00	0.00	79.6669	0.00	0.00
0.9289	0.00	0.00	92.8848	0.00	0.00
1.0830	0.00	0.00	108.2957	0.01	0.00
1.2627	0.00	0.00	126.2635	0.02	0.01
1.4722	0.00	0.00	147.2125	0.03	0.01
1.7164	0.00	0.00	171.6372	0.06	0.01
2.0011	0.00	0.00	200.1143	0.12	0.02
2.3332	0.00	0.00	233.3161	0.27	0.03
2.7203	0.00	0.00	272.0266	0.63	0.06
3.1716	0.00	0.00	317.1597	1.77	0.18
3.6978	0.00	0.00	369.7811	5.87	0.48
4.3114	0.00	0.00	431.1331	18.57	0.55
5.0267	0.00	0.00	502.6642	34.84	1.36
5.8607	0.00	0.00	586.0634	27.21	0.43
6.8330	0.00	0.00	683.2998	9.06	0.51
7.9667	0.00	0.00	796.6691	1.44	0.15
9.2885	0.00	0.00	928.8480	0.11	0.02

Table C.16: Particle size distribution of coal particles after combustion - CH_4 diffusion flame. (Sieve size: 30-35).

Average diameter (μm)	Volume (%)	Standard Deviation (%)	Average diameter (μm)	Volume (%)	Standard Deviation (%)
0.1083	0.00	0.00	10.8296	0.00	0.00
0.1263	0.00	0.00	12.6264	0.00	0.00
0.1472	0.00	0.00	14.7213	0.00	0.00
0.1717	0.00	0.00	17.1637	0.00	0.00
0.2001	0.00	0.00	20.0114	0.00	0.00
0.2333	0.00	0.00	23.3316	0.00	0.00
0.2721	0.00	0.00	27.2027	0.00	0.00
0.3172	0.00	0.00	31.7160	0.00	0.00
0.3698	0.00	0.00	36.9781	0.00	0.00
0.4312	0.00	0.00	43.1133	0.00	0.00
0.5027	0.00	0.00	50.2665	0.00	0.00
0.5861	0.00	0.00	58.6064	0.00	0.00
0.6833	0.00	0.00	68.3300	0.00	0.00
0.7967	0.00	0.00	79.6669	0.00	0.00
0.9289	0.00	0.00	92.8848	0.00	0.00
1.0830	0.00	0.00	108.2957	0.01	0.01
1.2627	0.00	0.00	126.2635	0.02	0.01
1.4722	0.00	0.00	147.2125	0.03	0.01
1.7164	0.00	0.00	171.6372	0.06	0.03
2.0011	0.00	0.00	200.1143	0.14	0.06
2.3332	0.00	0.00	233.3161	0.33	0.14
2.7203	0.00	0.00	272.0266	1.03	0.34
3.1716	0.00	0.00	317.1597	3.88	0.77
3.6978	0.00	0.00	369.7811	15.03	0.94
4.3114	0.00	0.00	431.1331	35.73	2.88
5.0267	0.00	0.00	502.6642	30.45	1.39
5.8607	0.00	0.00	586.0634	10.90	1.34
6.8330	0.00	0.00	683.2998	2.13	0.50
7.9667	0.00	0.00	796.6691	0.25	0.08
9.2885	0.00	0.00	928.8480	0.01	0.01

Table C.17: Particle size distribution of coal particles after combustion - CH_4 diffusion flame. (Sieve size: 35-40).

Average diameter (µm)	**Volume (%)**	**Standard Deviation (%)**	**Average diameter (µm)**	**Volume (%)**	**Standard Deviation (%)**
0.1083	0.00	0.00	10.8296	0.00	0.00
0.1263	0.00	0.00	12.6264	0.00	0.00
0.1472	0.00	0.00	14.7213	0.00	0.00
0.1717	0.00	0.00	17.1637	0.00	0.00
0.2001	0.00	0.00	20.0114	0.00	0.00
0.2333	0.00	0.00	23.3316	0.00	0.00
0.2721	0.00	0.00	27.2027	0.00	0.00
0.3172	0.00	0.00	31.7160	0.00	0.00
0.3698	0.00	0.00	36.9781	0.00	0.00
0.4312	0.00	0.00	43.1133	0.00	0.00
0.5027	0.00	0.00	50.2665	0.00	0.00
0.5861	0.00	0.00	58.6064	0.00	0.00
0.6833	0.00	0.00	68.3300	0.00	0.01
0.7967	0.00	0.00	79.6669	0.01	0.00
0.9289	0.00	0.00	92.8848	0.01	0.01
1.0830	0.00	0.00	108.2957	0.02	0.02
1.2627	0.00	0.00	126.2635	0.04	0.03
1.4722	0.00	0.00	147.2125	0.09	0.06
1.7164	0.00	0.00	171.6372	0.21	0.11
2.0011	0.00	0.00	200.1143	0.55	0.22
2.3332	0.00	0.00	233.3161	1.61	0.46
2.7203	0.00	0.00	272.0266	4.96	0.86
3.1716	0.00	0.00	317.1597	14.34	1.05
3.6978	0.00	0.00	369.7811	29.36	1.18
4.3114	0.00	0.00	431.1331	29.54	1.41
5.0267	0.00	0.00	502.6642	14.21	0.88
5.8607	0.00	0.00	586.0634	4.13	0.41
6.8330	0.00	0.00	683.2998	0.79	0.12
7.9667	0.00	0.00	796.6691	0.10	0.02
9.2885	0.00	0.00	928.8480	0.01	0.00

Table C.18: Particle size distribution of coal particles after combustion - CH_4 diffusion flame. (Sieve size: 40-45).

Average diameter (μm)	Volume (%)	Standard Deviation (%)	Average diameter (μm)	Volume (%)	Standard Deviation (%)
0.1083	0.00	0.00	10.8296	0.00	0.00
0.1263	0.00	0.00	12.6264	0.00	0.00
0.1472	0.00	0.00	14.7213	0.00	0.00
0.1717	0.00	0.00	17.1637	0.00	0.00
0.2001	0.00	0.00	20.0114	0.00	0.00
0.2333	0.00	0.00	23.3316	0.00	0.00
0.2721	0.00	0.00	27.2027	0.00	0.00
0.3172	0.00	0.00	31.7160	0.00	0.00
0.3698	0.00	0.00	36.9781	0.00	0.00
0.4312	0.00	0.00	43.1133	0.00	0.00
0.5027	0.00	0.00	50.2665	0.00	0.00
0.5861	0.00	0.00	58.6064	0.01	0.01
0.6833	0.00	0.00	68.3300	0.01	0.01
0.7967	0.00	0.00	79.6669	0.02	0.01
0.9289	0.00	0.00	92.8848	0.04	0.02
1.0830	0.00	0.00	108.2957	0.07	0.03
1.2627	0.00	0.00	126.2635	0.16	0.06
1.4722	0.00	0.00	147.2125	0.39	0.13
1.7164	0.00	0.00	171.6372	1.04	0.27
2.0011	0.00	0.00	200.1143	2.90	0.50
2.3332	0.00	0.00	233.3161	7.52	0.73
2.7203	0.00	0.00	272.0266	15.80	0.81
3.1716	0.00	0.00	317.1597	23.94	0.47
3.6978	0.00	0.00	369.7811	23.60	0.60
4.3114	0.00	0.00	431.1331	15.09	1.14
5.0267	0.00	0.00	502.6642	6.59	0.82
5.8607	0.00	0.00	586.0634	2.22	0.36
6.8330	0.00	0.00	683.2998	0.52	0.09
7.9667	0.00	0.00	796.6691	0.07	0.01
9.2885	0.00	0.00	928.8480	0.01	0.01

Table C.19: Particle size distribution of coal particles after combustion - CH_4 diffusion flame. (Sieve size: 45-50).

Average diameter (µm)	**Volume (%)**	**Standard Deviation (%)**	**Average diameter (µm)**	**Volume (%)**	**Standard Deviation (%)**
0.1083	0.00	0.00	10.8296	0.00	0.00
0.1263	0.00	0.00	12.6264	0.00	0.00
0.1472	0.00	0.00	14.7213	0.00	0.00
0.1717	0.00	0.00	17.1637	0.00	0.00
0.2001	0.00	0.00	20.0114	0.00	0.00
0.2333	0.00	0.00	23.3316	0.00	0.00
0.2721	0.00	0.00	27.2027	0.00	0.00
0.3172	0.00	0.00	31.7160	0.00	0.00
0.3698	0.00	0.00	36.9781	0.00	0.00
0.4312	0.00	0.00	43.1133	0.00	0.00
0.5027	0.00	0.00	50.2665	0.01	0.01
0.5861	0.00	0.00	58.6064	0.01	0.01
0.6833	0.00	0.00	68.3300	0.02	0.01
0.7967	0.00	0.00	79.6669	0.03	0.02
0.9289	0.00	0.00	92.8848	0.06	0.03
1.0830	0.00	0.00	108.2957	0.13	0.07
1.2627	0.00	0.00	126.2635	0.36	0.20
1.4722	0.00	0.00	147.2125	1.06	0.54
1.7164	0.00	0.00	171.6372	3.05	1.35
2.0011	0.00	0.00	200.1143	7.62	2.49
2.3332	0.00	0.00	233.3161	14.80	2.13
2.7203	0.00	0.00	272.0266	19.92	1.35
3.1716	0.00	0.00	317.1597	19.64	1.18
3.6978	0.00	0.00	369.7811	15.61	2.30
4.3114	0.00	0.00	431.1331	10.20	2.50
5.0267	0.00	0.00	502.6642	5.14	1.61
5.8607	0.00	0.00	586.0634	1.89	0.65
6.8330	0.00	0.00	683.2998	0.40	0.12
7.9667	0.00	0.00	796.6691	0.05	0.03
9.2885	0.00	0.00	928.8480	0.01	0.01

Table C.20: Particle size distribution of coal particles after combustion - CH_4 diffusion flame. (Sieve size: 50-60).

Average diameter (μm)	Volume (%)	Standard Deviation (%)	Average diameter (μm)	Volume (%)	Standard Deviation (%)
0.1083	0.00	0.00	10.8296	0.00	0.00
0.1263	0.00	0.00	12.6264	0.00	0.00
0.1472	0.00	0.00	14.7213	0.00	0.00
0.1717	0.00	0.00	17.1637	0.00	0.00
0.2001	0.00	0.00	20.0114	0.00	0.00
0.2333	0.00	0.00	23.3316	0.00	0.00
0.2721	0.00	0.00	27.2027	0.00	0.00
0.3172	0.00	0.00	31.7160	0.00	0.00
0.3698	0.00	0.00	36.9781	0.00	0.00
0.4312	0.00	0.00	43.1133	0.00	0.00
0.5027	0.00	0.00	50.2665	0.01	0.01
0.5861	0.00	0.00	58.6064	0.02	0.01
0.6833	0.00	0.00	68.3300	0.03	0.01
0.7967	0.00	0.00	79.6669	0.05	0.02
0.9289	0.00	0.00	92.8848	0.10	0.05
1.0830	0.00	0.00	108.2957	0.28	0.12
1.2627	0.00	0.00	126.2635	0.87	0.35
1.4722	0.00	0.00	147.2125	2.79	0.91
1.7164	0.00	0.00	171.6372	7.33	1.51
2.0011	0.00	0.00	200.1143	13.34	1.21
2.3332	0.00	0.00	233.3161	15.98	1.14
2.7203	0.00	0.00	272.0266	15.00	0.83
3.1716	0.00	0.00	317.1597	13.63	0.28
3.6978	0.00	0.00	369.7811	12.63	1.53
4.3114	0.00	0.00	431.1331	10.30	2.12
5.0267	0.00	0.00	502.6642	5.47	1.33
5.8607	0.00	0.00	586.0634	1.77	0.45
6.8330	0.00	0.00	683.2998	0.34	0.10
7.9667	0.00	0.00	796.6691	0.05	0.02
9.2885	0.00	0.00	928.8480	0.01	0.02

Table C.21: Particle size distribution of coal particles after combustion - CH_4 diffusion flame. (Sieve size: 60-70).

Average diameter (µm)	Volume (%)	Standard Deviation (%)	Average diameter (µm)	Volume (%)	Standard Deviation (%)
0.1083	0.00	0.00	10.8296	0.00	0.00
0.1263	0.00	0.00	12.6264	0.00	0.00
0.1472	0.00	0.00	14.7213	0.00	0.00
0.1717	0.00	0.00	17.1637	0.00	0.00
0.2001	0.00	0.00	20.0114	0.00	0.00
0.2333	0.00	0.00	23.3316	0.00	0.00
0.2721	0.00	0.00	27.2027	0.00	0.00
0.3172	0.00	0.00	31.7160	0.00	0.00
0.3698	0.00	0.00	36.9781	0.01	0.00
0.4312	0.00	0.00	43.1133	0.01	0.00
0.5027	0.00	0.00	50.2665	0.02	0.01
0.5861	0.00	0.00	58.6064	0.03	0.01
0.6833	0.00	0.00	68.3300	0.06	0.02
0.7967	0.00	0.00	79.6669	0.13	0.04
0.9289	0.00	0.00	92.8848	0.35	0.11
1.0830	0.00	0.00	108.2957	1.09	0.34
1.2627	0.00	0.00	126.2635	3.25	0.92
1.4722	0.00	0.00	147.2125	7.57	1.69
1.7164	0.00	0.00	171.6372	11.71	1.86
2.0011	0.00	0.00	200.1143	12.33	1.51
2.3332	0.00	0.00	233.3161	10.92	1.01
2.7203	0.00	0.00	272.0266	10.04	0.48
3.1716	0.00	0.00	317.1597	10.62	0.73
3.6978	0.00	0.00	369.7811	11.59	1.85
4.3114	0.00	0.00	431.1331	10.52	2.62
5.0267	0.00	0.00	502.6642	6.42	2.08
5.8607	0.00	0.00	586.0634	2.50	0.85
6.8330	0.00	0.00	683.2998	0.65	0.19
7.9667	0.00	0.00	796.6691	0.14	0.06
9.2885	0.00	0.00	928.8480	0.05	0.05

Table C.22: Particle size distribution of coal particles after combustion - CH_4 diffusion flame. (Sieve size: 70-80).

Average diameter (μm)	Volume (%)	Standard Deviation (%)	Average diameter (μm)	Volume (%)	Standard Deviation (%)
0.1083	0.00	0.00	10.8296	0.00	0.00
0.1263	0.00	0.00	12.6264	0.00	0.00
0.1472	0.00	0.00	14.7213	0.00	0.00
0.1717	0.00	0.00	17.1637	0.00	0.00
0.2001	0.00	0.00	20.0114	0.00	0.00
0.2333	0.00	0.00	23.3316	0.01	0.00
0.2721	0.00	0.00	27.2027	0.01	0.00
0.3172	0.00	0.00	31.7160	0.02	0.00
0.3698	0.00	0.00	36.9781	0.04	0.00
0.4312	0.00	0.00	43.1133	0.07	0.01
0.5027	0.00	0.00	50.2665	0.13	0.02
0.5861	0.00	0.00	58.6064	0.24	0.03
0.6833	0.00	0.00	68.3300	0.44	0.04
0.7967	0.00	0.00	79.6669	0.80	0.09
0.9289	0.00	0.00	92.8848	1.42	0.18
1.0830	0.00	0.00	108.2957	2.37	0.34
1.2627	0.00	0.00	126.2635	3.55	0.48
1.4722	0.00	0.00	147.2125	4.58	0.51
1.7164	0.00	0.00	171.6372	5.15	0.43
2.0011	0.00	0.00	200.1143	5.45	0.35
2.3332	0.00	0.00	233.3161	5.91	0.36
2.7203	0.00	0.00	272.0266	7.10	0.43
3.1716	0.00	0.00	317.1597	9.68	0.51
3.6978	0.00	0.00	369.7811	13.78	0.50
4.3114	0.00	0.00	431.1331	16.61	1.01
5.0267	0.00	0.00	502.6642	13.30	1.24
5.8607	0.00	0.00	586.0634	6.68	0.81
6.8330	0.00	0.00	683.2998	2.14	0.38
7.9667	0.00	0.00	796.6691	0.45	0.10
9.2885	0.00	0.00	928.8480	0.07	0.04

Table C.23: Particle size distribution of coal particles after combustion - CH_4 diffusion flame. (Sieve size: < 80).

C.4 Particle Size Distribution after Combustion (CH_4/air Premixed Flame)

Average diameter (μm)	Volume (%)	Standard Deviation (%)	Average diameter (μm)	Volume (%)	Standard Deviation (%)
0.1083	0.00	0.00	10.8296	0.00	0.00
0.1263	0.00	0.00	12.6264	0.00	0.00
0.1472	0.00	0.00	14.7213	0.00	0.00
0.1717	0.00	0.00	17.1637	0.00	0.00
0.2001	0.00	0.00	20.0114	0.00	0.00
0.2333	0.00	0.00	23.3316	0.00	0.00
0.2721	0.00	0.00	27.2027	0.00	0.00
0.3172	0.00	0.00	31.7160	0.00	0.00
0.3698	0.00	0.00	36.9781	0.00	0.00
0.4312	0.00	0.00	43.1133	0.00	0.00
0.5027	0.00	0.00	50.2665	0.00	0.00
0.5861	0.00	0.00	58.6064	0.00	0.00
0.6833	0.00	0.00	68.3300	0.00	0.00
0.7967	0.00	0.00	79.6669	0.01	0.00
0.9289	0.00	0.00	92.8848	0.01	0.01
1.0830	0.00	0.00	108.2957	0.02	0.01
1.2627	0.00	0.00	126.2635	0.04	0.02
1.4722	0.00	0.00	147.2125	0.10	0.03
1.7164	0.00	0.00	171.6372	0.25	0.06
2.0011	0.00	0.00	200.1143	0.70	0.11
2.3332	0.00	0.00	233.3161	2.11	0.23
2.7203	0.00	0.00	272.0266	6.36	0.43
3.1716	0.00	0.00	317.1597	16.47	0.53
3.6978	0.00	0.00	369.7811	28.91	0.59
4.3114	0.00	0.00	431.1331	27.19	0.71
5.0267	0.00	0.00	502.6642	12.97	0.44
5.8607	0.00	0.00	586.0634	3.92	0.21
6.8330	0.00	0.00	683.2998	0.81	0.06
7.9667	0.00	0.00	796.6691	0.11	0.01
9.2885	0.00	0.00	928.8480	0.01	0.00

Table C.24: Particle size distribution of coal particles after combustion - CH_4/air premixed flame. (Sieve size: 40-45).

Average diameter (µm)	Volume (%)	Standard Deviation (%)	Average diameter (µm)	Volume (%)	Standard Deviation (%)
0.1083	0.00	0.00	10.8296	0.00	0.00
0.1263	0.00	0.00	12.6264	0.00	0.00
0.1472	0.00	0.00	14.7213	0.00	0.00
0.1717	0.00	0.00	17.1637	0.00	0.00
0.2001	0.00	0.00	20.0114	0.00	0.00
0.2333	0.00	0.00	23.3316	0.01	0.00
0.2721	0.00	0.00	27.2027	0.01	0.00
0.3172	0.00	0.00	31.7160	0.02	0.00
0.3698	0.00	0.00	36.9781	0.03	0.00
0.4312	0.00	0.00	43.1133	0.05	0.00
0.5027	0.00	0.00	50.2665	0.09	0.00
0.5861	0.00	0.00	58.6064	0.17	0.01
0.6833	0.00	0.00	68.3300	0.34	0.02
0.7967	0.00	0.00	79.6669	0.66	0.02
0.9289	0.00	0.00	92.8848	1.28	0.04
1.0830	0.00	0.00	108.2957	2.34	0.06
1.2627	0.00	0.00	126.2635	3.77	0.10
1.4722	0.00	0.00	147.2125	5.11	0.15
1.7164	0.00	0.00	171.6372	5.84	0.19
2.0011	0.00	0.00	200.1143	6.10	0.22
2.3332	0.00	0.00	233.3161	6.58	0.24
2.7203	0.00	0.00	272.0266	7.84	0.29
3.1716	0.00	0.00	317.1597	10.49	0.42
3.6978	0.00	0.00	369.7811	14.27	0.56
4.3114	0.00	0.00	431.1331	15.83	0.28
5.0267	0.00	0.00	502.6642	11.58	1.49
5.8607	0.00	0.00	586.0634	5.52	0.87
6.8330	0.00	0.00	683.2998	1.70	0.35
7.9667	0.00	0.00	796.6691	0.35	0.16
9.2885	0.00	0.00	928.8480	0.04	0.03

Table C.25: Particle size distribution of coal particles after combustion -CH_4/air premixed flame. (Sieve size: < 80).

C.5 Particle Size Distribution after Combustion

($CH_4/O_2/CO_2$ Premixed Flame)

Average diameter (µm)	Volume (%)	Standard Deviation (%)	Average diameter (µm)	Volume (%)	Standard Deviation (%)
0.1083	0.00	0.00	10.8296	0.00	0.00
0.1263	0.00	0.00	12.6264	0.00	0.00
0.1472	0.00	0.00	14.7213	0.00	0.00
0.1717	0.00	0.00	17.1637	0.00	0.00
0.2001	0.00	0.00	20.0114	0.00	0.00
0.2333	0.00	0.00	23.3316	0.00	0.00
0.2721	0.00	0.00	27.2027	0.00	0.00
0.3172	0.00	0.00	31.7160	0.00	0.00
0.3698	0.00	0.00	36.9781	0.00	0.00
0.4312	0.00	0.00	43.1133	0.00	0.00
0.5027	0.00	0.00	50.2665	0.00	0.01
0.5861	0.00	0.00	58.6064	0.00	0.02
0.6833	0.00	0.00	68.3300	0.00	0.03
0.7967	0.00	0.00	79.6669	0.01	0.05
0.9289	0.00	0.00	92.8848	0.02	0.07
1.0830	0.00	0.00	108.2957	0.03	0.10
1.2627	0.00	0.00	126.2635	0.06	0.15
1.4722	0.00	0.00	147.2125	0.13	0.21
1.7164	0.00	0.00	171.6372	0.31	0.25
2.0011	0.00	0.00	200.1143	0.77	0.28
2.3332	0.00	0.00	233.3161	2.12	0.30
2.7203	0.00	0.00	272.0266	5.98	0.35
3.1716	0.00	0.00	317.1597	15.28	0.39
3.6978	0.00	0.00	369.7811	27.93	0.26
4.3114	0.00	0.00	431.1331	27.85	1.09
5.0267	0.00	0.00	502.6642	14.03	0.98
5.8607	0.00	0.00	586.0634	4.39	0.46
6.8330	0.00	0.00	683.2998	0.93	0.19
7.9667	0.00	0.00	796.6691	0.13	0.06
9.2885	0.00	0.00	928.8480	0.01	0.01

Table C.26: Particle size distribution of coal particles after combustion - $CH_4/O_2/CO_2$ premixed flame. (Sieve size: 40-45).

Average diameter (µm)	**Volume (%)**	**Standard Deviation (%)**	**Average diameter (µm)**	**Volume (%)**	**Standard Deviation (%)**
0.1083	0.00	0.00	10.8296	0.00	0.00
0.1263	0.00	0.00	12.6264	0.00	0.00
0.1472	0.00	0.00	14.7213	0.00	0.00
0.1717	0.00	0.00	17.1637	0.00	0.00
0.2001	0.00	0.00	20.0114	0.00	0.00
0.2333	0.00	0.00	23.3316	0.01	0.00
0.2721	0.00	0.00	27.2027	0.01	0.00
0.3172	0.00	0.00	31.7160	0.02	0.00
0.3698	0.00	0.00	36.9781	0.03	0.00
0.4312	0.00	0.00	43.1133	0.06	0.00
0.5027	0.00	0.00	50.2665	0.10	0.01
0.5861	0.00	0.00	58.6064	0.20	0.02
0.6833	0.00	0.00	68.3300	0.39	0.03
0.7967	0.00	0.00	79.6669	0.77	0.05
0.9289	0.00	0.00	92.8848	1.48	0.07
1.0830	0.00	0.00	108.2957	2.65	0.10
1.2627	0.00	0.00	126.2635	4.12	0.15
1.4722	0.00	0.00	147.2125	5.33	0.21
1.7164	0.00	0.00	171.6372	5.88	0.25
2.0011	0.00	0.00	200.1143	6.06	0.28
2.3332	0.00	0.00	233.3161	6.50	0.30
2.7203	0.00	0.00	272.0266	7.72	0.35
3.1716	0.00	0.00	317.1597	10.24	0.39
3.6978	0.00	0.00	369.7811	13.68	0.26
4.3114	0.00	0.00	431.1331	15.24	1.09
5.0267	0.00	0.00	502.6642	11.53	0.98
5.8607	0.00	0.00	586.0634	5.69	0.46
6.8330	0.00	0.00	683.2998	1.84	0.19
7.9667	0.00	0.00	796.6691	0.38	0.06
9.2885	0.00	0.00	928.8480	0.06	0.01

Table C.27: Particle size distribution of coal particles after combustion - $CH_4/O_2/CO_2$ premixed flame. (Sieve size: < 80).

C.6 Particle Size Distribution after Combustion (CH_4/O_2 Premixed Flame)

Average diameter (µm)	Volume (%)	Standard Deviation (%)	Average diameter (µm)	Volume (%)	Standard Deviation (%)
0.1083	0.00	0.00	10.8296	0.00	0.00
0.1263	0.00	0.00	12.6264	0.00	0.00
0.1472	0.00	0.00	14.7213	0.00	0.00
0.1717	0.00	0.00	17.1637	0.00	0.00
0.2001	0.00	0.00	20.0114	0.00	0.00
0.2333	0.00	0.00	23.3316	0.00	0.00
0.2721	0.00	0.00	27.2027	0.00	0.00
0.3172	0.00	0.00	31.7160	0.00	0.00
0.3698	0.00	0.00	36.9781	0.00	0.00
0.4312	0.00	0.00	43.1133	0.00	0.00
0.5027	0.00	0.00	50.2665	0.00	0.00
0.5861	0.00	0.00	58.6064	0.00	0.01
0.6833	0.00	0.00	68.3300	0.00	0.02
0.7967	0.00	0.00	79.6669	0.01	0.03
0.9289	0.00	0.00	92.8848	0.01	0.05
1.0830	0.00	0.00	108.2957	0.02	0.07
1.2627	0.00	0.00	126.2635	0.04	0.11
1.4722	0.00	0.00	147.2125	0.09	0.16
1.7164	0.00	0.00	171.6372	0.21	0.25
2.0011	0.00	0.00	200.1143	0.55	0.38
2.3332	0.00	0.00	233.3161	1.61	0.50
2.7203	0.00	0.00	272.0266	4.96	0.40
3.1716	0.00	0.00	317.1597	14.34	0.46
3.6978	0.00	0.00	369.7811	29.36	0.71
4.3114	0.00	0.00	431.1331	29.54	0.56
5.0267	0.00	0.00	502.6642	14.21	0.29
5.8607	0.00	0.00	586.0634	4.13	0.18
6.8330	0.00	0.00	683.2998	0.79	0.10
7.9667	0.00	0.00	796.6691	0.10	0.03
9.2885	0.00	0.00	928.8480	0.01	0.01

Table C.28: Particle size distribution of coal particles after combustion - CH_4/O_2 premixed flame. (Sieve size: 40-45).

Average diameter (µm)	Volume (%)	Standard Deviation (%)	Average diameter (µm)	Volume (%)	Standard Deviation (%)
0.1083	0.00	0.00	10.8296	0.00	0.00
0.1263	0.00	0.00	12.6264	0.00	0.00
0.1472	0.00	0.00	14.7213	0.00	0.00
0.1717	0.00	0.00	17.1637	0.00	0.00
0.2001	0.00	0.00	20.0114	0.00	0.00
0.2333	0.00	0.00	23.3316	0.01	0.00
0.2721	0.00	0.00	27.2027	0.01	0.00
0.3172	0.00	0.00	31.7160	0.02	0.00
0.3698	0.00	0.00	36.9781	0.03	0.00
0.4312	0.00	0.00	43.1133	0.06	0.00
0.5027	0.00	0.00	50.2665	0.11	0.00
0.5861	0.00	0.00	58.6064	0.21	0.01
0.6833	0.00	0.00	68.3300	0.40	0.02
0.7967	0.00	0.00	79.6669	0.79	0.03
0.9289	0.00	0.00	92.8848	1.54	0.05
1.0830	0.00	0.00	108.2957	2.79	0.07
1.2627	0.00	0.00	126.2635	4.35	0.11
1.4722	0.00	0.00	147.2125	5.59	0.16
1.7164	0.00	0.00	171.6372	6.07	0.25
2.0011	0.00	0.00	200.1143	6.26	0.38
2.3332	0.00	0.00	233.3161	6.80	0.50
2.7203	0.00	0.00	272.0266	8.09	0.40
3.1716	0.00	0.00	317.1597	10.42	0.46
3.6978	0.00	0.00	369.7811	13.20	0.71
4.3114	0.00	0.00	431.1331	14.25	0.56
5.0267	0.00	0.00	502.6642	10.75	0.29
5.8607	0.00	0.00	586.0634	5.62	0.18
6.8330	0.00	0.00	683.2998	2.04	0.10
7.9667	0.00	0.00	796.6691	0.46	0.03
9.2885	0.00	0.00	928.8480	0.13	0.01

Table C.29: Particle size distribution of coal particles after combustion - CH_4/O_2 premixed flame. (Sieve size: < 80).